Liquid Crystal Self-Assembly and Organic–Inorganic Hybrid Material Design

Pouya Moghimian

Dissertation submitted as a requirement for the degree of Doctor of Philosophy
January 2017 – Technical University of Darmstadt (TUD) – D17

TECHNISCHE
UNIVERSITÄT
DARMSTADT

Liquid Crystal Self-Assembly and Organic–Inorganic Hybrid Material Design

Dissertation Approved by the Department of Materials and Earth Sciences
in Fulfillment of the Requirements for the Degree of

Doctor of Philosophy (Dr. rer. nat.)

By

Pouya Moghimian
Max Planck Institute for Solid State Research

B.Eng. Ceramics Engineering 2011, M.Sc. Advanced Materials 2013
Born in Tehran

Technische Universität Darmstadt, Hochschulkennziffer D17

Place of Publication: Darmstadt
Year of Publication: 2017

Date of Submission: October 24, 2016
Date of Oral Examination: January 17, 2017

Certified by

Peter A. van Aken
Professor of Geo-Material Science
Max Planck Institute for Solid State Research
Referee

Certified by

Hans-Joachim Kleebe
Professor of Geo-Material Science
Technical University of Darmstadt
Co-Referee

Liquid Crystal Self-Assembly and Organic–Inorganic Hybrid Material Design

By

Pouya Moghimian

Submitted to the Department of Materials and Earth Sciences on October 24th, 2016
in Partial Fulfillment of the Requirements for the Degree of
Doctor of Philosophy in Materials Science

ABSTRACT

Viruses offer promising applications in virotronics (virus-based technology) and as soft scaffolds for building intelligent (*i.e.* responsive) multicomponent materials. The Ff class of phages including M13 and fd phages have recently received high attention due to their high uniformity and monodispersity. Phages have been used in virus-based applications owing to their low cost production, mild working temperature and pH conditions, chemical modifiability and ease of manipulation. In addition, they were found to exhibit liquid crystalline behavior in solutions; a property that made rod-like phages suitable material for self-assembly and soft matter physics. All of these features brought phages in the center of focus for the use in diverse applications such as semiconductors, chemical and biological sensing and piezoelectric nanogenerators.

Spontaneous assembly of anisometric colloidal particles, such as rod-like M13 phages, in two-dimensions (2D) can be carried out via evaporation of the colloid-containing suspensions on solid substrates. Rod-like particles having a high aspect ratio (*e.g.* very long inoviruses) show liquid crystal (LC) behavior in suspensions and they can be treated as polymer chains composed of homogenous elastic material, where the persistence length characterizes the molecular stiffness. Therefore, suspensions containing M13 phages are considered to be ideal model systems for studying the properties of soft matter systems. Here, I designed an experiment in order to obtain a condition in which filamentous M13 phages have a high degree of alignment along a common axis on a solid substrate. One aim is to attain a fully covered surface with densely packed and highly oriented M13 phage particles. Moreover, the effect of substrate surface chemistry on the alignment and orientation of macromolecules was investigated. Our results suggest an approach that can be used to immobilize oriented viral arrays on amorphous carbon surface. A unique feature of our approach is that the aforementioned architectures can be obtained by applying phage solution on a surface without employing nanoparticle assembly methods such as dip coating or convective assembly. However, an ordered medium of liquid crystals often possesses a variety of defects and deformations, at which the director $n(r)$ of the liquid crystal undergoes an abrupt change compared to the vicinity of the defect. Experimental research on these effects has been remained challenging and been barely performed on confined rod-like colloidal particles on structured surfaces. Therefore, I intend to investigate the local deformation of rod-like M13 phage particles resulting from confinement in an irregular stranded web of thin carbon film and compare them to the existing theories. I shift the focus from evaporative self-organization on rationally designed surfaces to that on a complex surface. The aim is to study the possibility of controlling the orientation of M13 phages in two-dimensional nematic films by choosing structured substrates.

These rod-like molecules have the ability to mineralize a variety of inorganic materials. They can be used for the controlled growth of inorganic materials and for the production of hybrid structures. Owing to this property, phages are in the center of attention for the selected deposition and

mineralization of inorganic substances. Here, I use M13 phages to mineralize zinc oxide nanoparticles from a deposition solution. This allowed us to construct nano-hybrid layered materials consisting of alternating organic (M13 phage) and inorganic (zinc oxide) layers (layer-by-layer) on a silicon substrate. Our aim is to achieve a homogeneous and uniform phage-assisted assembly of layered structures and to determine their microstructure, elemental composition and homogeneity. These hybrid structures have a potential for the use in biotechnology such as organic electronics.

ZUSAMMENFASSUNG

Viren bieten vielversprechende Anwendungen in „Virotronics“ (Virus-basierte Technologie) und als weiche Gerüste für den Aufbau intelligenter mehrkomponentiger Materialien. Die Ff Klasse von Phagen einschließlich M13 und fd Phagen haben vor kurzem hohe Aufmerksamkeit wegen ihrer hohen Gleichmäßigkeit und Monodispersität erlangt. Materialwissenschaftler und chemische Biologen haben Phagen in Virus-basierten Anwendungen aufgrund ihrer geringen Produktionskosten, milden Temperatur und pH-Bedingungen, chemischen Modifizierbarkeit und Leichtigkeit der Manipulation verwendet. Darüber hinaus wurde ein flüssigkristallines Verhalten in Lösungen nachgewiesen; eine Eigenschaft, die stabförmige Phagen zu einem geeigneten Material für Selbstorganisation und der Physik der weichen Materie macht. Alle diese Merkmale brachten Phagen in den Fokus für den Einsatz in verschiedenen Anwendungen, wie beispielsweise Halbleiter Technologie, Chemo- und Biosensoren und piezoelektrische Nanogeneratoren.

Den spontanen Zusammenbau von anisometrischen kolloidalen Teilchen, wie stabförmige M13 Phagen, in zwei Dimensionen (2D) kann über Verdampfung der kolloidhaltigen Suspensionen auf festen Substraten durchgeführt werden. Stabförmige Teilchen mit einem hohen Aspektverhältnis (beispielsweise sehr lange „Inoviruses“) zeigen flüssigkristallines (LC) Verhalten in Suspensionen und sie können als Polymerketten behandelt werden, die aus homogenen elastischen Material bestehen, wobei die Persistenzlänge des Moleküls seine Steifigkeit auszeichnet. Daher werden Suspensionen, die M13 Phagen enthalten, als ideale Modellsysteme für das Studium der Eigenschaften weicher Materie angesehen. Hier entwickelte ich ein Experiment, um einen Zustand zu erhalten, in dem filamentöse M13 Phagen einen größtmöglichen Grad der Ausrichtung entlang einer gemeinsamen Achse auf einem Substrat aufweisen. Ein Ziel ist es, eine Oberfläche zu erreichen, die mit dicht gepackten und gleichförmig ausgerichteten M13 Phagen möglichst vollständig bedeckt ist. Darüber hinaus wurde die Auswirkung der Substratoberflächenchemie auf die Ausrichtung und Orientierung der Makromoleküle untersucht. Unsere Ergebnisse deuten darauf hin, dass dieser Ansatz, dazu verwendet werden kann, orientierte virale Felder auf amorpher Kohlenstoffoberfläche zu immobilisieren. Ein besonderes Merkmal unseres Ansatzes ist, dass die oben genannten Strukturen durch Aufbringen einer Phagenlösung auf einer Oberfläche ohne den Einsatz von auf Nanopartikeln basierenden Montageverfahren wie „dip coating“ oder „convective assembly“ erhalten werden können. Jedoch besitzt ein geordnetes Medium von Flüssigkristallen häufig eine Vielzahl von Fehlstellen und Deformationen, wo der Direktor $n(r)$ des Flüssigkristalls eine abrupte Änderung im Vergleich zu der Umgebung des Defektes erfährt. Experimentelle Forschung über diese Effekte sind noch immer eine große Herausforderung und wurde nur selten an beschränkten, stabförmigen, kolloidalen Teilchen auf strukturierten Oberflächen durchgeführt. Deshalb will ich die lokale Verformung von stabförmigen M13 Phagen untersuchen, die sich aus der Umgebung in einem unregelmäßigen Netz von dünnen Kohlenstoff Filmen ergibt und diese mit den existierenden Theorien vergleichen. Ich verschiebe den Fokus von Verdunstungsselbstorganisation auf rational designten Oberflächen zu der auf einer komplexen Oberfläche. Das Ziel ist es, die Möglichkeit einer Steuerung der Orientierung von M13 Phagen in 2D nematischen Filme zu untersuchen, indem strukturierte Substrate verwendet werden.

Diese stabförmigen Moleküle haben die Fähigkeit, eine Vielzahl von anorganischen Materialien zu mineralisieren. Sie können für das kontrollierte Wachstum von anorganischen Materialien verwendet werden, um Hybridstrukturen zu produzieren. Aufgrund dieser Eigenschaft sind Phagen in den Mittelpunkt der Aufmerksamkeit für die gezielte Ablagerung und Mineralisierung von anorganischen Substanzen gerückt. Hier verwende ich M13 Phagen, um Zinkoxid Nanopartikel

aus einer Abscheidungslösung zu mineralisieren. Dies erlaubte uns, Nanohybridmaterialien zu konstruieren, die aus alternierenden organischen (M13 Phagen) und anorganischen (Zinkoxid) Schicht („layer-by-layer“) auf einem Substrat bestehen. Unser Ziel ist es, eine homogene und einheitliche Phagen-gestützte Anordnung von Schichtstrukturen zu erreichen und ihre Mikrostruktur, elementare Zusammensetzung und Homogenität zu bestimmen. Diese Hybridstrukturen haben ein Potenzial für den Einsatz in der Biotechnologie wie die organische Elektronik.

THESIS SUPERVISORS

Prof. Dr. Peter A. van Aken

Professor of Geo-Material Science
Stuttgart Center for Electron Microscopy (StEM)
Max Planck Institute for Solid State Research

Prof. Dr. Hans-Joachim Kleebe

Professor of Geo-Material Science
Geo- and Material Sciences Department
Technical University of Darmstadt

THESIS COMMITTEE

Prof. Dr. Peter A. van Aken

Referee
Professor of Geo-Material Science
Geo- and Material Sciences Department
Technical University of Darmstadt

Prof. Dr. Hans-Joachim Kleebe

Co-referee
Professor of Geo-Material Science
Geo- and Material Sciences Department
Technical University of Darmstadt

Prof. Dr. Wolfram Jägermann

Examiner
Professor of Materials Science
Materials Science Department
Technical University of Darmstadt

Prof. Dr. Jörg J. Schneider

Examiner
Professor of Chemistry
Inorganic Chemistry Department
Technical University of Darmstadt

To my parents, Jamileh and Ahmad
who always believed in me all the way;
To my brother, Nima, for his encouragement
and caring guidance in all ways

ACKNOWLEDGMENTS

First of all, I sincerely express my deepest gratitude to my thesis supervisors, Prof. Dr. van Aken and Prof. Dr. Hans-Joachim Kleebe. I am grateful to both of them for guiding and encouraging me throughout my doctoral study and for giving me the opportunity to develop my own ideas. I have always appreciated and admired Prof. van Aken's leadership and Prof. Kleebe's knowledge and approachable personality. I have equally enjoyed working with Vesna because of her kindness, support and enthusiasm. I feel lucky for having been part of their research group. I would like to thank my thesis committee members, Prof. Dr. Wolfram Jägermann, and Prof. Dr. Jörg J. Schneider for the insightful discussions on my work that gave me a new perspective.

I pay my compliments and express my debt to Dr. Ludger Harnau (MPI-IS) both as a mensch and as a distinguished scholar in Physics, who inspired me most and initiated me into the study of condensed matter physics.

I would like to gratefully acknowledge all the members of StEM for bringing so much joy and for encouraging and caring words. I would also like to thank several mentors that helped me with laboratory techniques and instrument use, especially at the beginning and also throughout my Ph.D.; In the TEM sample preparation lab, Ute Salzberger and Marion Kelsch taught me sample preparation methods beside tripod polishing technique and ion milling. In the TEM labs, Kersten Hahn and Peter Kopold for tutoring me in electron microscopy techniques. In the SEM labs, Felicitas Predel for teaching me SEM techniques. Ulrike Eigenthaler for preparing TEM samples by FIB. In the Biolabs, my dearest mentor and friend Sandra J. Facey for providing me viral solutions and for the fruitful discussions. Dirk Rothenstein for teaching me drop casting method. Thanks also to Stefan Kilper for sharing his knowledge of the organic–inorganic layer-by-layer assembly with me and several other techniques related to thin films. Joachim Spatz for the allowance to use his biolabs and Christine Mollenhauer for providing all the biolab equipment and for her support during the experiments. Petia Atanasova for her contribution to my knowledge about the organic–inorganic structures. In particular, I would like to thank especially my dear colleagues and friends, Nilesh Vats, Surong Guo, Iman Rastegar, Nima Farhmand Bafi, Mahdieh Schmidt and Robin Lingstädt. They have been absolutely helpful with research, and their presence also made my days more pleasant. Especially, I would like to sincerely thank Jana Rein who was continuously there beside me all the way.

I have also had the opportunity and honor to work with other very helpful collaborators, who helped me with measurements for my project or kindly offered help with different tasks; Benoit P. Pichon from the University of Strasbourg who gave me amazing ideas in our project and initiated the study of organic and magnetic inorganic hybrid materials. Francisco de la Peña from the University of Cambridge who helped me tremendously with image analysis. Markus Bier, Mykola Tasinkevych and Nima Farahmand Bafi, from the Theory of Inhomogeneous Condensed Matter group (MPI-IS) for discussions and the help with data analysis. I would like to acknowledge, in particular, the help offered by Alison F. Mark from StEM. She was very generous with her time, and her ideas and expertise were extremely useful for developing my work. I also want to highlight the contribution of StEM administrative assistant, Caroline Heer, who has been tremendously helpful with scheduling and simply for her care.

I would like to sincerely acknowledge the financial support by the German Research Foundation (DFG). The research leading to our results has received funding from the European Union Seventh Framework Programme [FP7/2007-2013] under grant agreement no. 312483 (ESTEEM2).

I could not thank enough my family, whose love and guidance carried me through this process. You have been my greatest inspiration and I could not have finished this thesis without you.

BIOGRAPHICAL NOTE

EDUCATION

Ph.D.	Max Planck Institute for Solid State Research Technical University of Darmstadt (TUD)	2013–2017
	Materials Science	*Supervised by,* Prof. Dr. Peter A. van Aken Prof. Dr. Hans-Joachim Kleebe
M.Sc.	University of Ulm	2011–2013
	Advanced Materials –Biomaterials–	*Supervised by,* Prof. Dr. Ute Kaiser Prof. Dr. Peter A. van Aken
B.Eng.	Iran University of Science & Technology (IUST)	2006–2011
	Ceramics Engineering	*Supervised by,* Prof. Dr. Jafar Javadpour

HONORS AND AWARDS

Awarded as "Recognized Reviewer" by the journal of *Powder Technology* (Elsevier) and the journal of *Materials Science & Engineering C* (Elsevier)

PUBLICATIONS

Papers

P. Moghimian, V. Srot, B. P. Pichon, S. J. Facey, P. A. van Aken, "Stability of M13 Phage in Organic Solvents", *Journal of Biomaterials and Nanobiotechnology*, 2016, **7** (2), 72-77.

P. Moghimian, L. Harnau, V. Srot, F. de la Peña, N.F. Bafi, S. J. Facey, P. A. van Aken, "Controlled Self-Assembly of Biomolecular Rods on Structured Substrates", *Soft Matter*, 2016, **12** (13), 3177-3183.

P. Moghimian, S. Kilper, V. Srot, D. Rothenstein, S. J. Facey, B. Hauer, J. Bill, P. A. van Aken, "Phage-Assisted Assembly of Organic-Inorganic Layered Hybrid Structures", *International Journal of Materials Research (IJMR)*, 2016, **107** (4), 295-299.

P. Moghimian, V. Srot, D. Rothenstein, S. J. Facey, L. Harnau, B. Hauer, J. Bill, P. A. van Aken, "Adsorption and Self-Assembly of M13 Phage into Directionally Organized Structures on C and SiO_2 Films", *Langmuir*, 2014, **30** (38), 11428-11432.

P. Moghimian, A. Najafi, S. Afshar, J. Javadpour, "Effect of low temperature on formation mechanism of calcium phosphate nano powder via precipitation method", *Advanced Powder Technology*, 2012, **23** (6), 744-751.

Conferences

V. Srot, B. Bussmann, U. Salzberger, P. Moghimian, M. Espanol, B. Hauer, P. A. van Aken, "Investigations of Sensitive Composite Organic-Inorganic Materials by Analytical (S)TEM" (oral), Materials Science Engineering (MSE) Congress, September 2016, Darmstadt, Germany.

P. Moghimian, L. Harnau, V. Srot, F. de la Peña, N.F. Bafi, S. J. Facey, P. A. van Aken, "Colloidal Rods in Irregular Spatial Confinement" (poster), The 16th European Microscopy Congress (EMC), August 2016, Lyon, France.

P. Moghimian, V. Srot, L. Harnau, D. Rothenstein, S. J. Facey, B. Hauer, J. Bill, P. A. van Aken, "Assembly of Semi-Flexible Macromolecules and Defect Formation in Colloid Ordering in Non-Symmetric Geometries" (oral), Materials Research Society (MRS) Fall Meeting, November 2015, Boston, MA, USA.

P. Moghimian, V. Srot, D. Rothenstein, S. J. Facey, L. Harnau, S. Kilper, B. Hauer, J. Bill, P. A. van Aken, "Phage-Controlled Assembly of Organic-Inorganic Hybrid Layered Structures" (poster), Microscopy Conference 2015 (MC 2015) , September 2015, Göttingen, Germany.

P. Moghimian, V. Srot, D. Rothenstein, S. J. Facey, B. Hauer, J. Bill, T. Schimmel, P. A. van Aken, "From Ultrathin Assembled Viral Films to Organic-Inorganic Multilayered Structures" (oral), European Materials Research Society (E-MRS), May 2015, Lille, France.

P. Moghimian, V. Srot, D. Rothenstein, S. J. Facey, P. A. van Aken, "Adsorption and self-assembly of M13 phage into directionally organized structures on C and SiO_2 thin films" (oral), Materials Science Engineering (MSE) Congress, September 2014, Darmstadt, Germany.

P. Moghimian, V. Srot, D. Rothenstein, S. J. Facey, P. A. van Aken, "Induced assembly of M13 phage arrays using carbon thin films" (poster). 18th International Microscopy Conference, September 2014, Prague, Czech.

P. Moghimian, J. Javadpour, S. Afshar, A. Talimian, "An investigation on the phase evolution of calcium phosphate ceramics at low temperatures" (poster), 29th Annual Conference of the Canadian Biomaterials Society, Poster Presentation, Vancouver, BC, Canada.

P. Moghimian, M.H. Khosravi, J. Javadpour, M. Samadani, "A Novel Route for Producing Desired Biphasic Calcium Phosphates" (poster), 8th Congress of Iranian Ceramic Society, May 2011, Tehran, Iran.

Contents

1. Chapter 1. Introduction and Motivation

1.1. Bacteriophages

Bacteriophages or phages are viruses infecting bacterial host cells.[1,2] The name "bacteriophage" is a synonym of "bacteria eater" implying that once a bacteriophage infects the bacterial host, the virus uses the resources of the bacterial host cell to fabricate many copies of itself (*i.e.* to replicate).[3,4] Phages are among the most common organisms on earth. They constitute a protein capsid surrounding and guarding the genomic material (deoxyribonucleic acid (DNA) or ribonucleic acid (RNA)) in a single-stranded (ss) or double-stranded (ds) form.[2] There are many different kind of phages, each having different DNA/RNA, replication processes, and morphologies.[1] Different groups of phages having different genomic material and morphology are shown in Table 1.

Table 1.1. Different groups of phages classified according to their morphology and genomic material.[5]

Phage Group	Phage Type Member	Morphology	Genome
Inoviridae	M13, fd, f1	Rod-like	ssDNA
Myoviridae	T4, P1, P2	Tailed (long contractile tails)	dsDNA
Podpviridae	T7, P22	Tailed (short contractile tails)	dsDNA
Siphoviridae	λ, T1, T5	Tailed (long non-contractile tails)	dsDNA
Corticoviridae	PM2	Isometric	dsDNA
Leviviridae	MS2	Icosahedral	ssDNA

One important group having single-stranded DNA genomes (inoviridae) appears as long filamentous particles. Phages can be lysogenic or lytic with regard to their replication processes.[2,6] Lysogenic phages inject their genomic materials infecting the host cells. The genetic materials (DNA/RNA) uptake the host cell biosynthetic materials and reproduce the same genetic materials and proteins. Thereafter, the produced proteins are conveyed to the host cell membranes, where new phages, without disruption of the host cell walls, are loaded and released. In contrast, some phages undergo lytic infectious cycles that are replicated and in-grouped inside the host cells rather than at the cell membrane.[6] When the replication process is accomplished, the newly amplified phages break the host cell wall and are able to infect other host cells. The infection here results in a fast lysis of the cell within a short time (typically within minutes or hours). The process of releasing of new infectious viruses can be repeated as long as a sufficient number of bacterial hosts are present to support replication.[3] All phages have the ability to produce exact copies of themselves within completely credible structural exactness, regardless of differences in shape, composition and life cycle.[1,2] It has

been reported that temperature and pH are two important factors influencing not only the phage infection but also the host cell growth.[7] There are different morphologies of phages such as filamentous (M13, fd) or icosahedral phages (MS2) (Figure 1.1a-c). There are some sophisticated phage morphologies such as T4 phages that possess a head-tail structure with a cylindrical body (see Figure 1.1b). The length of the packaged DNA is a dominant factor on determining the length of the phages.[8] The Ff class of phages (M13, fd and f1 phages) have been in wide use for a variety of applications in biotechnology as biomimetic matrix for tissue engineering and also as biological templates for material design.[9] Phages offer nanoscale scaffolds for the construction of hybrid and complex structures for optical or electronic applications. Their shape, monodispersity and anisotropy provides material scientist with modifiable surfaces for the fabrication of such hybrid structures. Owing to these features, phages are great candidates for the development of novel bionanomaterials.

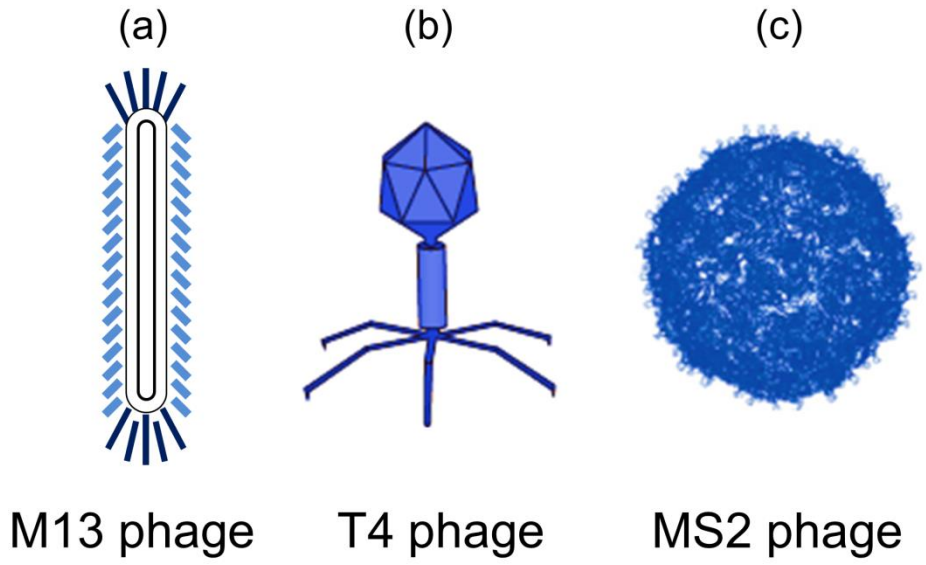

Figure 1.1. Schematic illustration of different phages morphologies. (a) Schematic diagram of rod-like structure of a filamentous M13 phage. (b) A T4 phage with connected head-tail structure having a cylindrical body. (c) A MS2 phage with an icosahedral structure. Adapted from Ref. [2], Copyright 2011, with permission from Elsevier.

Besides, phages play important roles in biology and ecology.[6] These include the use of phages as molecular model in the study of organismal ecology and evolutionary biology, as molecular tools (including phage display technologies) or indicators and tracers and their use in bacterial identification.[1,6]

1.1.1. M13 Phage

M13 phage is a negatively charged and non-pathogenic virus. It has a long filamentous shape that is approximately 880 nm in length and 6.6 nm in diameter with an aspect ratio $L/d \approx 130$, (where L is its contour length and d is its diameter).[10,11,12] The M13 phage shows liquid crystalline behavior in suspensions owing to its high aspect ratio.[13,14] M13 phages are categorized under the Ff class of inoviruses (M13, fd, f1) that have been the focus of extensive research due to their capability of self-assembling into liquid crystal structures. The M13 phage is stable under a wide range of temperatures (between 90 °C and –20 °C) and pH values (between 2 and 9) and therefore has attracted attention for the use in technological applications.[9,15,16] The virus body consists of ~2700 identical

copies of the helically arranged major coat protein pVIII, which exhibits chemical specificity to some inorganic materials.[17,18] It also contains a smaller number of different minor coat proteins at its ends; 5-7 copies per particle of the minor coat proteins, pIII, pVI, pIX, and pVII.[1,7,15,19] pIII and pVI are located at one end, while the pIX and pVII cap the other end (see Figure 1.2a). The major capsid protein wraps around an ssDNA. A schematic illustration of the major coat protein subunits having five-fold helical symmetry (72 degrees of rotational symmetry around the central helical axis) is shown in Figure 1.2b. The proteinaceous coat provides the structural stability, while pIII is necessary for host cell recognition and infection, and therefore is required for the initiation of assembly. pIII is the largest (406 amino acids) coat protein, which contains three distinct domains and therefore is considered as the most complex coat protein.[2,20]

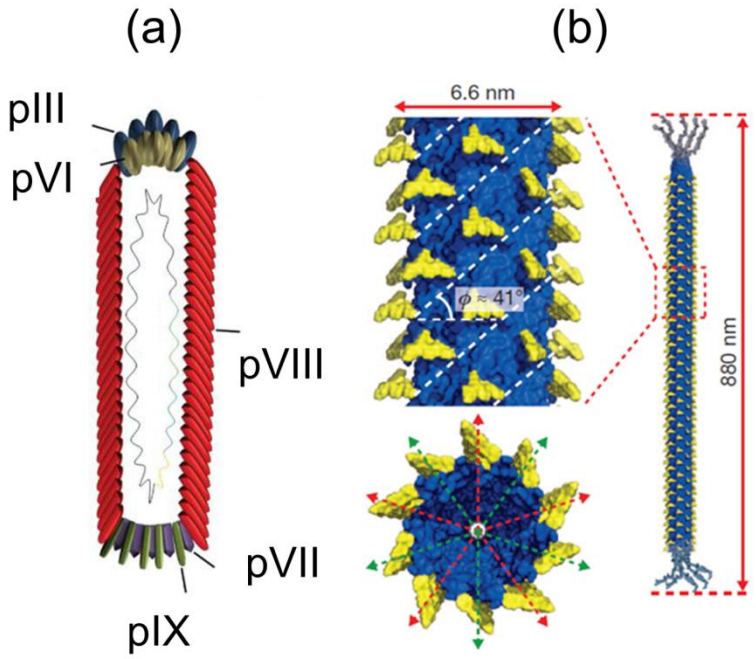

Figure 1.2. Schematic illustration of (a) M13 phage coat proteins [21] and (b) helically arranged major coat protein (pVIII) subunits having five-fold symmetry (*i.e.* the angle between the red or green arrows is 72 degrees). Adapted by permission from Macmillan Publishers Ltd: Nature, Ref. [14], copyright 2011, and from Ref. [21], copyright 2012, from the Chemical Society of Japan and Wiley-VCH, Weimheim.

The pVIII coat protein of M13 virus is comprised of 50 amino acid residues in a sequence that has a highly hydrophobic core and a negatively charged N-terminal domain and a basic positively charged C-terminal region (see Figure 1.3).[22] The N-terminal domain translocates the viral DNA during infection into the Escherichia coli (E. coli).[4] The C-terminal domain deals with the interaction with other phage coat proteins, and is thus responsible for the integration of pIII into the phage body.[19] The M13 phage is sorted in the non-lytic bacterial virus category, implying that it does not destroy the bacterial cell membrane upon release, but instead is secreted through a protein pore channel in the bacterial membrane.[2] Due to the increased phage demands of metabolism during phage production, bacterial host growth is lowered down but continues after infection. These properties enable bacteriophage mass amplification in bacterial culture.[4] Over the past two decades, owing to the phage genetic engineering and approaches of synthesizing site specific organics, the phage biochemical structure has been greatly flourished.[19,23] By exploitation of genetic engineering, each sequence of coat proteins can be modified by altering the viral DNA or integrating foreign DNA into phage genome.[20]

In phage-display technique, combinatorial peptides can be expressed as fusions to a capsid protein (*e.g.* pIII or pVIII) on the surface of viral particles. In this method, the M13 phage has been the most commonly used vector.[21] Using phage-display technique the expressed peptide or proteins can have interactions with desired targets in a way that the recombinant viral particles are stable. pIII and pVIII have been mostly used to display peptides.[21]

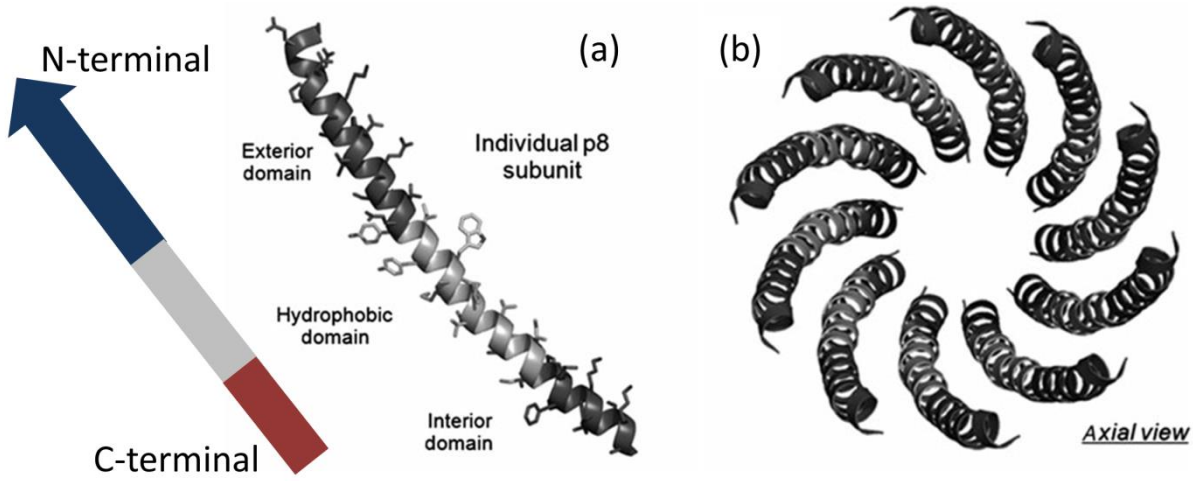

Figure 1.3. (a) Schematic side-view of a single pVIII (p8) subunit showing the exterior solvent-accessible domain (N-terminal), the hydrophobic core and the basic interior domain (C-terminal). (b) Schematic axial view of a the assembly of p8 subunits in a phage particle. Reprinted with permission from Ref. [24], Copyright 2014, Taylor & Francis.

Additionally, novel reactions that allows for site-specific modification of phage body with chemicals such as fluorescent dyes or chromophores for various applications including biochemical imaging and energy harvesting have been developed.[1,2]

1.2. Liquid Crystals and Self-Assembly

1.2.1. Liquid Crystals Fundamentals

Some condensed matter phases have more order than liquids but less than crystals. These phases are grouped together and called liquid crystals since they exhibit both liquid and crystal properties simultaneously (see Figure 1.4a).[25] The molecules in liquid crystals are free to flow like in liquids, however as they do so, they tend to remain their orientational order in a certain direction.[26] This order is not as perfect as in crystals, therefore a new phase or state of matter is attributed to them: liquid crystals. The molecules in a liquid crystal phase do not maintain their direction of orientation all the time because they move around freely. Therefore, to quantify the degree of orientational order inside a liquid crystal phase, an arrow is assumed in the liquid crystal as an average representing the direction of the molecules, called the director. At every snapshot of the molecules in liquid crystal phase, the molecules are oriented at a degree θ with respect to the director (Figure 1.4b). The function $S = (3\cos^2\theta - 1)/2$ (*i.e.* the order parameter) gives the average of the angle of all the molecules with respect to the director. In a liquid crystal with a perfect orientational order, this average becomes

1 and in a liquid crystal with no orientational order this function gives an average of 0. The average of the aforementioned function is called the order parameter (*S*). We should keep in mind that these arrangements occur in three dimensions in a bulk liquid crystal.

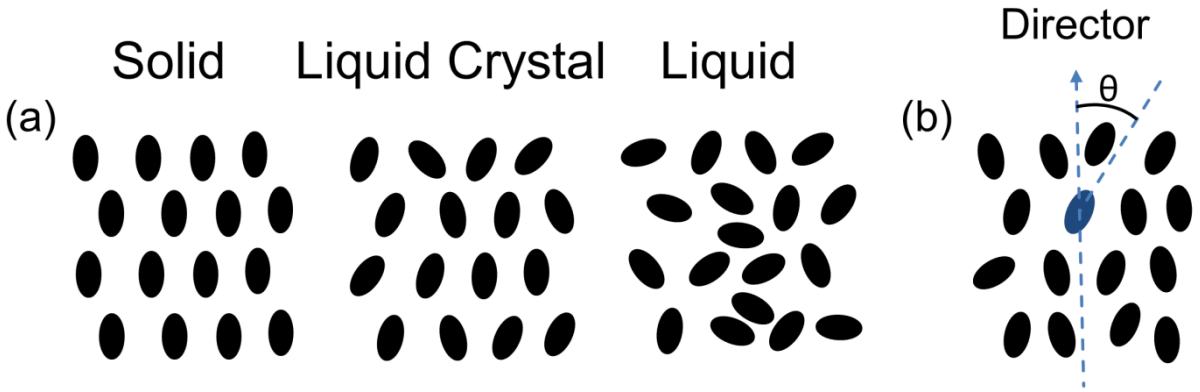

Figure 1.4. Schematic illustrations of (a) solid, liquid crystal and liquids phases of matter. (b) A snapshot of the molecules in a liquid crystal phase showing a preferred degree of orientation of the molecules (having an angle θ) according to the dashed arrow (the director). [26]

The liquid crystals are generally divided into two categories: the thermotropics and the lyotropics. The thermotropic liquid crystal phases are formed by a change of temperature, and the lyotropic liquid crystal phases are influenced by the concentration of the solvent. The lyotropics (*e.g.* M13 or fd filamentous viruses) that show different phases according to their concentration are of high interest in biological studies.[27] The thermotropics are generally distinguished with respect to the shape of the constituent molecules, being called *calamatic* for rod-like and *discotic* for disk-like molecules.[28,29] To date, there have been more than 80,000 different reported compounds that showed liquid crystal properties.[28]

1.2.2. Textures and Defects in Liquid Crystals

Many filamentous viruses have been extensively studied as lyotropic liquid crystalline model systems due to their monodispersity and long rod shape.[15,30,31] The variables such as concentration and external fields (*e.g.* electric and magnetic fields) have critical effect on their ordered liquid crystalline structures.[31,32,33] At low concentrations ($<$ 5 mg/ml), phages are ordered randomly in an isotropic liquid crystalline phase (isotropic). With increasing concentration (ranging from 10–20 mg/ml), the ratio between the viral length to the distance between neighboring viral particles will become larger. The virus particles start to align themselves into orientationally ordered configurations (nematic phase).[34] Going beyond the nematic concentration range (*i.e.* ~5-20 mg/ml), and with increasing the concentration in the range between 20 and 80 mg/ml, phages start to intertwine with each other and thus generating distinguishable periodic structures (helicity of the particles), which show finger print structures in the polarized light micrographs (chiral nematic or cholesteric phase).[34,35] Above 100 mg/ml, the viral particles attain positional order in addition to the orientational order along a direction (smectic phase).[32] These liquid crystalline phases are shown in Figure 1.5. The aforementioned structures are all being considered in 3D bulk samples. However, some viruses such as M13 and fd phages have been also used at high concentration ranges to grow two-dimensional ordered viral films.[36,37]

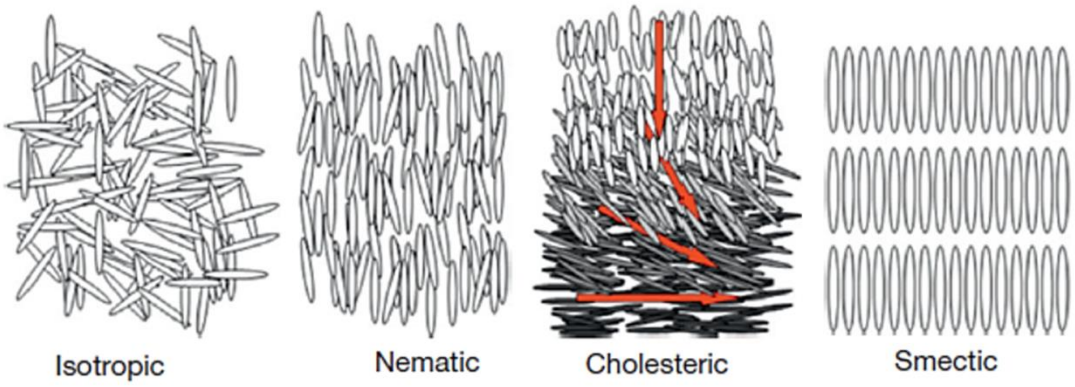

Figure 1.5. Schematic diagram of different liquid crystalline structures of M13 phages. Adapted with permission from Ref. [2], Copyright 2011, Elsevier.

In general, the orientation of M13 viruses onto a substrate depends on the concentrations of the particles, external forces, biomolecular interactions between the virion particles, and molecular stiffness.[17,38] Directional assembly of M13 phages on solid surfaces was obtained by a control of interactions between the phages and substrate surfaces.[39,40] Various approaches have been undertaken to develop such well-defined virus layers. Sawada *et al.*[31] have successfully immobilized M13 phages onto a poly(methyl methacrylate) (PMMA) film by a dipping/sweeping method. They have reported that a higher sweeping-up speed leads to a higher orientational order of phages due to the higher capillary forces at the meniscus. Yoo *et al.*[17] reported that M13 phages can be ordered through an interaction with weak polyelectrolytes. By tuning the concentration of the phage solution, phages could be immobilized on the gold substrates in a controlled process. Moreover, a variety of inorganic nanocomponents were organized into ordered films/fibers (2D/1D) using a phage self-assembly process combined with the peptide display technique.[38] For instance, by exposing the M13 phage pIII coat protein to zinc sulfide (ZnS)-specific binding peptides, ZnS nanoparticles (NPs) were organized into a hybrid film at the nanoscale.[41] Using pVIII engineering of viruses, viral composite films (composed of FePt, CoPt, *etc.*) were fabricated.[2,37] In addition, using a layer-by-layer deposition, ordered virus-templated thin films integrated with semiconductor (GaN) and metallic (Au) nanoparticles have been generated on multilayered electrolyte polymer films.[2] Phages can also be used for the assembly of biological tissues.[2,42] For example, hydroxyapatite (HAP) has been ordered into self-assembled phage nanofibers through the electrostatic interactions between the calcium ions and the genetically engineered M13 phages.[43] Ordered structures over a large scale, have a number of advantages in improving the properties of the resulting structures. It has been reported that the directionally organized structures on ordered organic building blocks can enhance the magnetic and electric properties regardless of the properties of the building blocks.[35,44]

However, the director does not point in the same direction at all points of a nematic liquid crystal sample. There are always certain areas of the sample, at which the director might point in different direction compared to its vicinity and therefore at these locations, no directors can be assumed in the liquid crystal. There is often a place between these two areas, at which the director suddenly changes its pointing direction. This location is called a defect in the order of the liquid crystal. [26] The important types of defects are point defects and line defects. The abrupt change in the director orientation imposes a severe distortion of the configuration around the defect. The fact, that the defects remain in the sample and are stable, is, because this is the best possible compromise between the outside forces (*e.g.* electric field, nearby surface, *etc.*) and the director configuration.[26]

Point defects are less common than line defects. As an example, point defects might appear in a thin capillary tube in which the molecules must orient themselves perpendicular to the cylindrical surface of the tube. A diagram of a capillary tube is shown in Figure 1.6 where two point defects with the strength $S = -1$ and $S = 1$ are depicted. This means that the two point defects with the same strength but different signs can combine and cancel each other. This is similar to, when two opposite electric charges cancel each other.[26]

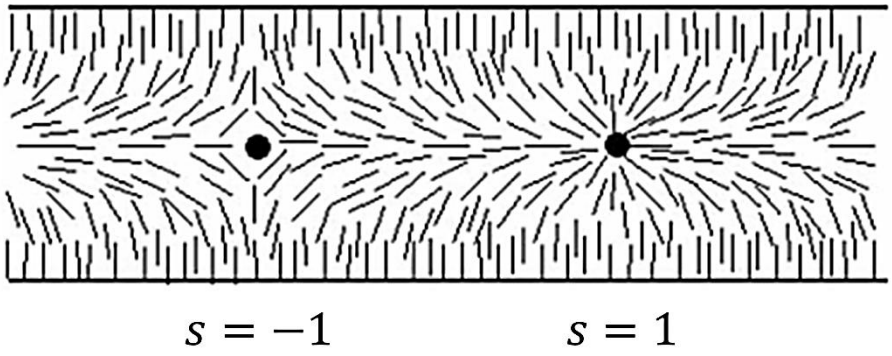

Figure 1.6. Point defects $\boldsymbol{S = -1}$ and $\boldsymbol{S = 1}$ in a capillary tube. Reprinted with permission from Ref. [45], Copyright 2006, Taylor & Francis.

There are also possible line defects which might be present along the center of the capillary tube. These line defects are called disclinations implying that the line represents a discontinuity in the inclinations of the director. Four examples of many different disclinations are shown in Figure 1.7, in which the direction of the disclinations lines is perpendicular to the page plane. One important feature of these defects is that all disclinations with integer strength, whether positive or negative, are not stable and can always relax.

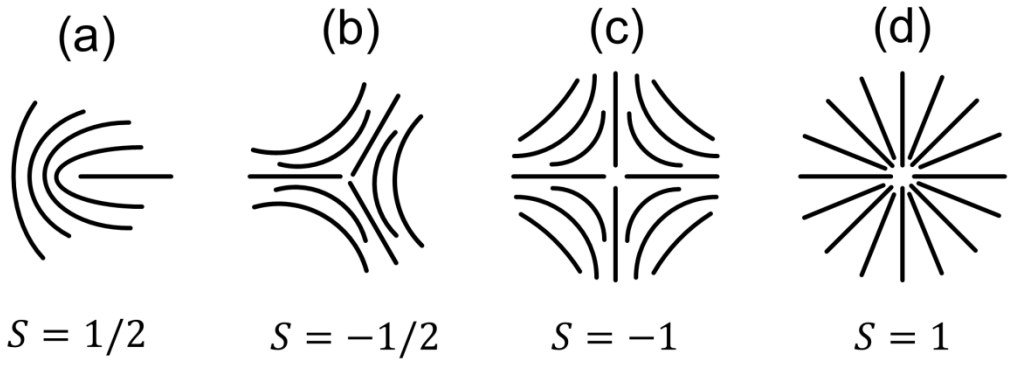

Figure 1.7. (a)-(d) Schematic illustration of four different types of disclinations. The numbers imply the strength of the disclinations.[26]

Defects in cholesteric and smectic liquid crystals are different from those occurring in nematics due to their twisted or layered structure. These liquid crystals phases can deform in many ways, but the most complicated situation is one that changes the pitch (*i.e.* the distance it takes for the molecules to undergo a full 360° twist) of the phases which occur in fact very rarely.

1.3. Bio-Inspired Organic–Inorganic Hybrid Structures

Biomolecules such as phages have been widely used as building blocks and templates for the synthesis and assembly of inorganic structures inspiring from the pioneering work of Belcher and co-workers.[46] Due to the capability of biomolecules to self-assemble into ordered structures, a variety of hybrid composites with desired structures and compositions can be constructed.[47] Although proteins are capable of nucleation and growth of a limited class of inorganic materials, the genetic engineering of proteins/viruses has made it possible to trigger the nucleation and growth of a wider range of inorganic materials which opens up a possibility to fabricate a wider range of complex hybrid structures.[47] Chemical functionalities of proteins with secondary molecular forces (*i.e.* hydrogen binding, hydrophobic and electrostatic interactions) have been tailored as scaffolds to construct nanomaterials with defined geometry.[48] To this end, phage display technique has been extensively used to identify peptide sequences, which have the affinity for different inorganic materials.[36,49,50] This has been used to obtain particular binding between organic and inorganic materials.[1,51] Construction of many interesting functional nanomaterials and nanostructures has been made possible through genetic engineering of functional peptides with crystal nucleation and growth capabilities on phage coat proteins.[52] This is of high importance, because selectivity has been a major problem in the synthesis of multicomponent materials. In nature, specific binding proteins which have the affinity toward various inorganic crystals are being used to synthesize hybrid organic–inorganic materials, such as silica in diatoms, calcium carbonate in abalone shells, or calcium phosphate in bones and teeth.[42] Studies of Belcher and co-workers showed that a genetically engineered phage can specifically recognize inorganic semiconductor substrates and binds to them. The functionality of pIII and pVIII coat proteins of phages can be rationally modified via genetic engineering. For instance, it has been demonstrated that phages can be genetically engineered with gold (Au)-binding peptides on the pVIII (capsid) and streptavidin-binding motifs at pIII (one end of the virus) to assemble Au and cadmium selenide (CdSe) nanoparticles into ordered arrays.[53] Courchesne *et al.*[54] fabricated a hybrid nonporous network using complexation of M13 phages with gold nanoparticles and further biomineralization of crystalline titania. Jeong *et al.*[55] presented a nanogenerator composed of barium titanate ($BaTiO_3$) nanocrystals synthesized on arrays of pVIII-engineered M13 phages. Chen *et al.*[56] assembled TiO_2 nanowires into semiconducting structures using M13 phage as template. Phages can also nucleate gold and metal oxides simultaneously. This work has been done by Nam *et al.*[51] by inserting multiple major coat protein genes in the phage genome. Using simultaneous modifications of pIII and pVIII coat proteins, a variety of phage-templated nanostructures have been successfully constructed.[42] Three coat proteins, which are on both ends and major coat protein, could be engineered and thus phages can be employed to perform multiple operations. Such engineered phages are expected to open the way for self-assembled, self-interconnected, self-fabricated electronic devices.[37,57] Wild-type (WT) phages have been also used as templates for the fabrication of hybrid organic–inorganic materials. Metallic nanoparticles such as Au and platinum (Pt) were deposited on WT tobacco mosaic virus (TMV) viruses. The Raman spectrum of such a decorated TMV showed a slight shift indicating the specific interaction between the coat protein of the virus and the nanoparticles.[48] Moghimian *et al.*[58], as a part of the current thesis, constructed bilayered nanostructures of WT M13 and zinc oxide (ZnO) materials which contained alternating organic–inorganic layers on a carbon-coated silicon substrate. However, using WT virus templates to grow hybrid organic–inorganic structures has some drawbacks. First, only a certain class of inorganic materials could be templated by WT virus templates. Second, WT virus templates often have weak binding to the inorganic nanoparticles and the nanoparticles might detach from the coat proteins under harsh environment.[48]

1.3.1. Biomineralization of Zinc Oxide

Biomineralization is a nature-inspired process of inorganic nanomaterial nucleation and growth with controlled structures that relies on bioorganic molecules such as proteins and peptides.[59,60,61] Biomineralization has been used to create functional nanomaterials due to its advantages that include ambient synthetic conditions and diversity of inorganic and peptide combinations available.[59] The process of biomineralization is often attributed to genetic modification and this control allows for the production of structures with physical and mechanical properties fit for function. For such biomineralized structures, molecular recognition between the organic and inorganic materials is crucial. Recognition can be due to electrostatic interactions, hydrogen bonding, hydrophobic effect or a combination of them.[61] It is important to note that the physico-chemical properties of inorganic nanoparticles are defined both by their size and shape, which can be significantly different from those of the corresponding bulk material.[62]

Recently, there has been high interest in the field of electronic nanodevices to synthesize semiconductor nanowires with controlled size and morphology. ZnO is a highly promising semiconductor (band gap energy of 3.37 eV) which is a great candidate for functional applications such as ultraviolet light emitters or transistors.[63,64] Based on the reaction conditions, different morphologies of ZnO can be synthesized such as nanorods and nanorings.[65] Highly anisotropic viruses, such as M13 phage, could be exploited as attractive scaffolds for ZnO nanowires, which can offer linearly assembled structures of ZnO directed by the coat proteins of the virus in solution.[63] This method has several advantages including low synthesis temperature and neutral pH of the reaction condition.[65]

1.4. Thesis objectives and Structure

This thesis focuses on the controlled 2D self-assembly of rod-like and semi-flexible M13 phages on flat/unstructured and also on structured surfaces. This work is motivated by the need for fine control of the morphology of biomolecular scaffolds in the rapidly developing virus-based technology. The increasing need of obtaining a controlled structure of organic–inorganic hybrid components, places the focus of this thesis first on the study of the influence of different kinds of surfaces (and their surface properties) and different surface morphologies on the assembly of these biomolecules. Starting with examining the stability of M13 phages in organic solvents, this work is then expanded to the use of the resulting ordered organic layers to template metal oxide nanoparticles (ZnO) and to further construct layer-by-layer (L-b-L) organic–inorganic hybrid structures and to investigate their microstructure, elemental composition and integrity of the structures. Constructing such multilayered structures is a bio-inspired approach which tailors the unique properties of protein arrangements on the elongated nano-viruses for the selective mineralization of inorganic components. An overview of the scope of this thesis is presented in Figure 1.8.

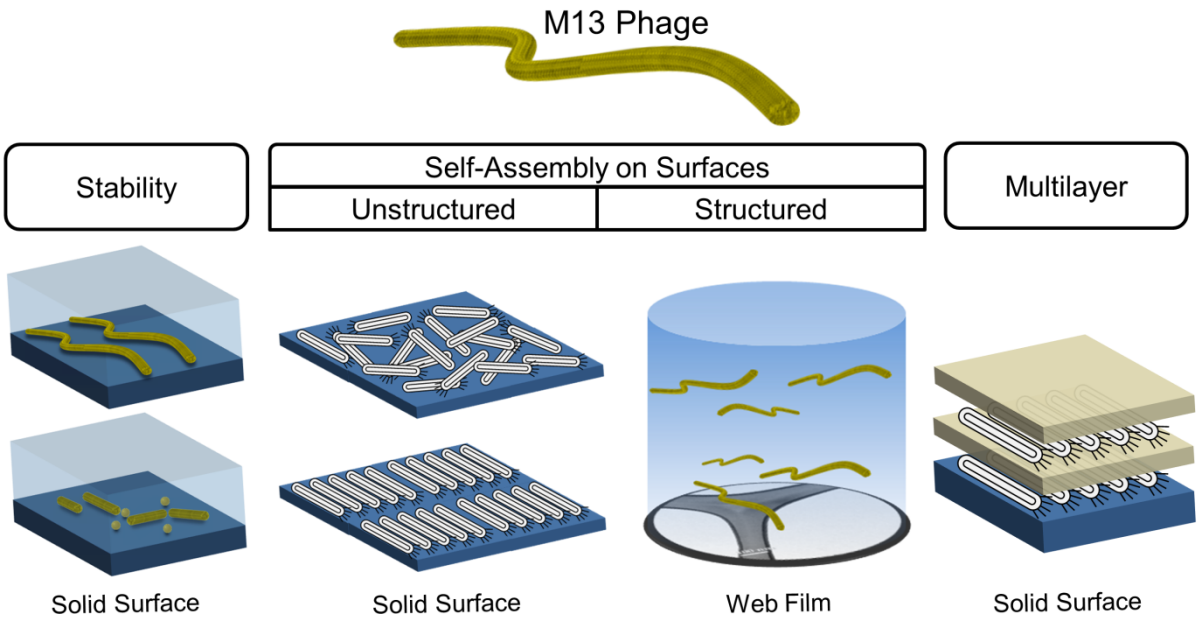

Figure 1.8. Structure of this thesis: Beginning with the structural integrity and stability of filamentous M13 phages when exposed to different organic media, as the first step, to understand the structural behavior of these macromolecules. Next, the adsorption and self-assembly of phages was investigated on flat (*i.e.* unstructured) and web-like (structured) surfaces. Finally, phages were employed as a soft scaffold for the layer-by-layer bio-mimetic fabrication of hybrid organic–inorganic structures, where inorganic nanomaterials are templated by the organic component.

2. Chapter 2. Characterization and Experimental Techniques

In this thesis, the following electron and atomic force microscopes were used to perform transmission electron microscopy (TEM), scanning electron microscopy (SEM) and atomic force microscopy (AFM).

The conventional Zeiss 912 Omega 120 kV TEM with a LaB_6 gun equipped with an Omega (Ω) in-column energy filter and a Noran energy-dispersive X-ray spectroscopy (EDX) system.

The Zeiss Sub-Electron-Volt-Sub-Angstrom-Microscope (SESAM), a high-resolution 200-kV field-emission gun (FEG) TEM microscope equipped with an electrostatic Ω-type monochromator, the in-column MANDOLINE filter, and an EDX system (EDAX, Mahwah, NJ, USA).

The JEOL ARM200F (JEOL Co. Ltd) atomic-resolution TEM equipped with a cold FEG, a DCOR probe Cs-corrector (CEOS Co. Ltd.), a 100 mm^2 JEOL Centurio SDD-EDX detector, the Thermo Noran System 7 EDX system (Thermo Fisher Scientific Inc.) and a Gatan GIF Quantum energy filter. The system is set up for operation at voltages of 30, 60, 80 and 200 kV.

The Zeiss DSM 982 Gemini, a FEG SEM equipped with an secondary-electron (SE) in-lens detector and an EDX detector (Thermo Noran Voyager 3105A) enabling imaging (secondary electrons and backscattered electrons) and elemental analysis. The accelerating voltage is adjustable from 0.2 to 30 kV.

A Nanoscope III Multimode instrument AFM (Digital Instruments, Inc., Santa Barbara, CA, USA) equipped with a silicon tip operating in tapping mode in air. AFM images were analyzed using the WsXM software.

A Krüss G10 contact angle goniometer (Krüss GmbH, Germany) was used to measure the contact angles and to investigate the hydrophobicity of solid substrates.

All the instruments and characterization techniques are discussed in more detail in the current chapter.

2.1. Scanning Electron Microscopy

The invention of scanning electron microscope (SEM) was soon after the transmission electron microscope but took longer time to be developed for scientific research.[66] Only after substitution of magnetic lenses for electrostatic ones and after addition of stigmators to the lens column, the spatial resolution of the instrument improved. Today, the number of existing scanning electron microscopes is more than of transmission electron microscopes and are used in many fields, including medical and materials science research.[67] Figure 2.1 shows a schematic diagram of a typical SEM.

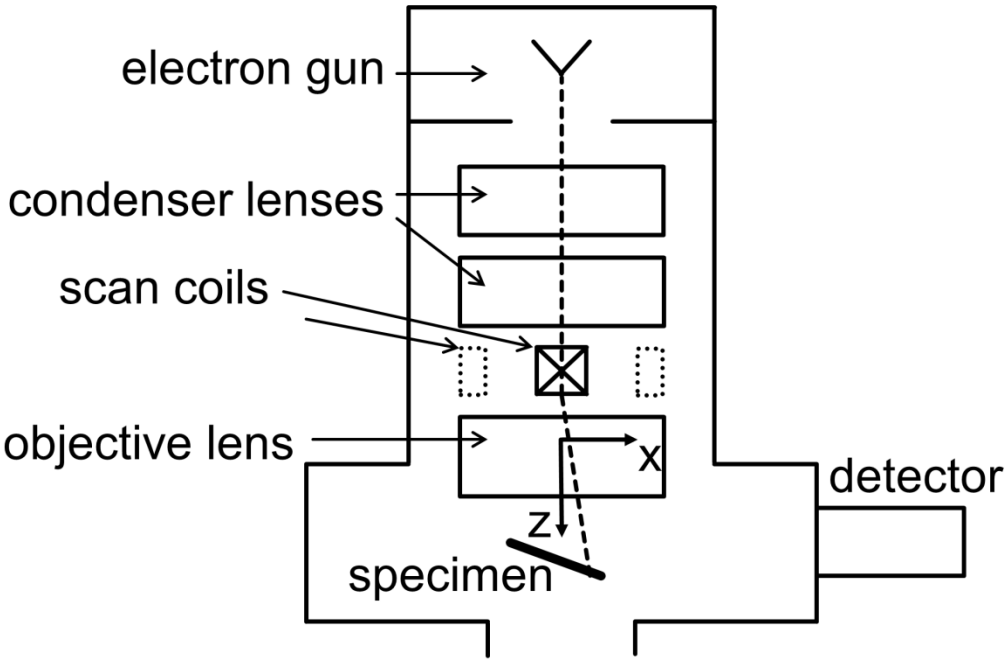

Figure 2.1. Schematic diagram of a scanning electron microscope (SEM).[66]

2.1.1. Principles of SEM

The SEM electron sources can be tungsten filament, LaB_6 or Schottky emitter, or a tungsten field-emission tip. In SEM, the electron gun is smaller comparing with TEM, requiring less insulation because the maximum accelerating voltage (typically 30 kV) is lower than for a TEM. Magnetic lenses used in SEM are also smaller than those employed in the TEM; this is due to the fact that the electrons of lower kinetic energy do not need a strong magnetic field generated by polepieces. There are also fewer lenses in SEM and imaging lenses are not required in this case.[66,67]

Above the sample in the SEM column, there are two or three lenses. The diameter of the incident beam in the SEM (*i.e.* the electron probe) is typically ~10 nm and with a field-emission source it can reach to ~1 nm. The final lens responsible for forming this extremely small probe is named the objective lens; this lens performance (including aberrations) substantially determines the resolution of the microscope. The resolution can never be higher than the incident-probe diameter when an image is acquired in SEM.[66] The electron probe of an SEM is horizontally scanned across the

specimen in *x* and *y* directions (*i.e.* raster probe). The *x*-scan is relatively fast. However, the coils above the objective lens create a magnetic field in the *y*-direction, applying a force on an electron (moving in the *z*-direction) that deflects it in the *x*-direction (see Figure 2.1.). Therefore, the *y*-scan is much slower than the *x*-scan. The whole procedure is sometimes referred to as raster scanning due to the rectangular covered area of the specimen by the electron beam.[66]

2.1.2. Interaction of Electrons with a Solid

When accelerated electrons penetrate a solid bulk, they get scattered both by electrostatic interaction with atomic nuclei (*i.e.* elastic scattering) and by interaction with electrons (*i.e.* inelastic scattering). Most of the inelastic scattering is followed by electron deflection angles of less than 90° that is called "forward" scattering. But a small fraction of the primary electrons are elastically backscattered by deflection angles of $\theta > 90°$ which lose only a small fraction of their energy. Because of their high kinetic energy, the backscattered electrons have a high chance of leaving the specimen and entering the surrounding vacuum and then they can be further collected and contribute to the backscattered electron (BSE) signal. Inelastic scattering consists of small scattering angles and therefore contributes mostly to the image noise and little to the backscattered signal. However, until the primary electrons are brought to rest and absorbed into the solid, their kinetic energy will be reduced. The depth below the sample surface at which penetration occurs is called the penetration depth or the electron range. The volume of sample at which the scattering of electrons occurs is called the interaction volume and is represented as pear-shaped in cross section (see Figure 2.2).[66] The interaction volume when electrons hit a material with a higher atomic number *Z* is smaller, because the probability of high-angle elastic scattering is proportional to Z^2. In the case of a BSE image, the BSE signal is collected from the BSE electrons which have enough energy to escape the solid depth of about half of the penetration depth. Therefore, BSE images show a contrast indicating different chemical composition of the specimen. It is noteworthy that the interaction volume and the penetration depth are quantities that are averaged for a large number of electrons. The reason is that the behavior of a single electron can be dramatically different from that of other electrons.[66]

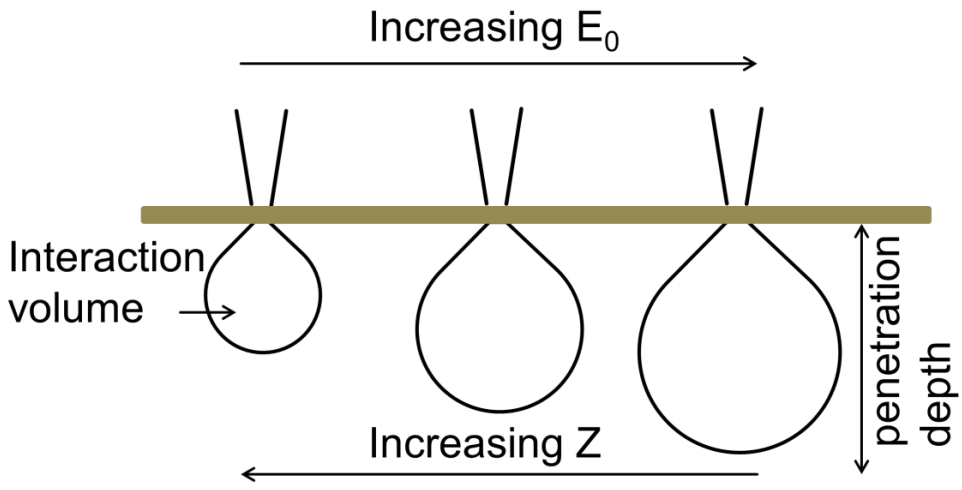

Figure 2.2. Interaction volume dependency on the atomic number *Z* and incident energy of electrons.[66]

There are several interactions between the beam electrons and specimen atoms. Figure 2.3 illustrates the possible signals generated when a high energy electron beam interacts with a thin specimen.

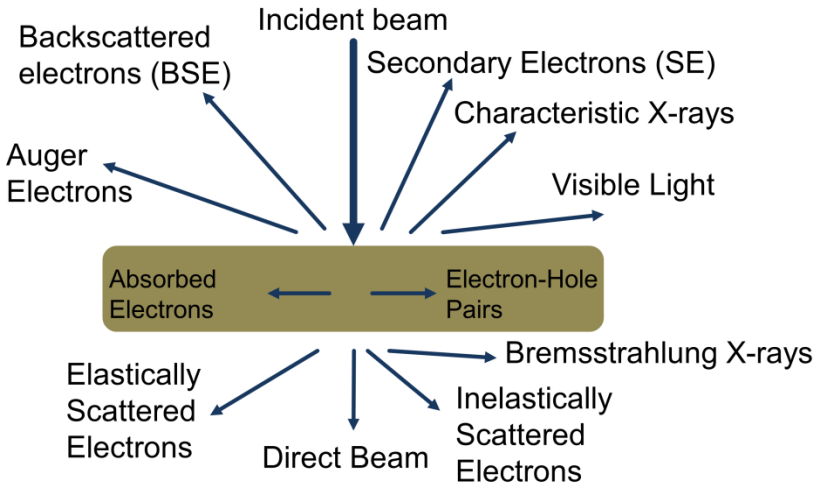

Figure 2.3. Different generated signals when an electron beam interacts with a thin specimen.[68]

2.1.3. Secondary-Electron Images

When inelastic scattering occurs, based on the principle of conservation of energy, any energy lost by a primary electron will appear as a gain in energy of the atomic electrons that made the inelastic scattering happen. If these are the valence or conduction electrons, they are weakly bound to an atomic nucleus and only a small part of this acquired energy will be used up as potential energy, to release them from a particular atom. The remaining energy will be retained as kinetic energy, allowing the electrons to move through the solid as secondary electrons (SE or secondaries). The secondaries themselves are charged particles and therefore can interact with other atomic electrons and be further inelastically scattered and lose their kinetic energy. In fact, the energy of most secondary electrons is less than 100 eV and, due to the inversely dependence of probability of inelastic scattering on kinetic energy, the average distance that a secondary electron travels in the solid is just one or two nanometer. As a result, most secondary electrons lose their kinetic energy within the interaction volume, and consequently have no chance to escape the solid. But those secondaries which have been generated close to the surface might escape into the vacuum. Typically, the secondary electrons which escape from the solid are generated only less than about 2 nm below the surface (see Figure 2.4). The signal of the SE image is collected only from this small depth that is called the escape depth. The SE image is a property of the surface structure (the image displays topographical contrast), because the SE signal used in the SEM is collected from the escaping secondary electrons in the vacuum. It is interesting to mention that the average number of escaping secondaries per primary electron is 0.1 to 10 and it is called the secondary-electron yield (SE yield, δ). The δ value depends on the and also on the primary electron energy E_0 and also on the chemical composition of the surface of the solid. The value δ decreases with increasing E_0, because higher-energy primary electrons undergo less inelastic scattering and thus within the escape depth there will be fewer secondary electrons.[66,69]

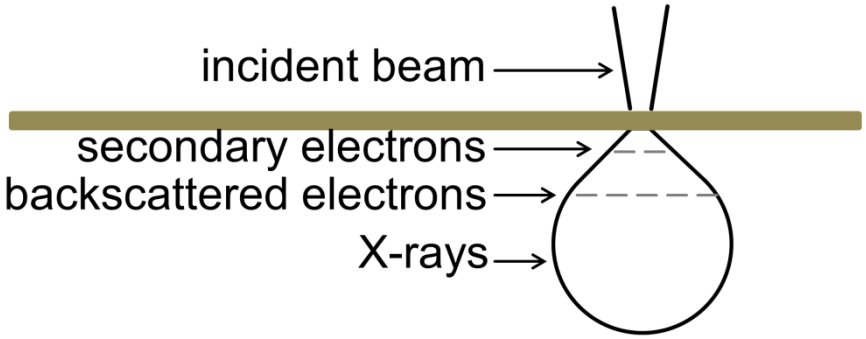

Figure 2.4. Diagram of the interaction volume and the regions from which the different signals may be detected.

The SE detector is usually located to one side of the SEM column (see Figure 2.1). Therefore, surface features appear bright if they are tilted towards the detector, because electrons have a greater probability of reaching the detector if they are emitted from these regions. This fact can be used to distinguish the morphology and topography of the specimen surface.[66]

2.1.4. SEM Sample Preparation

In comparison to TEM, one of the most advantages of the SEM is the ease of specimen preparation, because the sample does not need to be thinned to become electron transparent in prior to the SEM investigations. In fact, before performing SEM on many conducting specimens, they do not need special preparation. Besides, insulating materials do not have a path to ground for the accumulation of static electric charges on the specimen, and therefore they undergo electrostatic charging when bombarded by the electron beam. The charging parts become brighter and brighter in the SEM image. The local negative charges on the specimen causes a serious problem due to their repulsion of the incident electrons and deflection of the scanning probe which can result in image distortion. The charging problem can be solved by sputtering the surface of the specimen with a thin film of a metal (most commonly platinum palladium (PtPd) and gold (Au)) or conducting carbon. This can be performed in vacuum using the evaporation technique for instance. Evaporated carbon has a low SE yield and it has a very small granularity. Therefore, the coating does not conceal real specimen features and also does not appear (as an artifact) in a high-magnification SEM image. Thin evaporated films of thickness ~10 nm can conduct sufficiently to prevent the charging problem of most specimens. But in this case, the SE signal would be collected from the coating rather than from the material. The reason is that the thickness of the coated material is larger than the SE escape depth. However, the external outline of the thin film follows those of the specimen resulting in a topographical image. One should be careful not to lose the surface features while sputtering a surface with very fine features (small troughs or bumps). Here, it is recommended that the coating takes place with a very low thickness (*e.g.* < 1 nm). When sputtering the surface is not necessary, the specimen charging can often be controlled by choosing an optimum SEM accelerating voltage.[70] It should be noted that in this case and by choosing very low accelerating voltage (*e.g.* 0.5 kV), BSE imaging would not be possible because BSE imaging is most-commonly performed under accelerating voltages of 10 kV or higher.[71] Radiation damage is often inevitable especially in biological samples as they are more sensitive to the electron beam. Because, most of the energy lost (due to inelastic scattering) is converted to heat, and therefore samples can be heated up under the electron beam.[72] If the sample is

composed of biological matter, the electron excitation of organic molecules can lead to bond rupture so the organic material can undergo mass loss and decomposition after the electron exposure (*i.e.* radiolysis). However, the damage is higher when the illumination area gets smaller, and that can limit high-resolution studies of biological samples.[66,67,69]

2.2. Transmission Electron Microscopy

Transmission electron microscope (TEM) has the ability to display magnified images of a thin specimen, typically with a magnification ranging from 10^3 to 10^6. Besides, the TEM can be used to acquire electron-diffraction patterns (DPs), in order to analyze the properties of a crystalline specimen or its crystallinity or to perform analytics. This overall property is obtained with an electron-optical system containing an electron gun (in order to produce the beam of electrons) and several magnetic lenses, assembled vertically to form an electron column.[66,68] In transmission electron microscopy, a specimen is required that is thin enough to be electron transparent, which allows for the transmission of required number of electrons through the specimen to produce sufficient intensity in the TEM analysis. When the electron beam interacts with the sample, a projection image is obtained.

2.2.1. Principles of TEM

The electron column of a transmission electron microscope (Figure 2.5) consists of an electron gun and set of 5 or more electromagnetic lenses operating in vacuum.

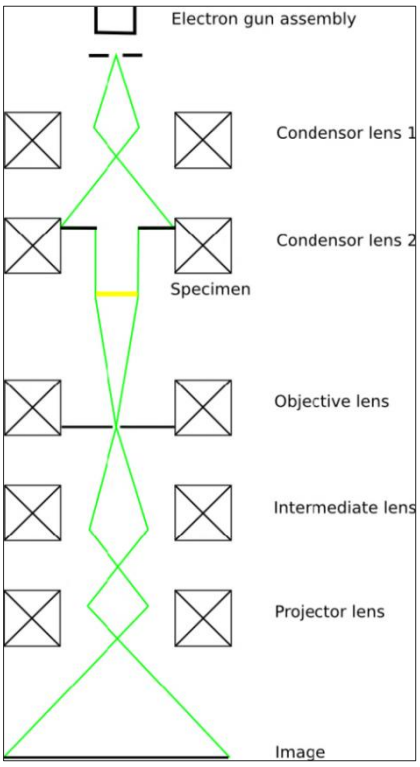

Figure 2.5. Schematic diagram of a transmission electron microscope with a gun assembly, in which a high electrostatic potential is present between the cathode and the anode, and with electromagnetic lenses.[68]

The instrument consists of different sections. The illumination system includes the electron gun, along with two or more condenser lenses that focus the electron beam onto the thin specimen. The diameter of the beam and the intensity in the final TEM image are determined with the illumination system design and operation, because the electron beam passes through a set of condenser lenses focusing the beam of electrons with a desired diameter. The next section consists of the objective lens and the specimen stage at which all of the beam-specimen interactions occur. Here, two fundamental TEM operations take place, that is, the formation of the different kinds of images and diffraction patterns which are further magnified for viewing and recording. The imaging system produces a magnified image or a diffraction pattern of the specimen on a fluorescent screen or on a monitor screen of a camera system. The operation of this imaging system determines the magnification of the TEM image, while the spatial resolution that can be obtained from the microscope, is largely influenced by the design of the imaging lenses.[66,67]

Electron Guns

There are two kinds of electron guns in the TEM, which are known as thermionic gun and field-emission gun (FEG). Thermionic guns produce electrons when their filaments are heated. They were formerly made of tungsten filaments, but nowadays lanthanum hexaboride (LaB_6) is also used. The materials, which have a high melting point with a lower potential function, are the ones preferred for the filament. The sharp tip of the tungsten filament in the thermionic gun is heated up electrically. When a high temperature is reached on the tungsten filament, it allows some of the electrons to gain enough energy to overcome the work function of the tungsten-vacuum interface. Thereafter, the electrons are emitted from the filament.[68] In this way, the temperature of the tungsten filament contributes to the emission of more electrons, but it also causes evaporation of the tungsten filament. Due to this reason, there exists always a limit in maximum operation temperature. In a field-emission gun, the electrons are generated using a high electric potential between the gun and an anode. In order to produce electrons, a sharp tip usually tungsten is used as a cathode because higher electric fields are generated at the sharper tips. Hence, if a very high electric field is generated on the metal surface, the probability of an electron leaving the surface is higher. By this way, more electrons are emitted from a tungsten filament than in that of thermionic gun. In the case that the tip works at ambient temperature or at high temperatures (thermal-energy assisted), the electron gun is called cold FEG and thermal FEG, respectively. Schottky emitters are thermal FEGs in which the tungsten tip is coated with a layer of zirconium oxide for better conductivity at higher temperatures.[68]

Electromagnetic Lenses

The lenses are the prominent components in the transmission electron microscope, which enables the use of the electron beam in order to form images in the TEM or to focus the beam into a spot. Electron lenses are placed beyond the electron gun. The function of the lenses is to transform a point in an object to a point in an image and to focus parallel rays to a point in the focal plane of the lens. Electrons can be focused by two means; electrostatic or magnetic field. In an electromagnetic lens there is a cylindrically symmetrical core of soft magnetic material such as soft iron (polepiece), with a hole drilled through it (the bore of the polepiece). The second part of the lens is a coil of copper wire which surrounds the polepiece. When we pass a current through the coil, a magnetic field is created in the bore.[68]

The electron rays can be simply divided into two sections; electron rays that are close to the optical axis, which form an image of the object with correct shape and position, and also the electron rays, which are sided to the optical axis and do not come to focus at the correct position, causing a

blurred image called aberration. The aberrations can imperfect the lens operation and three major aberrations are the spherical aberration, chromatic aberration and astigmatism. Together they influence the lens performance and are responsible for the final image resolution obtained in the TEM. Spherical aberration appears due to the trajectories of the electrons, which are far away from the optical axis, and therefore get bent more heavily by the magnetic field than those close to the axis. This process leads to an enlarged blurred image of a point in the image plane. In electron microscopy, the main goal is to form a monochromatic electron beam (with a single wavelength). However, in practice, the power supplies engender the electron energy variance. These variations are small and they do not cause substantial problems in the microscopes. The energy fluctuations are usually due to the spread in the energy of the electrons generated by the electron gun. In TEM, in addition to the power source which causes the energy spread, the interaction of the electron beam with the specimen also lead to the generation of electrons with different wavelengths. All of these cause a distortion in the final image in the TEM called chromatic aberration. In TEM, the energy absorption in the specimen can produce a significant change in primary electron energy, which will introduce substantial distortions in the image. Deviance from rotational symmetry is typical for the electromagnetic lenses. This defect is caused by the asymmetry in the windings and contaminated apertures. A circular asymmetrical lens will cause electrons to divert from a point object to be focused at the image at two separate lines of foci. This effect can be realized by the stretching of the image in two perpendicular lines when the objective lens is underfocused and then overfocused, respectively. By using a stigmator, which is an octuple of small electromagnetic coils generating a weak magnetic field to remunerate the lens distortions, the astigmatism can be corrected.[66]

In TEM there are two or more condenser lenses which are positioned below the electron gun. Condenser apertures are placed between the condenser lenses. The condenser system allows for the control of the spot size and the beam convergence angle.[73]

The TEM specimen in a form of a thin foil, section, or fine particles transparent to the electron beam is located beyond the objective lens. At the specimen surface, an image of the electron density distribution is formed by the objective lens.[66] A diffraction pattern is generated in the back focal plane of the objective lens and then the combination of the diffracted beams forms an image in the image plane of the objective lens. The projection and intermediate lenses below the objective lens are used to focus and further magnify the image or the diffraction pattern onto the viewing screen. An ultimate magnification is reachable by the use of these lenses each capable of a magnification of up to twenty times. The first projector lens in the column is generally named as intermediate lens, which can switch between the image mode and the diffraction mode. In diffraction mode, the intermediate lens is focused on the back focal plane of the objective and the diffraction pattern is projected onto the viewing screen.[73] To attain quantitative information about the materials microstructure, the TEM can be employed to generate several image types or diffraction patterns obtained from desired regions of the specimen.[68] An objective aperture is situated near the objective lens. The aperture limits and controls the collection angle of the lens and therefore the angular spread of the electrons.

The fluorescent screen made of a disk coated with doped zinc-sulfide is placed at the bottom of the electron column. It emits green light upon impingement of the electron beam onto the screen. The intensity of the green light is directly proportional to the intensity of the electron beam.[68] A camera is mounted below the viewing screen to record the images which detects the incident electrons. Nowadays, charge-coupled device (CCD) array cameras are widely used in electron microscopes, and have become a standard for recording images and diffraction patterns in real time TV mode. CCDs are devices made up from metal-insulator-silicon, being capable of storing the charges created by electron beams or light.

Some microscopes can be equipped with energy filters, which substantially enhance the quality of images and diffraction patterns, particularly in the case of thick specimens where the frequency of occurrence of inelastic scattering is higher. The energy filter is positioned between the intermediate and the projector lenses in the TEM column below the specimen. The energy filter removes the inelastically scattered electrons and permits the scattered ones to travel down the microscope column with specific amount of energy loss.[68]

Contrast Mechanisms

The most important mechanism, which takes part in the image contrast formation in the TEM, is mass-thickness contrast. This contrast originates from incoherent elastic scattering of electrons. As electrons penetrate the specimen they are scattered by elastic nuclear interaction. The atomic number determines the cross section for elastic scattering. As the specimen thickness increases the elastic scattering also increases since the mean-free path remains constant. Therefore, specimens consisting of higher atomic number elements *Z* will scatter more electrons than those of having lower *Z*. Hence, the image formed from thicker regions appears darker due to the less electrons transmitted from that region. However, the image formed from the thinner area, appears brighter in the image plane due to the less scattering occurred in that area. This will create differential intensity in an image.[66] Mass-thickness contrast is the main imaging mechanism in biological applications.[68]

Contrast in TEM images can be also due to the electron waves phase difference, which are scattered through a specimen. Whereas bright- and dark-field TEM modes usually use only the direct beam or a single diffracted beam, the phase contrast method uses the interference of two or more beams. There is a small phase difference due to the scattering in the specimen while the electrons leaving the bottom surface of a thin specimen. Phase contrast imaging is the basis for the so called high-resolution TEM (HRTEM). Phase contrast contains important information of the material and provides information of the periodically ordered part of the crystals.[68]

Energy Dispersive X-ray Analysis

Energy dispersive X-ray spectroscopy (EDX) is a qualitative and quantitative X-ray analytical technique that allows for the identification of elements with atomic number $Z > 3$ as well as for elemental ratio quantification. EDX is considered as a non-destructive analytical technique, that is, the sample can be reanalyzed many times. However, very often materials can damage under the electron beam. Using this method, a quick overview of the elements present in the solid specimen can be obtained.[74] An electron beam is focused on the sample and the electrons from the primary beam penetrate the sample and interact with its atoms. The X-rays resulting from these interactions are further detected by an energy dispersive detector which displays a spectrum of intensity (number of X-rays) versus energy. The energies of the characteristic X-rays allow for the identification of the elements of the sample, while the intensities of the characteristic X-ray peaks allows for the quantification of the concentrations of the elements. However, to obtain the real concentrations, certain corrections to the raw intensities are needed.[73] The general approach for thin samples (*i.e.* absorption or fluorescence within the sample can be neglected) in TEM is the Cliff-Lorimer method. In this method, for a binary system (a substance composed of two elements A and B), characteristic X-ray intensities I_A and I_B are measured. Then, the concentration ratio of the two elements C_A/C_B is obtained from the equation $C_A/C_B = k_{AB} \cdot I_A/I_B$, where k is termed the Cliff-Lorimer factor (or k-factor) which is related only to the atomic-number for thin samples (the X-ray absorption and the fluorescence are minimal). The Cliff-Lorimer factor can be different in each TEM/EDX system and it depends also on the voltage being used. For ternary or higher order systems, the same equation applies

to each pair of elements (AB, BC, etc.) keeping in mind that the assumed elements must constitute 100% of the specimen ($C_A + C_B + ... + C_n = 100\%$).[68]

2.2.2. Scanning TEM (STEM)

To form scanning TEM (STEM) images, a fine probe is used. The scanning beam must always scan parallel to the optic axis. Here, two pairs of scan coils are used to achieve parallel incidence to pivot the beam about the front-focal plane of the upper objective polepiece. It is important to note that the quality of STEM images does depend on the probe which has aberrations due to the lens that was used to form it. In STEM, we do not use lenses to form the image. Therefore, aberrations present in the imaging lenses (*i.e.* chromatic aberration) have no influence on the image resolution.[68]

2.2.2.1. Bright-Field STEM Images

To form an image in STEM mode, we simply use the scan coils to scan the beam on the specimen. Due to the serial recording, image formation in STEM mode takes longer time than in TEM mode. In the TEM mode, we insert an aperture into the plane of the TEM diffraction pattern (*i.e.* objective aperture) and then only the direct beam, and not the other scattered electrons, are allowed to go through it into the imaging system. However, in STEM mode, instead of an aperture we use a bright-field (BF) detector which intercepts with the direct-beam electrons. Therefore, we allow only the electrons we want to hit the detector and contribute to the image formation. The signal is then generated at a point on the specimen.[68] This signal will be further amplified and it will be shown at an equivalent point on the computer display (Figure 2.6).

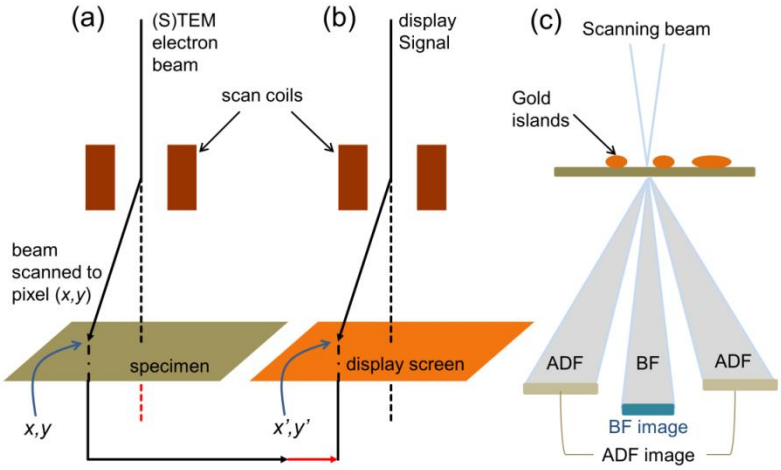

Figure 2.6. A schematic of formation of a scanning image (a) The beam-scan on the specimen is controlled by the scan coils in the microscope. (b) The scan coils control the beam-scan on the display screen of the STEM. (c) STEM image formation: A BF detector is placed in the microscope to intercept the direct beam. An ADF detector has a hole in the middle and is centered on the optical axis and surrounds the BF detector.[68]

2.2.2.2. Annular Dark-Field (ADF) STEM Images

For dark-field imaging, we usually use an annular detector, on which all the scattered electrons fall. As shown in Figure 2.7, the ADF detector has a hole in the middle and is centered on the optical axis, and therefore it is complementary to the BF image and collects low-angle elastically scattered electrons. This process is called annular dark-field (ADF) imaging, which has several advantages including less noise in the images, higher image contrast than the TEM dark-field (DF) contrast, and imaging of elements with low atomic number.[68]

2.2.2.3. High-Angle Annular Dark-Field (HAADF) STEM Images

We can also use another detector which surrounds the ADF detector which can pick the electrons which are scattered to higher angles forming a so-called high-angle (HA) ADF (or *Z*-contrast) image (HAADF). In ADF there is a problem of the contribution of the inelastically scattered electrons to the ADF signal. Since the normal ADF detectors collect Bragg-scattered electrons, it is necessary to have a detector with a higher angle to avoid the Bragg-scattered electrons to hit the detector. Thus, HAADF detectors are designed to collect scattered electrons through very high angles. A schematic of the HAADF detector setup along with BF and ADF detectors in a STEM is shown in Figure 2.7. HAADF images have the advantage of having its contrast unaffected by small specimen thickness changes.[68] The intensity of the HAADF signal is proportional to $Z^{1.7-2.0}$ where Z is the atomic number of the sample.[75]

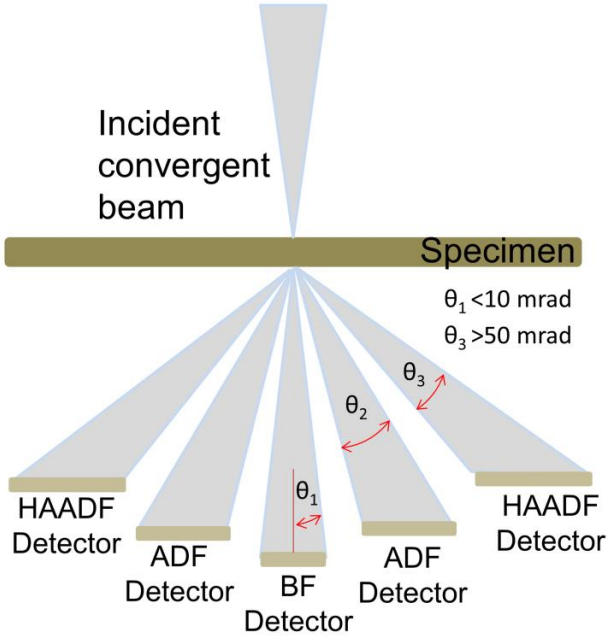

Figure 2.7. A schematic of the HAADF, ADF, and BF detector setup in STEM along with the range of electron scattering angles collected by each detector.[68]

2.2.3. TEM Specimen Preparation

The limits in the range of possible materials to be studied with TEM arise from the requirement for thin specimens containing no volatile components. On the other hand, sample preparation for TEM is a process that can cause modifications and alteration of the sample which needs to be taken into account. It is necessary to keep the specimen stable, thin, and small enough (about 3 millimeters in diameter) to allow its introduction into the evacuated electron column and also to permit the transmission of electrons. Each area of research and each material might require a different TEM sample preparation technique.[68,76]

To investigate biological samples in TEM, they can be deposited on copper grids covered with a thin film of *e.g.* amorphous carbon, silicon dioxide or silicon nitride.[33,77] When a droplet of the solution containing the biological sample is deposited on a grid, it is necessary that the sample is stained so that the biological entities can be easily contrast-differentiated from the background. The biological molecules are mainly consisting of carbon, oxygen, nitrogen, and hydrogen, which are not very dense, and the amount of electrons they absorb in the electron column is minimal compared to the intensity of the electron beam. Therefore, for normal electron microscopy, samples should be stained by using a heavy metal salt (usually uranium or tungsten) which can readily absorb electrons in the TEM.[78,79] Staining in this way (with heavy atoms) is called "negative staining" because the stain surrounds the biological particles but it is excluded from the volume occupied by those particles. As a consequence, a good contrast is achieved in TEM image when the stain completely surrounds the biological samples (the background is stained). Because, a higher electron scattering occurs by the heavy stain-rich regions compared to that light biological samples.[80]

There are different techniques to prepare TEM specimens such as ultramicrotomy, cleavage technique, chemical etching, tripod polishing, ion beam milling and focused ion beam (FIB). The two methods which were used to prepare TEM samples for the current thesis are the tripod polishing technique followed by the ion beam milling, and FIB.[81]

Ultramicrotomy

In this technique a diamond knife is used to cut out thin slices (< 100 nm) from a sample, which is mounted on an ultramicrotome holder, and to place the slices onto a supporting grid. If the sample is soft or small (*e.g.* bacteria or viruses), embedding in resin or in epoxy is necessary. This preparation technique is purely mechanical and therefore it could cause mechanical damage to the sample, however it does not cause any ion irradiation damage.[81]

Cleavage Technique

In this method, the material undergoes fracture or cleavage by applying a mechanical stress along weakly bonded atomic planes of the material. As a result, an electron transparent edge is obtained and the wedge is then mounted on a support grid for the TEM investigation. The cleavage technique is relatively a quick and inexpensive method to prepare TEM samples without the need of further thinning processes. However, it is limited only for hard materials such as glasses or silicon carbide.[81]

Chemical Etching

This method has been applied to a broad range of materials to avoid ion irradiation damage or high temperatures. In this method the sample thinning occurs as a result of chemical dissolution. Using appropriate solvent is an important factor in this method.[81]

Tripod Polishing and Ion Beam Milling

In this method, wedge-shaped specimens are prepared using a tripod polisher. Precut specimens are first mounted on a holder (typically Pyrex) and then polished on one side using a diamond-lapping film (DLF) on a rotating wheel to provide a planar surface. The granularity of the DLFs range from 30 to 0.1 µm. With using finer abrasive films, the rotation speed of the wheel is decreased to achieve a fine polished surface. Prior to polishing the other side, samples are removed from the Pyrex by dipping them into acetone. To polish the second side, specimens are turned around and glued again onto the specimen holder. A wedge angle is introduced and the specimens are thinned down to a specific thickness using different sets of DLFs. The specimens are polished down in several steps and between each polishing step the specimens are regularly monitored using an optical microscope. Thereafter, the samples are glued on a ring (*e.g.* molybdenum (Mo), cupper (Cu)). This method is widely used for prethinning before ion beam milling. Samples can be ion-beam thinned in an ion milling system using an ion gun. Here, mechanical prethinning of the sample is required before the ion milling process. Ion beam milling machines are one of the most commonly used machines in TEM sample preparation. This machine thins samples until they get transparent to the electron beam in TEM by bombarding the sample by energetic ions (typically argon (Ar^+)). The ion beam can be adjusted at angles typically from 1° to 10° and the guns can be set up for single or double-sector thinning. In new specimen stage designs, the specimen chamber can be cooled down to liquid nitrogen temperature. These options have made ion beam milling a versatile and effective method which allows for specific thinning of the sample considering the materials properties. For instance, adverse thinning effects on the multilayered structures can be minimized by using low milling angles (down to 1°). Besides, heating of sensitive biological samples under ion milling can be avoided by cooling down the specimen chamber.[81,82]

Focused Ion Beam (FIB)

One of the most common and widely used techniques for TEM sample preparation is the use of a focused ion beam (FIB) to mill and thin a section from the sample. This technique is especially of high importance for site-specific sample preparation. To this end, a FIB system which is usually linked to an SEM column (referred to as cross-beam) is used to prepare TEM specimens using an ion beam source (usually gallium (Ga^+)). To protect the sample surface during the specimen milling process and before cutting, the surface of the sample is covered with a thin protective layer (*e.g.* carbon or PtPd) deposited on the location of interest. Three FIB techniques to prepare TEM lamellas are trench technique, *in situ* lift-out method and *ex situ* lift-out method. In the trench method, a thin mechanically-polished sample is fastened to a support grid and is mounted vertically in the FIB to get two trench cuts from each side. Therefore, an electron-transparent slice remains, which is connected to the bulk material. In the *ex situ* lift-out method, a lamella from a site-specific region is ion milled to electron-transparency and then it is loose cut from the bottom by the ion beam and transferred to a TEM grid covered with a carbon film. In the *in situ* lift-out method, a thick lamella of the sample is cut and then lifted out using an *in situ* micromanipulator. Then the lamella gets fastened to a TEM support

grid using FIB metal deposition and it can be additionally thinned in the FIB. Lift-out methods are significantly faster than the trench method because no mechanical thinning is required.[81,82]

2.3. Atomic Force Microscopy

Atomic force microscopy is a method to investigate topographical features of a conducting or insulating sample by means of a vibrating tip, in which the force between the tip and sample is measured. Most modern AFMs use a laser beam deflection system. A schematic of atomic force microscope is shown in Figure 2.8.

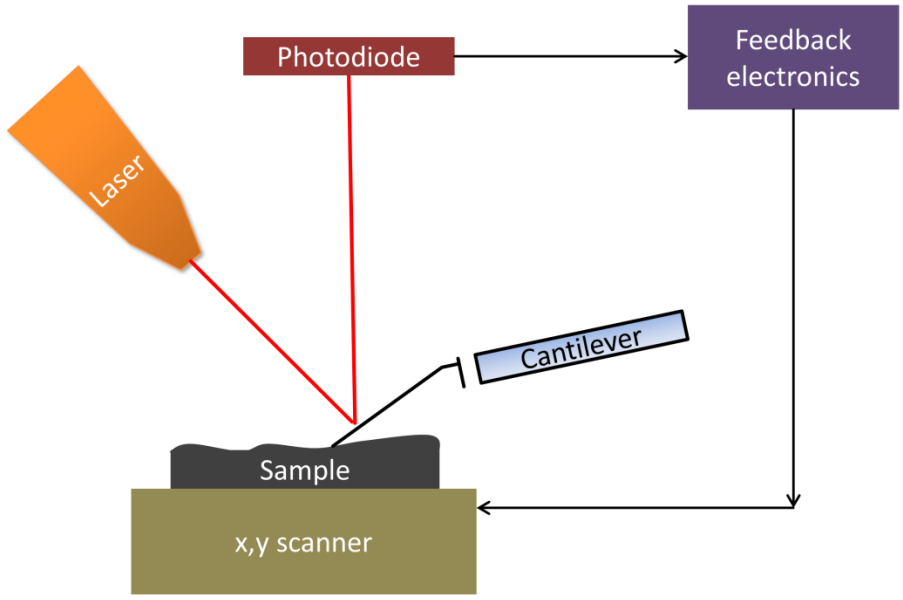

Figure 2.8. Schematic illustration of an atomic force microscope.[83]

In Figure 2.9, a diagram of the force between the tip and sample is illustrated. Three different regimes are shown in this diagram. First, if the tip is far away from the surface of the sample, there is almost no force acting between tip and sample. Second, for closer distances an attractive (negative) force between tip and sample appears. Lastly, for very small distances between the tip and the sample, a strong electrostatic repulsive force occurs. One problem here is that the probe can penetrate the sample, leading to elastic and further inelastic deformations. It should be noted that for one value of the measured force in the attractive regime, there are two tip-sample distances, point 1 and point 2 on the force distance diagram. The force between tip and sample can be measured using the deflection of the cantilever. The cantilever acts like a spring and the tip-sample force is proportional to the cantilever deflection. When the AFM tip is probing over the sample, a laser beam is reflected from the back of a reflective cantilever attached to the tip. This reflected light interacts with a position sensitive detector and delivers the frequency and the phase, the tip is vibrating at. The surface topography is then mapped while scanning over the sample by changing the z-position of the tip in such a way that the tip-sample force (correspondingly, the tip-sample distance) is kept constant. If the measurements are performed in the repulsive regime of the force-distance curve, the operating mode is called contact

mode. In this mode, the last atoms of the tip are in direct contact with the surface atoms.[83] AFM in contact mode is a non-destructive method which is capable of providing micro or nano-scale three-dimensional information on the surface of materials.

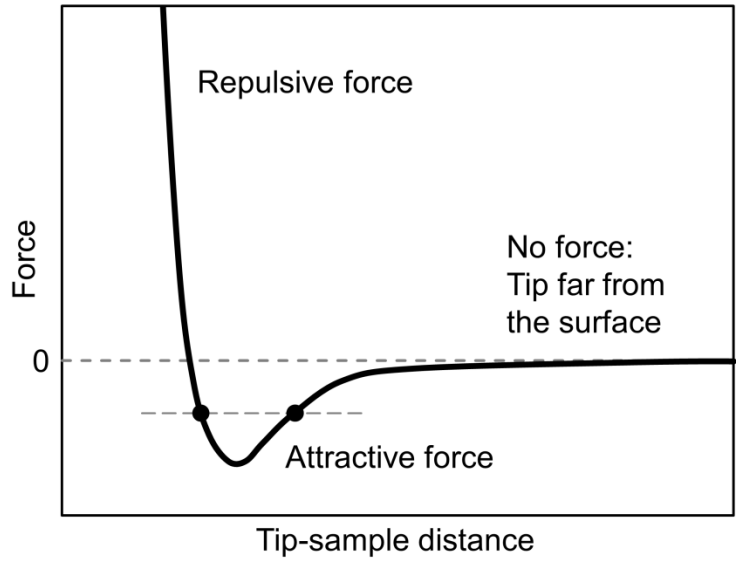

Figure 2.9. Qualitative behavior of the force (between the tip and the sample) versus the distance between the tip and the sample.[83]

By using AFM, the roughness of a surface can be measured. The root mean square (abbreviated to *RMS*) is the most commonly used quantity to measure the roughness of a surface and it is defined as the standard deviation of the heights $h(x, y)$

$$\sigma = \sqrt{\langle (h(x,y) - \bar{h})^2 \rangle} = \sqrt{\frac{\sum_{x=1}^{L} \sum_{y=1}^{W} (h(x,y) - \bar{h})^2}{LW}} \qquad 2.1$$

where L and W are the length and the width of the acquired image (*i.e.* number of pixels) and $\bar{h}$ is the average height. This calculation (Eq. 2.1) gives an accurate evaluation of the surface roughness over the imaged area.

2.4. Contact Angle Goniometry

Contact angle goniometry is a technique to determine the surface wettability and to investigate the hydrophobicity.[84,85] The term "wetting" describes the contact occurring between a liquid and a solid substrate when these two meet. The degree of wetting or the contact angle is the angle between the liquid–vapor interface and the solid–liquid surface which can provide information on the interaction energy between the liquid and the surface. The contact angle for flat surfaces is measured using a static sessile drop method, in which a drop of a liquid rests on the flat surface. The angle formed

between the liquid–solid and the liquid–vapor interface is then measured using an optical microscope. As shown in Figure 2.10, if the liquid has a strong attraction towards the solid surface (that is a hydrophilic surface), the liquid droplet will spread out on the surface and the contact angle will be low (close to zero). Whereas hydrophobic surfaces have a contact angle close or greater than 90°. Superhydrophobic surfaces are considered to have a contact angle greater than 150°.[84]

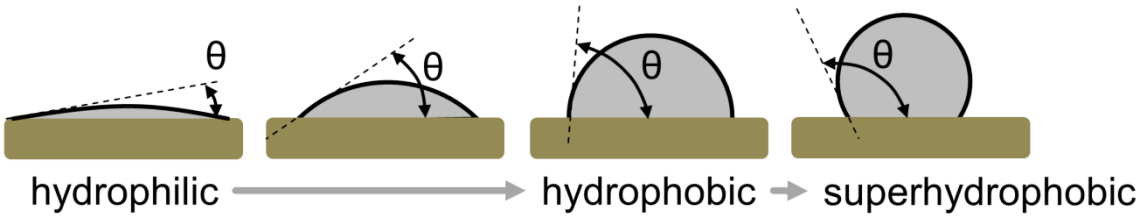

Figure 2.10. Schematic illustration of different contact angles and wettability of solid surfaces.[84]

2.5. Phage Propagation and Purification

M13KE (WT M13) phage was purchased from New England Biolabs, Inc. (Frankfurt, Germany). Competent cells of *E. coli* ER2738 were transfected with the replicative form (RF) DNA of M13KE. The transfected cells were shaken for 60 min at 37 ℃. After propagation, several dilutions of the transfected cells were made. 100 µl of the diluted cells were mixed with 300 µl of an overnight culture of *E. coli* ER2738 cells in 3-ml melted Luria Bertani (LB) top agar (47 ℃) and plated on LB agar plates with 40 µg/ml 5-bromo-4-chloro-3-indolyl β-D-galactopyranoside (X-gal) and 0.2 mM isopropyl β-D-thiogalactopyranoside (IPTG). After solidification of the top agar, agar plates were incubated at 37 °C overnight. To generate M13 phage, a single blue plaque was picked, and the phage was eluted in 500 µl of TE buffer (10 mM Tris/HCl, pH 8.0, 1 mM ethylenediaminetetraacetic acid) for 1 h. The obtained phage stock of M13KE was used for infection of a 400 ml culture of *E. coli* ER2738 cells at a density of 1×10^8 cells/ml. Adsorption of the phage was allowed for 15 min at room temperature without shaking. Subsequently, for propagation of the phage, the infected cells were grown at 37 ℃ in 2x yeast extract tryptone (2xYT)-medium overnight. The phage was harvested from the supernatant after removing the cells by centrifugation and precipitating the phage out of solution by adding 1/6 volume of 20% polyethylene glycol (PEG) 6000 and 2.5 M sodium chloride (NaCl). After centrifugation at 12,000 × g (gravitational force) at 4 ℃ for 20 min the phage pellet was suspended in 30 ml of Tris (hydroxymethyl)aminomethane (tris-buffered saline or TBS) (20 mM Tris/HCl, pH 7.4, 150 mM NaCl, 2.7 mM KCl) and reprecipitated with 1/6 volume of 20% PEG 6000/2.5 M NaCl. The pellet was suspended in 1 to 5 ml of the TBS buffer.

The phage titer was determined by spectrophotometry. The method is based on the relationship between the length of the viral DNA and the amount of the proteins, which, together, are the major contributors of the absorption spectrum in the UV range at 269 nm. The relationship between virion number and absorption was calculated by using the equation:[86]

$$virions/ml = (A_{269} - A_{320}) \times (6 \times 10^{16})/number\ of\ bases\ per\ virion \qquad 2.2$$

2.6. Convective Assembly Technique

Convective assembly (*i.e.* controlled drying) has been developed as an easily adopted and inexpensive tool for the deposition of the nanoparticles in ordered structures on a solid surface. This technique relies on the accumulation of particles near the three phase contact lines driven by solvent evaporation (shown schematically in Figure 2.11). In plate-withdrawal experiments, a glass plate is withdrawn with a constant speed with a trapped colloidal suspension to form ordered layers. The suspension along with the particles is moved along the contact line, driven both by the glass plate motion and the evaporative flux. The solvent evaporation leads to an increase of the concentration of the elongated particles in the solution at the contact lines with the solid surface (to compensate for the evaporated solvent) and causes the orientational ordering of the particles. When the meniscus thickness near the contact line becomes less than the particle diameter, an attraction occurs from very strong capillary interactions that lead to the formation of layers of particles.[87]

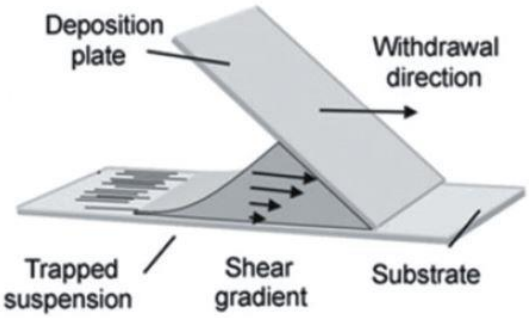

Figure 2.11. Schematic apparatus of convective nanoparticle assembly for controlled deposition. Reprinted by permission from Ref. [35], copyright 2012, from the Chemical Society of Japan and Wiley-VCH, Weimheim.

I used the convective assembly technique to assemble filamentous M13 phages in ordered structures on a solid surface. A convective assembly apparatus was designed and assembled in house as a part of the present thesis (see Figure 2.11). The apparatus is made up of a controlled linear motor (Pump 11, Harvard Apparatus, Holliston, MA, USA) and a glass slide with a 45° orientation with regard to the substrate holder plane. A viral solution is applied on the edge of the glass slide to form a thin strip of solution extended along the substrate. Viral particles are then directionally deposited by pulling the meniscus containing the virus solution with a constant rate. It should be mentioned that the angle between the glass slide and the substrate is believed to not have an influence on the assembly process. Because, the contact angle of the substrate remains constant regardless of a change in the glass-substrate subtending angle.

Figure 2.12. A Convective assembly apparatus designed and built up using a controlled linear motor (Pump 11, Harvard Apparatus, Holliston, MA, USA) and a oriented glass slide (45° with regard to the substrate plane). This apparatus was designed and assembled as a part of the current thesis. Photo Courtesy: Robin Lingstädt.

3. Chapter 3. Stability and Structural Integrity of M13 Phages

3.1. Abstract

M13 phages are being widely used in the novel virus-based technology (*i.e.* virotronics) and also as model systems to study liquid crystal textures due to their high aspect ratio and monodispersity.[24,41] Viruses normally suffer from chemical aggression rather than mechanical stresses.[88] Here I expose M13 filamentous phages to organic solvents and report their dissolution behavior and conformational changes using SEM and TEM. The aim is to find an appropriate organic solvent, in which the virions can retain their original structure and can maintain their directional assembly for longer periods of time. The effect of different types of organic solvents on the structural integrity of M13 phages has been directly visualized by SEM and TEM. The exposure of M13 phages to apolar hexane had no effect on the structure of the phages for up to 8 h. In contrast, phages showed ~8-fold contraction into rod-like I-forms and to flattened spheroids with ~12 nm diameter upon exposure to polar organic solvents. I show that this finding can be beneficial for the macromolecular self-assembly and in broader aspects, to enhance the spatial arrangement of desired inorganic nanoparticles in the rapidly developing field of virotronics.

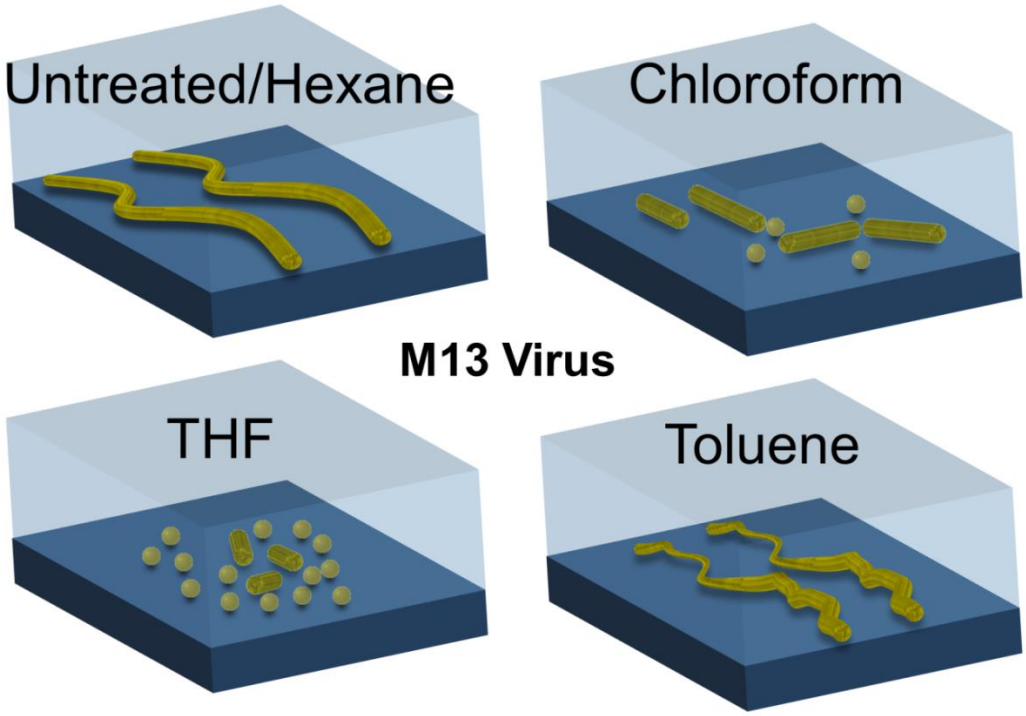

This chapter has been published in Ref. [89]

3.2. Introduction

Several studies have been devoted to stress the key role of organic solvents on protein folding and inactivation of viruses,[90,91] yet it has been shown that different kinds of filamentous viruses, even from the same class, show different structural integrity in an organic solvent.[92] For instance, the filamentous phage Pf1 was inactivated in diethyl ether and acetone, whereas the filamentous phage fd retained its native structure in these solvents.[93] M13 phages are among the phages being successfully used in templating inorganic nanoparticles and hence in the development of optical biosensors and battery devices.[52,94,95] The major coat protein (pVIII) is comprised of 50 amino acid residues with a highly hydrophobic core that accounts for the interlock of the coat protein with its subunits. [15,22] It has been reported that these hydrophobic interactions have a strong role in the stabilization of virions against denaturation.[93]

M13 filaments are highly sensitive to ultrasonication[15] and their worm-like shape would change to a mucus-like structure under near-infrared laser irradiations.[96] The denaturation process in solutions has been examined and observed in aqueous-organic mixtures. But viruses might experience a higher degree of denaturation in pure organic solvents. Solvent properties such as hydrophobicity and hydrogen-bonding capacity have a high impact on the structural integrity of proteins and virus particles.[24,90] It has been reported that M13 phages are very stable viral particles that can resist heating and cooling processes between 90 °C and −20 °C and can resist high and low pH values without losing their structural integrity.[15,20,23,78] For many applications in virotronics, viruses must be stable for a certain period of time under a wide range of conditions – in particular, in different organic solvents. These solvents are often used in the production of organic electronic devices that are fabricated by solution processing (*e.g.* organic light-emitting diodes).[97] While a number of studies have been devoted to the structural stability of fd,[98] f1[93] and T7[88] phages in organic solvents, no work has been performed yet to systematically study the structural integrity of M13 phages in different organic solvents. Establishing conditions under which M13 phages are stable is an important determinant in the practical utility of the virus technology.[24]

3.3. Materials and Methods

The WT M13 phages were suspended in TBS at pH 7.4. An aliquot of phage solution (5 µl) with a concentration of 1.4×10^{12} pfu/ml was added to an equal volume of an organic solvent (hexane (Sigma-Aldrich), chloroform (Merck), tetrahydrofuran (THF, Merck) and toluene (Sigma-Aldrich)) at room temperature. The mixture was left unstirred for 60 min. Thereafter, a 5 µl droplet of the mixture was loaded for 5 min onto Quantifoil® (Quantifoil Micro Tools GmbH) TEM grids covered by a carbon support film. The samples were gently washed with Milli-Q water, negatively stained with 1% uranyl acetate (UA) and blotted dry. The Zeiss SESAM microscope was used to carry out TEM investigations. The average viral particle sizes were calculated by averaging sizes over all the particles of the same type on the acquired BF-TEM images. The SEM images were acquired by the Zeiss DSM 982 Gemini operating at 3 kV. To assemble a homogeneous and closely-packed viral film on silicon wafers, the viral particles were directionally deposited using the convective assembly technique by pulling a meniscus containing 5.5 µl of the virus solution across the substrate at a constant rate (1.2 mm/min).

3.4. Results and Discussion

Untreated phages were included in this study as a control sample (Figure 3.1a,b). BF-TEM observations of hexane-treated M13 phages revealed that the virions retained their structure, flexibility and original dimensions (see Figure 3.1c,d). Phages showed no decomposition or fragmentation after 1h contact with hexane. This could be associated with the fact that hexane is a nonpolar hydrophobic solvent that cannot compete for hydrogen bonds between proteins and thus was not able to denature the native structure of the phages. However, when exposed to chloroform, phages were destabilized from their native structure and they were ~5-fold contracted into shortened I-form rods having an average length of ~180 nm (blue arrows in Figure 3.1e). A rather low portion of spherical filaments (spheroids or S-forms) having an average diameter of ~17 nm were also present (red arrows in Figure 3.1f). Both morphological changes have been reported to result in the inactivation (*i.e.* loss of infectivity) of phages.[93,98,99,100] The reason for these observations relies on the fact that chloroform is a polar solvent and is therefore able to break the hydrogen bonding and the hydrophobic interactions between the capsid proteins.[99]

Similarly, BF-TEM images of THF-treated phages showed apparent fragmentation of the phages but in a greater extend (red and blue arrows in Figure 3.1g,h). The original filaments were extremely decomposed mostly into S-forms and in a less amount in I-forms. This could be a result of peptide bonds breaking in capsid proteins and by having the coat proteins detached from the core DNA which had been held together by weak electrostatic interactions.[99] The diameter of rods and spheroids were in average ~120 nm and ~13 nm, respectively, which shows more filament contraction (~8-fold contraction) and decomposition rate compared to the chloroform-treated filaments. THF is one of the most polar ethers and has a similar polarity as chloroform. However, THF is hydrophilic and water-miscible and therefore it is able to dissolve in the phage solution and rapidly break the hydrogen bonds in proteins and consequently changes the structure. In contrast, chloroform is hydrophobic and does not have as much interaction with the phages as THF. This could be the reason that in our specific experimental time period, phages showed a higher degree of decomposition in THF compared with that in chloroform. It should be noted that this phenomenon is a function of exposure time, indicating that phages would suffer the same level of decomposition in THF after a certain amount of time as they did in chloroform. In contrast to chloroform and THF, toluene has a relatively low polarity and therefore did not show high fragmentation of M13 filaments, yet it was able to deform the phages to a certain level. As shown in Figure 3.1i,j, no I-form or S-form particles could be observed, however virions were kinked that could be attributed to the disruption of the molecular tertiary structure interactions and deformation of the capsid arrangement.[90] Hence, the solvent polarity has a significant contribution to the interactions that lead to the structural changes of M13 phages. Higher polarities of the solvents employed in this study have a higher influence on breaking inter-coat protein forces, and weakening the van der Waals interactions between the DNA and the coat proteins.

Next, I assembled a well-aligned film of phages on a silicon wafer (Figure 3.1k) and immersed it for 8 h in 3 ml of hexane. As shown in Figure 3.1l, the hexane immersion did not disrupt the phage assembly even up to 8 h, showing that extended exposures to hexane has no influence not only on the structural integrity of virions, but also on the their directional assembly. The alignment of the phage assemblies can be identified by Fourier transform (FT) images. The insets in Figure 3.1k,l show the FT images with an intensity pattern in a narrow and elongated ellipse perpendicular to the direction of alignment, that confirms the highly-aligned structure of the phage assemblies.

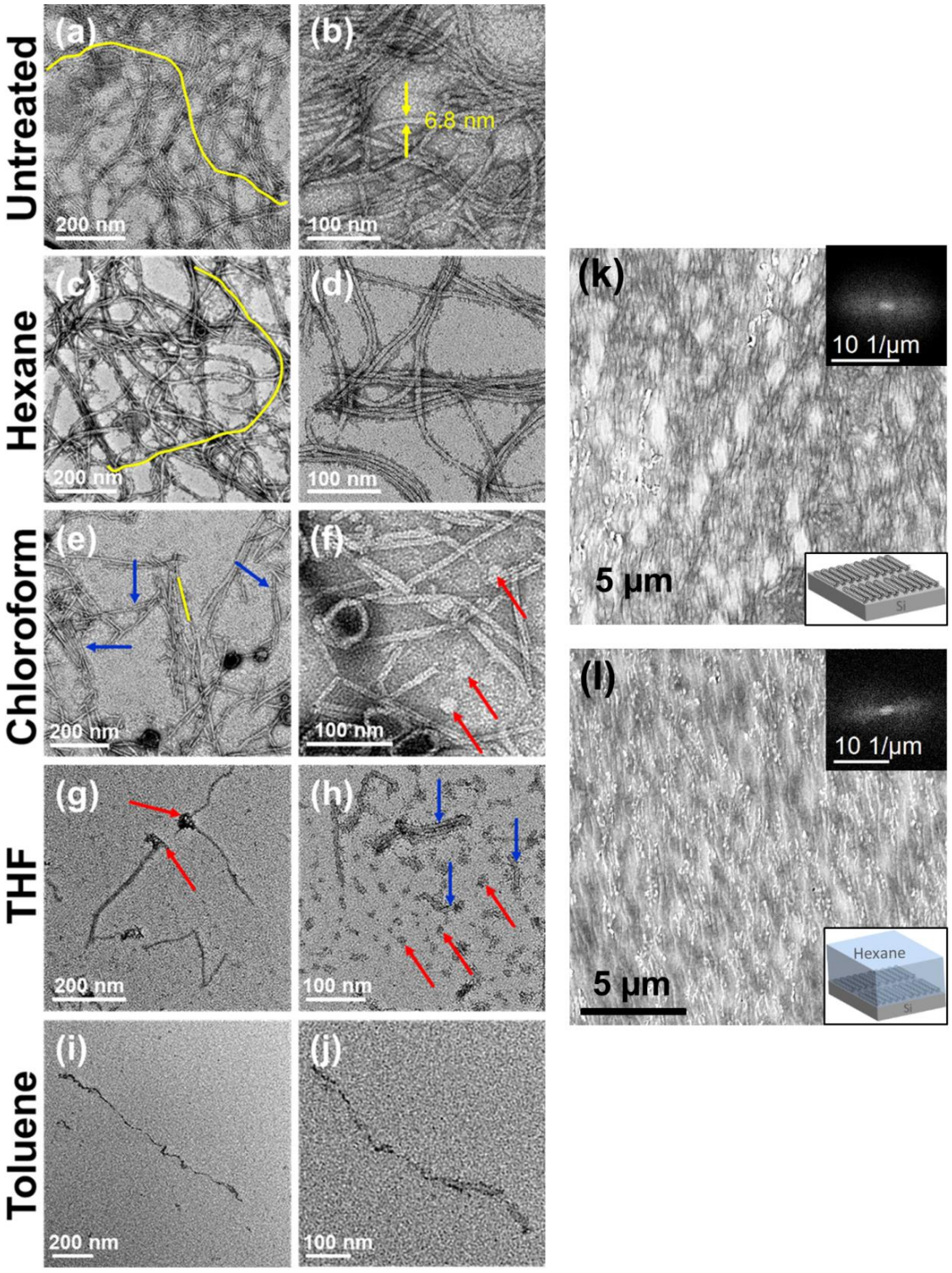

Figure 3.1. BF-TEM images of untreated M13 phages (a,b) and the conformational and structural changes of phages after 1 h exposure to (c,d) hexane, (e,f) chloroform, (g,h) THF and (i,j) toluene. The right column shows high-magnification BF-TEM images. Yellow lines mark an intact phage in (a,b) and a single shortened I-form rod in (e) as a means of identification. Blue and red arrows show the contraction of M13 intact filaments to I-forms (shortened rods) and spheroids, respectively. SEM image of a densely-packed and well-aligned assembly of phages on (k) silicon substrate and (l) after exposure of the assembly to hexane for 8 h. The small white round particles on the top of the phage layers are composed of sodium (Na) and chlorine (Cl) (as measured by EDX) which arise from the salts present in the primary phage solution. The insets show the FT images of the corresponding SEM images. Adapted with permission from Ref. [89]. Copyright 2016 Journal of Biomaterials and Nanobiotechnology.

This key finding is of high importance in virotronics, in which viruses are used as unique biological entities to create advanced multi-component materials with a high molecular-level control.[2] The functional properties of such devices, *e.g.* electrical[35,101] and magnetic collective properties[102] can be maximized by using a self-assembled layer of organic molecules to spatially arrange inorganic nanostructures.[44] However, inorganic nanoparticles usually come in contact with organic templates in the presence of an organic solvent. Therefore, hexane can be a great candidate for a dispersion medium for the desired inorganic particles prior to them assembling into functional 2D films.

3.5. Conclusions

In closing, this study provides direct assessment of the stability of the filamentous M13 structure when exposed to different organic solvents. Efforts to maintain the structural integrity of viruses leads to an increased understanding of the factors that disrupt their structure. Phages showed to be denatured in polar organic solvents as compared to nonpolar solvents. This phenomenon could be understood by considering three factors: Solvent hydrogen-binding capacity, hydrophobicity and water miscibility. This work also gives information on the handling of supramolecular assemblies in organic solvents for virus-based materials. This can be used in the developing topic of research that is the control of macromolecular assemblies with hierarchical frameworks.

Contributions to this chapter:

Pouya Moghimian and Benoit P. Pichon (Université de Strasbourg) designed the study. Pouya Moghimian performed research. Sandra J. Facey (University of Stuttgart) prepared the phage solutions. Christine Mollenhauer (MPI-IS) provided the organic solvents. Vesna Srot (MPI-FKF) and Peter A. van Aken (MPI-FKF) jointly supervised this work. The published article (Ref. 89) was written by Pouya Moghimian.

4. Chapter 4. Adsorption and Self-Assembly of M13 Phages on Solid Surfaces

4.1. Abstract

Fabrication of multi-component materials with complex structures is of high interest due to their broad range of applications.[47] Biologically-inspired processes in which the biological entities (*e.g.* phages) serve as templates for the directed synthesis of a range of complex inorganic nanostructured materials have allowed us to envision efficient electronic devices.[47,53,103] Here, a versatile method for the directional assembly of M13 phage using amorphous carbon (a-C) and SiO_2 thin films over micrometer scale was demonstrated. A high affinity of the M13 phage macromolecules for incorporation into aligned structures on an amorphous carbon surface was observed at the concentration range, in which the viral nanofibers tend to disorder. In contrast, the viral particles showed less tendency to adopt an aligned orientation on SiO_2 films when deposited in close vicinity. Here an interpretation of the role of the carbon surface in significant enhancement of adsorption and generation of viral arrays with a high orientational order was proposed in terms of surface chemistry and competitive electrostatic interactions. Our aim is to investigate the surface role on the immobilization process in a highly ordered manner and to attain a fully covered surface with densely packed and highly oriented M13 phage viral particles. This study suggests the use of amorphous carbon substrates as a template for directional organization of a closely-packed and two-dimensional M13 viral film, which can be a promising route to mineralize a variety of inorganic materials.

Table of contents: Self-assembly of M13 phages on flat (*i.e.* unstructured) solid surfaces.

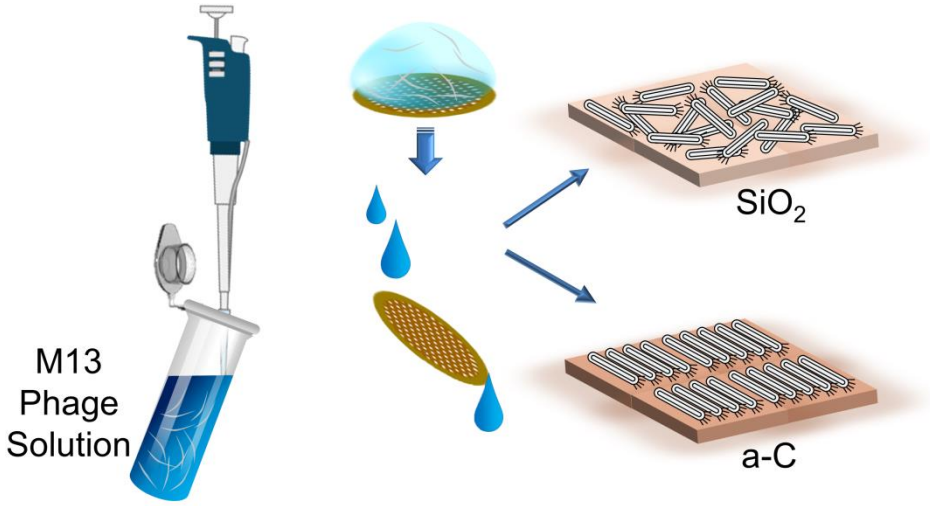

This chapter has been published in Ref. [40]

4.2. Introduction

In order to induce the growth of uniform and homogeneous inorganic nanostructures, bio-assisted synthesis methods are utilized as promising tools to attain organic–inorganic hierarchical nanolayers. To this end, not only preparation of a densely packed layer of biological entities onto specific surfaces is inevitable, but also achieving a directionally ordered pattern of the biological entities, extending over a length scale is crucial to enhance the functional and physical properties of the final product.[35,41,43,101] The WT M13 phage has been the focus of many studies among the phages due to its ability to template the formation of exquisite nanoinorganic material structures at room temperature.[6] Several approaches have been undertaken to form well-ordered M13 viral structures.[104] As an example, Sawada *et al.* [31] have immobilized engineered M13 phages in an oriented manner onto an poly(methyl methacrylate) (PMMA) film by dipping method. It has been stated that a higher sweeping-up speed leads to a more ordered structure due to the higher capillary force acting at the meniscus. Although several assembly attempts have been made for hybrid structures using modified M13 phage recently, the study of the surface chemical key factors in directing the 2D order of WT M13 viral particles has been overlooked.[41,105] Wang *et al.*[106] successfully assembled M13 phage bundles on a poly(L-lysine) substrate. The alignment of M13 phages leads to well-ordered nanofibers, which is of technological importance in piezoelectric generators.[101] The piezoelectric strength of directionally patterned phages was reported to intensify due to the dipole moment of the pVIII α-helical structure.[35,101] In general, the orientation of M13 viruses onto a substrate depends on phage concentration, biomolecular interactions between the virion particles and external fields.[17,38,107] However, not only the surface chemistry of the substrate but also other factors like the surface roughness play prominent roles in protein adsorption and directional alignment.[108,109] The influence of different surface chemistries on the adsorption of M13 phages and their further alignment was less studied up to now.

4.3. Materials and Methods

WT M13 phages were pipetted from viral solutions with different concentrations onto TEM grids (~3 mm) covered by a carbon support film or a thermally grown silicon dioxide membrane, both with a thickness of ~20 nm. Thereafter, the grids were directionally washed using Milli-Q water in order to apply a shear force[110] on the phage particles in a directed manner and to remove soluble salts from the supporting films. Lastly, the specimens were negatively stained using 2% uranium acetate (UA) and characterized by TEM. The Zeiss SESAM microscope was used to carry out TEM investigations. In addition, STEM and EDX analysis were performed using the VG HB501UX STEM instrument. Furthermore, the surface roughness of the films was measured by means of AFM NanoWizard II. The contact angles of the SiO_2 and a-C films were measured using the Krüss G10 contact angle goniometer. The measured contact angles were an average on three different regions of each surface.

The concentration of phage solution was calculated by using the molecular weight of a phage particle (12×10^6 Da).[111] The initial phage concentrations and the corresponding liquid crystalline regions are shown in Table 4.1.

Table 4.1. Phage concentrations used for macromolecular self-assembly on a-C and SiO_2 thin films, estimated from the molecular weight of phage particles. Reprinted with permission from Ref. 39. Copyright 2014 American Chemical Society.

Self-assembled structure	Initial concentration (pfu/mL)	Initial concentration (mg/mL)
Isotropic region[a]	1.4×10^{13}	0.28
Nematic region[b]	3.5×10^{14}	6.97

[a] Concentrations below 5 mg/ml.[2]
[b] Concentrations above 5 mg/ml.

4.4. Results and Discussion

In order to substantiate the role of the surface on the protein adsorption, the phage self-assembly was studied in two liquid crystalline regions: in the extreme isotropic region and above the nematic threshold. Initial investigation revealed that the low concentration of M13 phage solution (1.4×10^{13} pfu/ml) leads to the disordered phase of viral particles on the silicon dioxide surface (Figure 4.1a,b). From this observation, it can be concluded that when the concentration of the primary viral solution is below 5 mg/ml (2.51×10^{14} pfu/ml) (see Table 4.1) the trend of the system is towards the formation of an isotropic phage distribution, which exhibits no orientational order.[2,112] Phage bundles were generated, which resulted in a decrease in the apparent concentration of filamentous particles. It has been reported that phage bundling can disrupt the long-range phage orientation in the nematic regime.[106] Even though from Figure 4.1a,b the state of disorder was evident at the microscopic level, a more accurate description and identification of the macromolecular arrangement of the prepared viral films can be obtained by FT images. The insets in Figure 4.1a,b show the FT images for disordered nanofibrous viruses, which show no preferential order and a round intensity profile. It should be noted that the partial darkening effects of WT phages arise from the heavy metals in the UA solution used as the staining agent. Figure 4.1c and d show BF-TEM images of WT M13 phages deposited on an a-C film from a viral solution with the same concentration of 1.4×10^{13} pfu/ml. The FT images for aligned viruses produce an intensity profile distributed in a broad elongated ellipse perpendicular to the virus alignment. The a-C support film was covered with a packed layer of phages, suggesting a 2D stacking upon the drying process on the carbon film. As seen in Figure 4.1d, single phages could be traced on the top of the phage layer, which might be due to the electrostatic interaction between the phage particles and the rather weak driving force for all the filamentous particles to point along the same direction for low colloidal concentrations. The nanofibers are not perfectly aligned, yet they do have some degree of alignment as confirmed by the FT images.

Next, the viral solution of a different phage concentration was deposited onto the a-C and SiO_2 films. This was done to direct the liquid crystalline system to a phase transition from an isotropic to a nematic phase on the supporting films. For this purpose, the phage concentration was increased to a concentration above the nematic threshold (see Table 4.1).

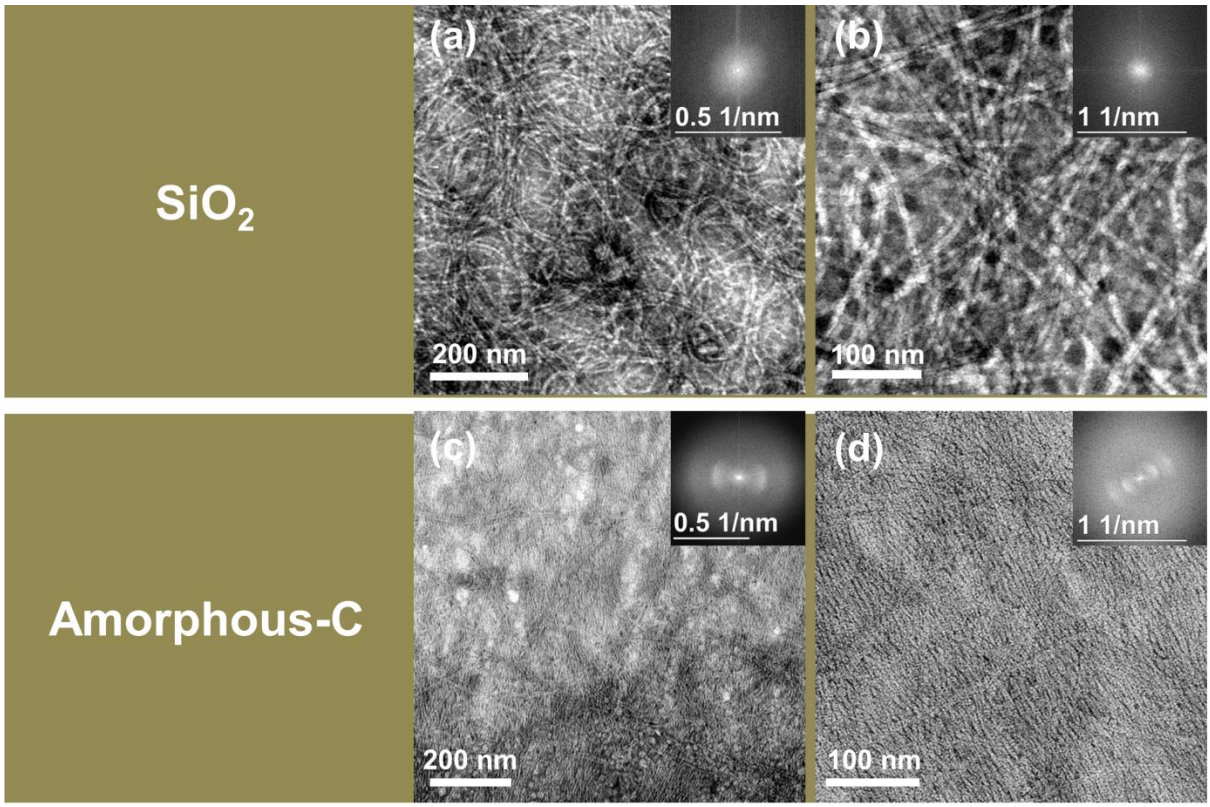

Figure 4.1. (a) BF-TEM image of randomly distributed and bundled WT M13 phages immobilized on SiO_2 membrane from a droplet of M13 viral solution (1.4×10^{13} pfu/ml). (b) High-magnification image of (a), depicting a highly disorder and web-like structure. (c) BF-TEM image of WT M13 phages packed on a-C support film from a droplet of M13 viral solution (1.4×10^{13} pfu/ml). (d) High-magnification image of (c), showing the 2D alignment along a common direction. The insets show the FT images of the corresponding BF-TEM images. The isotropic–nematic transition is visible from (b) to (d). Reprinted with permission from Ref. [40]. Copyright 2014 American Chemical Society.

Figure 4.2a,b and Figure 4.2c,d show BF-TEM images of WT M13 phages deposited on a-C and SiO_2 films respectively from a viral solution with the same concentration of 3.5×10^{14} pfu/ml. It could be observed that a high directional phage alignment of the viral 2D film could be achieved on the a-C film (cf. Figure 4.2a,b with Figure 4.2c,d). A closely packed and highly aligned M13 phage viral film along a direction was obtained at the initial phage concentration of 3.5×10^{14} pfu/ml. This was verified by the FT images showing a narrow and elongated ellipse perpendicular to the direction of alignment (see insets in Figure 4.2c,d). This suggests the formation of a well-organized and uniform viral film on the a-C surface. As shown in Figure 4.2b, an intertwined texture having a net degree of alignment was detected on the SiO_2 surface.

Small round-shaped particles, which were not dissolved in Milli-Q water during the washing process, were also observed on surfaces. The presence of these particles, which might have emerged from the viral solution, is due to buffer and salts remaining in the purified M13 phage solution and/or the buffer used to disperse the viral particles in the aqueous medium.[31,113]. It could be hypothesized that upon stacking of the very thin 2D nematic layer on the a-C surface, the small solution residues have formed local agglomerates atop the phage layer, which could be prone to removal during the washing process.

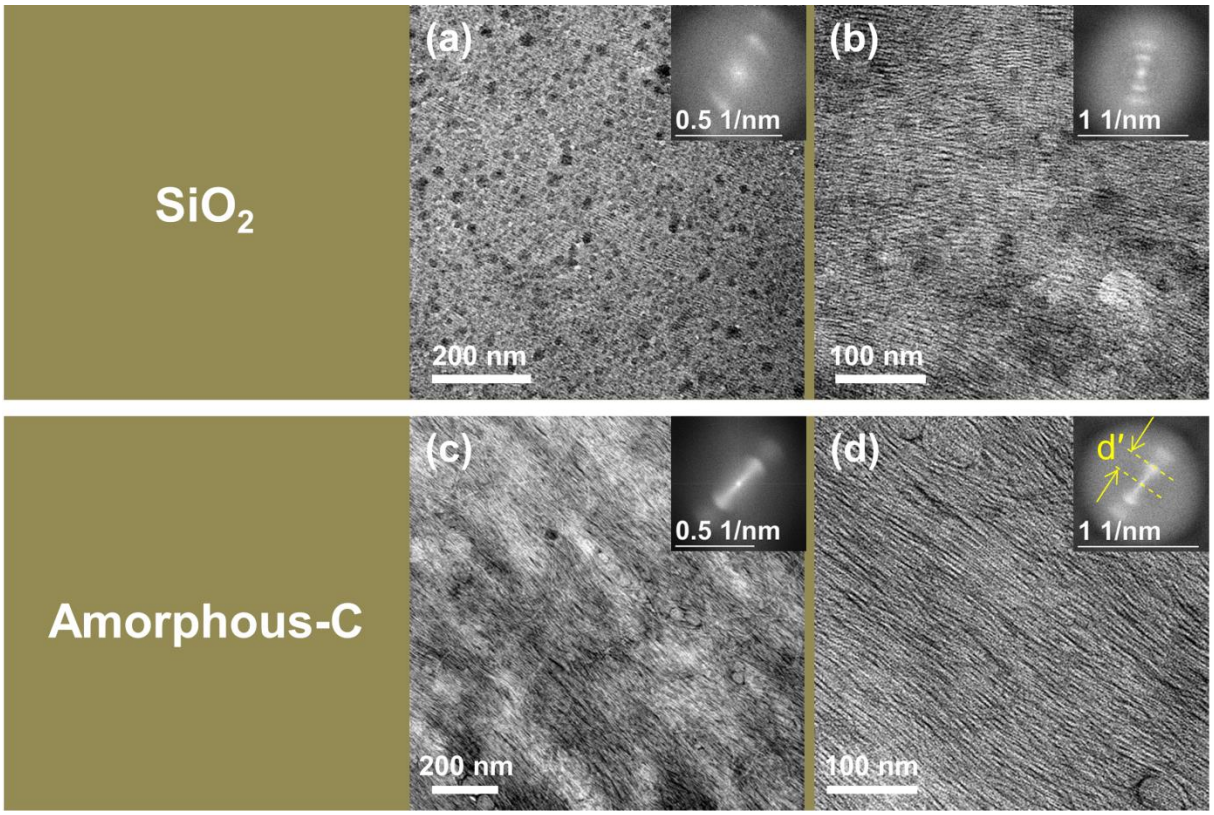

Figure 4.2. (a) BF-TEM image of WT M13 phages oriented on SiO_2 membrane from a droplet of M13 viral solution (3.5×10^{14} pfu/ml). (b) High-magnification image of (a), showing slightly intertwined and branched WT M13 nanofibers. (c) BF-TEM image of WT M13 phages densely packed and highly oriented on a-C support film from a droplet of M13 viral solution (3.5×10^{14} pfu/ml). (d) High-magnification image of (c), showing a high degree of anisotropy. The insets show the FT images of the corresponding BF-TEM images. The measured spacing $d' = 0.15$ 1/nm (in reciprocal space) gives an average width of 6.7 nm. This width is approximately equal to the thickness of the M13 phage particles. Reprinted with permission from Ref. [40]. Copyright 2014 American Chemical Society.

From these results, it can be inferred that the a-C surface induces the assembly of M13 phages into parallel arrays, regardless of the initial low concentration of the viral solution. The a-C surface can stimulate the M13 phage macromolecules to form aligned structures in the concentration range in which the viral nanofibers tend to disorder (see Figure 4.1d). The SiO_2 has a smooth and hydrophilic (with native oxide and contact angle ~55°) surface, whereas the a-C film could be described as neutral and slightly hydrophobic (contact angle ~70°) and has a roughness of nearly 3 times that of SiO_2 (see Figure 4.3).[33,114,115]

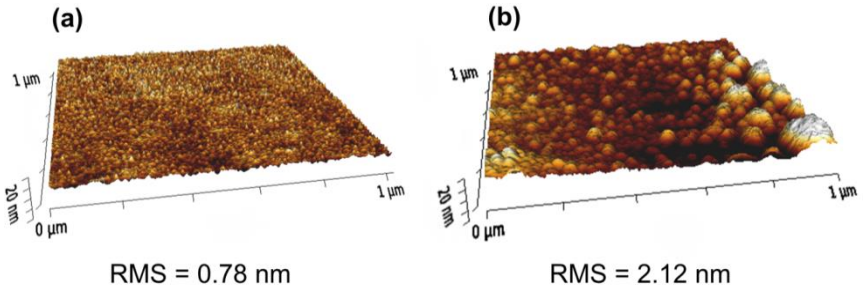

Figure 4.3. AFM 3D images of surface morphologies and RMS values of surface roughness of (a) SiO_2 and (b) a-C thin films, all with a scan size of 1×1 µm^2. The z-scale is 20 nm per division for all images. Reprinted with permission from Ref. [40]. Copyright 2014 American Chemical Society.

It has been reported that the state of hydrophobicity and the charge density can influence the protein adsorption.[116] For instance, it has been stated that the hydroxyl (OH^-) groups of the SiO_2 surface can function as adsorptive sites for positively-charged organic materials.[117,118] In contrast to the SiO_2 surface, the hydrophobic nature of a-C causes weak interactions between the viral macromolecules and the solid surface. This is believed to allow for the mobility of phages after deposition and further directional stacking of the 2D viral film as a consequence. The estimated two-dimensional phage number densities of the viral films on the a-C and SiO_2 substrates were calculated according to:

$$\rho^{(2D,est)}L^2 = L/P, \qquad 4.1$$

where L is the length of the thin rods and P is the center-to-center distance of two hypothetical parallel cylinders of diameter $D \leq P$. The particle number densities of thin rods in two dimensions were estimated from the intensity profiles of Figures 4.1d, 4.2b, and 4.2d to be 101.6, 125.7, and 130.6, respectively. These values are considerably higher than the particle number density of thin hard rods in two dimensions at the isotropic to nematic phase transition according to the Onsager model:[119]

$$\rho^{(2D,IN)}L^2 = 4.7. \qquad 4.2$$

Hence, the $\rho^{(2D,est)}$ values are significantly higher than the $\rho^{(2D,IN)}$ due to the incubation of viral solution on the thin films. Therefore, a two-dimensional nematic phase can be found in the aforementioned Figures (Figures 4.1d, 4.2b, and 4.2d) similar to earlier result for amyloid fibrils of comparable diameter.[120]

It has been demonstrated that a smooth surface hosts lower amounts of adsorbed proteins per macroscopic area compared with a rough surface.[114] It should be noted that a solid surface which has a higher isoelectric point (pI) is a higher virus absorbent compared to those with a lower pI under the same experimental conditions.[116] The pI values of the a-C and SiO_2 solids have been measured to be 7–9 and 1.9, respectively.[33,121] As pointed out, hydroxyl groups present on the SiO_2 surface[115,122] might influence the adsorption of organic residues from the viral solution.[123] In an aqueous medium, the phage coat proteins tend to fold in a way to expose their hydrophilic side chains on the surface while shielding hydrophobic side chains. **[116]** Thus, on SiO_2 films, M13 phages prefer to paste their bodies on the surface firmly and this prevents the freedom of the viral particles to orient in a parallel fashion when deposited in close vicinity. This is suggested to be the reason for the formation of slightly branched arrays of phage fibers even at high concentrations of phage solutions (see Figure 4.2b). Furthermore, as shown in Figure 4.1a,b, at low virus concentrations the bundle formation and immobilization of phages upon the deposition process prevent their further alignment on the solid film. Therefore, there is not enough driving force to dictate the self-assembly of the phages along a direction even as a result of directional flow of Milli-Q water. Interestingly, the phage particles have the ability to accumulate and orient themselves on the a-C thin film to some extent (see Figure 4.2c,d), which could be merely attributed to the specific surface chemistry of a-C. The a-C thin films have been shown to adsorb a substantially higher amount of human serum albumin, human blood plasma, and antibodies compared to silicon.[114] M13 phage is composed of amino acid residues with side chains on its coat proteins. Contact sites between these amino acids and the surface allow for the adsorption of proteins on the surface.[124] On a-C films, a clear preference for the contact sites to align themselves according to a common direction was observed. Although the complex correlation between the surface hydrophobicity, roughness, interparticle forces, and external shear forces in nanoparticle assembly needs further investigation, our hypothesis is that the high contact angle of the a-C surface and its high

isoelectric point are the keys for obtaining a high degree of phage alignment and different adsorption responses at a specific phage concentration.

4.5. Conclusions

These results suggest a versatile approach that can be used to influence the mineralization of a variety of inorganic nanostructure layers and therefore open up exciting opportunities for the fabrication of organic–inorganic systems with nanoscale precision. This work demonstrated that, under specific experimental conditions, amorphous carbon film is a promising host for a highly oriented layer of M13 phages compared with silicon dioxide. The M13 phage particles were found to have a high affinity for incorporation into a densely assembled pattern on a-C films. Such assemblies were obtained by applying phage solution on the surface without employing nanoparticle assembly methods such as dip coating or convective assembly. Obtaining a directionally organized monolayer of M13 phages is a challenge due to their extremely low thickness, flexibility, and high affinity for bundle formation. Thus, this work sets the stage for a novel paradigm for biomolecular two dimensional self-assembly. This has potential in the development of nanoscale scaffolds for bottom-up construction of multicomponent devices. Future work will be performed to utilize the a-C-induced M13 phage film with closely packed and oriented fashion to further fabricate multilayers of organic–inorganic materials, which contain alternating virus-templated layers.

Contributions to this chapter:

Pouya Moghimian, Vesna Srot (MPI-FKF) and Dirk Rothenstein (University of Stuttgart) designed the study. Pouya Moghimian performed the research. Sandra J. Facey (University of Stuttgart) prepared the phage solutions. Ludger Harnau (MPI-IS) calculated the 2D phage number densities. Markus Weiler (MPI-IS) did the AFM work. Stefan Kilper (MPI-IS) measured the contact angles. Bernhard Hauer (University of Stuttgart), Joachim Bill (University of Stuttgart) and Peter A. van Aken (MPI-FKF) jointly supervised this work. The published article (Ref. 40) was written by Pouya Moghimian.

5. Chapter 5. Ordering of Biomolecular Rods on Complex Geometries

5.1. Abstract

Properties of colloidal particles in contact with structured substrates are of high interest due to useful applications such as selective deposition of particles.[125,126] In the previous chapter, the self-assembly of M13 phages on unstructured surfaces was investigated. In the current chapter, I report on the evaporative self-assembly and orientational ordering of semi-flexible spherocylindrical M13 phages on asymmetric stranded webs of thin amorphous carbon films. Although the phages were dispersed with a low concentration in the isotropic phase, the substrate edges induced nematic ordering and bending of the phages. As revealed by TEM, phages were aligned parallel to the curved substrate edges. This two-dimensional self-assembly on structured substrates opens a new route towards designed structures of orientationally ordered semi-flexible biomacromolecules. The aim is to study the possibility to control the orientation of M13 phages in two-dimensional nematic films by choosing structured substrates. The electron transparent a-C thin film was used to provide random and non-symmetric confining geometries with variable strand widths of the web film and also to obtain a high adsorption of viral particles on the substrate. [40] Here I shift the focus from evaporative self-organization on rationally designed surfaces to that on a complex amorphous carbon surface.

Table of contents: Orientational ordering of M13 phages on structured solid surfaces.

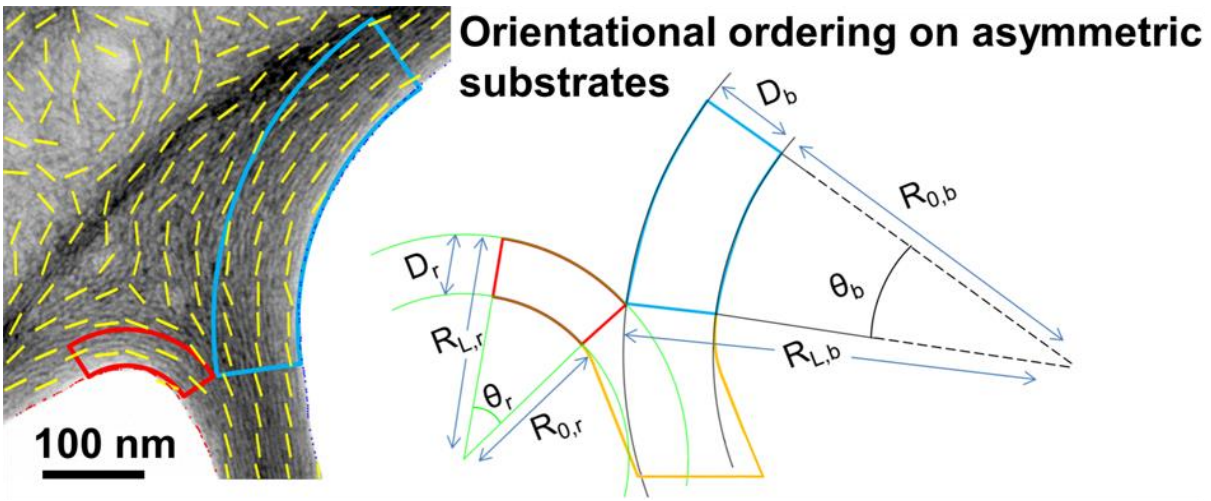

This chapter has been published in Ref. [12]

5.2. Introduction

While various experimental studies,[125,126,127,128] theoretical investigations,[129,130] and computer simulations [131,132] have been devoted to the understanding of the behavior of spherical colloidal particles on structured substrates, only few studies have been aimed at the properties of rod-like or worm-like particles in contact with such substrates, despite the importance of elongated particles for both biological and materials applications.[51,133,134,135,136,137,138] For instance, DNA separation studies have been performed using a channel device that uses entropic trapping of DNA molecules.[139,140,141] The entropic traps use substrates exhibiting a pattern consisting of rectangular blocks as a molecular sieve. Also, the influence of geometrical surface patterns on the frictional properties of nanowire-based lubrication systems has been investigated.[142] It has been demonstrated that nanowires can act as effective lubricants on structured substrates. Recently, Dammone *et al.*[143] studied the splay-to-blend transition of fluorescently labelled fd viruses confined to channels with wedge-structured walls having different wedge opening angles using laser scanning confocal microscopy. As compared with fluids consisting of spherical particles, studies of elongated semi-flexible molecules in contact with structured substrates are obviously more difficult due to the additional orientational and conformational degrees of freedom. To our knowledge, no work has been performed yet to trap semi-flexible spherocylinders in asymmetric restricted spaces. Studying such systems can provide insights into the influence of confinement on physical properties of soft matter.

M13 phages can be treated as polymer chains composed of homogeneous elastic material, where the persistence length characterizes the molecular stiffness. Therefore, suspensions containing M13 phages are considered to be ideal model systems for studying properties of soft condensed matter systems.[144] Spontaneous assembly of such colloidal particles can be achieved by evaporation of the phage-containing solution on a substrate.[145,146] Such evaporative assemblies have been successfully used in a number of different ways.[147] For instance, sessile droplets of a colloidal suspension can be evaporated on structureless mesoscale solid surfaces or on rationally designed spaces, *i.e.*, flat thin cells,[147] wedge geometries,[146] cylindrical channels,[87] or under the influence of external fields such as the frictional force.[14]

Here I study the self-organization and bending of M13 phages resulting from confinement on irregular stranded webs of thin a-C films using the Zeiss TEM and theoretical considerations. The aim is to study the possibility to control the orientation of M13 phages in two-dimensional nematic films by choosing structured substrates. The electron transparent a-C thin film was used to provide random and non-symmetric confining geometries with variable strand widths of the web film and also to obtain a high adsorption of viral particles on the substrate.[40] As a prerequisite for the present study we have ensured in chapter 4, that self-assembly and ordering of M13 phages on unstructured substrates takes place not only on a-C support films, but also on SiO_2 membranes.[40] Hence, I do not consider the self-organization process discussed in the following as a specific phenomenon of the supporting a-C web films.

5.3. Materials and Methods

WT M13 phage particles were generated and suspended in TBS at pH 7.4. A viral solution with a concentration of 0.2 mg/ml was prepared according to our previously reported method.[40] A 4 µl droplet of WT M13 phages was incubated for 5 min onto a copper grid coated with an a-C web film

(Plano GmbH, Germany) at ambient temperature to allow for the adsorption and self-ordering of the phages on the supporting web film. Here the suspension droplet containing rod-like particles formed a spherical sessile droplet on the solid surface. The incubation of phages leads to an increase in the 2D phage number density that can allow for the nematic configuration dominantly due to the effective entropic forces.

The SESAM microscope was used to carry out TEM investigations. All the samples were negatively stained using a 2% UA solution prior to the TEM characterization to provide the direct and close visualization of the M13 phages on complex geometries. BF-TEM images of phages on a-C web films were obtained and they were further analyzed to confirm the orientation of the molecules. To extract the angular orientation of the phages from the BF-TEM images, an adaptive thresholding algorithm was employed for segmentation of the particles. The edges were identified as the longest regions. Their orientation was estimated by fitting a spline to each edge and calculating its first derivative. The segmentation of the phages was finely tuned in order to minimize the noise in the plots arising from wrong identification by not considering regions with a major axis length below 4 nm and an aspect ratio lower than 2.6. The orientation of the phages was estimated as the orientation of the major axis of the ellipse and their position as its centroid. All the analysis was performed using the scikit-image image processing software package.[148] Furthermore, all data processing steps were carried out using ImageJ to calculate the radii and angle values and also using Mathematica software to calculate the mean orientations of the segments by means of the standard order parameter tensor.[149]

5.4. Bending Energy of Two-Dimensionally Confined Macromolecules

For a macromolecule in two spatial dimensions, the energy required to bend two segments of the macromolecule located apart a distance Δs by a subtending angle $\Delta\phi$ is given by[150]

$$U^{(seg)} = \frac{YI(\Delta\phi)^2}{2\Delta s}, \tag{5.1}$$

where Y is the Young's modulus and I is the area moment of inertia. These material properties are related to the persistence length l_p according to[151]

$$YI = k_B T l_p , \tag{5.2}$$

where k_B is the Boltzmann constant and T is the absolute temperature. Hence, the bending energy of a macromolecule of contour length L is given by

$$U^{(mol)} = \frac{1}{2} k_B T l_p \int_0^L ds\kappa^2(s) , \tag{5.3}$$

with the local curvature $\kappa(s) = d\phi/ds$. Here $s \in [0, L]$ is the contour coordinate along the macromolecule. The local curvature is a measure of the change of the macromolecule contour

direction as a function of the contour parameter. To simplify the calculation of the bending energy, a convenient representation of the contour of the macromolecules and their curvature is required. Here I consider the contour to be represented by a function $y(x)$ in a two-dimensional Cartesian coordinate system. For an analytical function $y(x)$ the local curvature is given by

$$\kappa(x) = \frac{d^2y}{dx^2}\left(1 + \left(\frac{dy}{dx}\right)^2\right)^{-\frac{3}{2}}, \tag{5.4}$$

because of $d\phi/ds = \tan\phi$ and $ds^2 = dx^2 + dy^2$. Hence, the bending energy in Eq. (5.3) can be written as

$$U^{(mol)} = \frac{1}{2}k_BTl_p\int_{x_0}^{x_L} dx \left(\frac{d^2y}{dx^2}\right)^2 \left(1 + \left(\frac{dy}{dx}\right)^2\right)^{-\frac{5}{2}}, \tag{5.5}$$

where the Cartesian coordinates (x, y) of the two ends of the macromolecule at $s = 0$ and $s = L$ are given by $(x_L, y(x_L))$, respectively. In the case of a contour given by an arc of radius R and subtending an angle θ with the circle center, Eq. (5.5) reduces to

$$U^{(mol)} = k_BT\frac{l_p\theta}{2R}, \tag{5.6}$$

since $y^2(x) = R^2 - x^2$ and $L = \theta R$. Hence, the bending energy associated with an arc is inversely proportional to the radius for a fixed angle subtended by the arc. On the basis of the bending energy given in Eqs. (5.3) and (5.5), properties of individual semi-flexible macromolecules such as DNA,[152,153] amyloid fibrils,[154,155] and unfolded proteins[156,157] have been extracted from two-dimensional atomic force and scanning tunneling microscopy images. However, the deposition method under consideration here organizes M13 phages into dense two-dimensional bundles where individual phages are closely packed. To provide a simple expression for the total bending energy of such a two-dimensional bundle consisting of N phages I consider a bundle shape given by an annulus sector of angle θ bounded by two concentric arcs of radii R_0 and $R_L = R_0 + (N-1)d$, where d is the diameter of the phages. Using Eq. (5.6) the resulting bending energy is given by

$$U^{(ann)} = k_BT\frac{l_p\theta}{2}\sum_{n=0}^{N-1}\frac{1}{R_0+nd} = k_BT\frac{l_p\theta}{2d}\left(\psi\left(N + \frac{R_0}{d}\right) - \psi\left(\frac{R_0}{d}\right)\right) \overset{R_0 \gg d}{\approx} k_BT\frac{l_p\theta}{2d}\ln\left(\frac{R_L+d}{R_0}\right), \tag{5.7}$$

where $\psi(z)$ is the digamma function.[158] Hence for given phage persistence length l_p and diameter d the bending energy in Eq. (5.7) depends on the three parameters R_0, R_L, and θ.

5.5. Results and Discussion

As shown in Figure 5.1a, the thickness of the supporting substrates of pure amorphous carbon web films with irregular and random strands was measured using EFTEM thickness mapping, based on the log-ratio method which gives the ratio of the characteristic mean free path λ for inelastic scattering of the material to the specimen thickness t.[159] The mean free path was calculated using a mean free path estimator script implemented in Digital Micrograph© (Gatan).[160] For the amorphous carbon films used in our experiments, a mean free path of 132.4 nm was determined. The corresponding t/λ map shows the analyzed area (see Figure 5.1b) to be relatively uniform, with a mean thickness of ~23 nm of the substrate film and at the edges (collar) up to ~55 nm. The sudden increase in thickness at the film edges might be due to bending of the thin film at the free-standing boundaries.

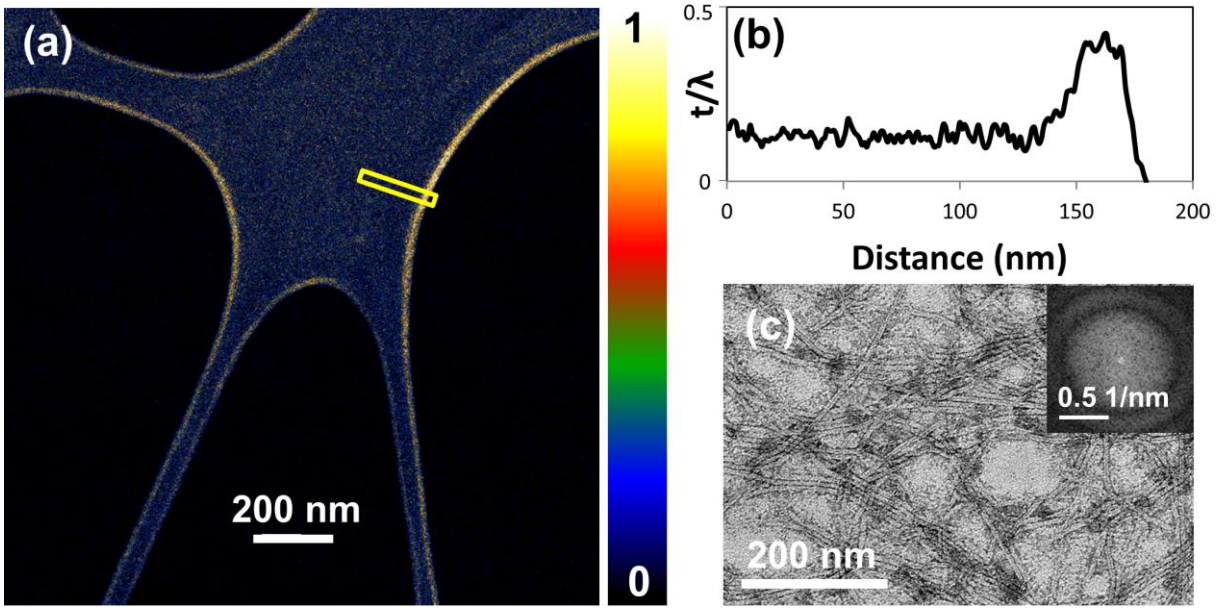

Figure 5.1. Thickness estimation of the carbon supporting film with a web-like 2D topology and randomly dispersed holes (black areas in (a)). (a) The EFTEM thickness map of the carbon web film. A line profile with an integration width of 40 nm (yellow rectangle) was taken from the area indicated to estimate the material's average thickness over the referred area. (b) The relative thickness profile (t/λ) along the length of the yellow rectangle in (a). The mean thickness of the film was measured to be ~23 nm on the flat surface and up to ~ 55 nm at the collar. The noise in the intensity profile might arise from the roughness of the carbon surface. (c) BF-TEM image of randomly oriented M13 particles on the a-C flat surface far from the surface edges and intersections. The inset shows the 2D FT image of the BF-TEM image confirming that the M13 phages formed an isotropic arrangement. The partial darkening of the phages is due to the heavy metals in the UA solution. Reproduced from Ref. 12 with permission from The Royal Society of Chemistry.

To study the effect of irregular spatial confinement on long semi-flexible M13 phages and their bending behavior, the phages were deposited onto carbon web films with asymmetric shapes. In the current chapter, unless otherwise stated, the term "surface" refers to the surface of the substrate solid phase that creates an interface with the phages. First, phage particles from a viral solution were incubated onto the surface. As seen in Figure 5.1c, on the structureless and wide surface areas far enough from the surface boundaries, the phages exhibit random orientations confirmed by the round intensity pattern with no preferential order of the FT image. In contrast, a close examination of the TEM images revealed that a significant morphological evolution occurred in the intersections where

the carbon strands meet (Figure 5.2). In such restricted geometries, the very long phages are confined to two-dimensional multi-stranded intersections due to their semi-flexibility. As illustrated in Figure 5.2, I have recorded images of molecules on different Y intersections (junctions) having a straight leg and two branching sections. A feature common to all the obtained images is that on a single and narrow carbon strand (the straight leg of the Y junction) the mean molecular alignment can be described by a unit vector field, referred to as the director, which is oriented parallel to the axis of the strand. The director is anchored parallel to the surface edges and consequently to the axis of the strand with a finite width. When constrained to strands, the M13 filamentous particles adopt a configuration that matches the confining boundary conditions in order to minimize the total free energy. Within the framework of a density functional theory, an enrichment of elongated particles lying parallel and close to the corner of a wedge has been predicted and interpreted in terms of an effective potential which pushes the particles to the corner of the wedge.[161]

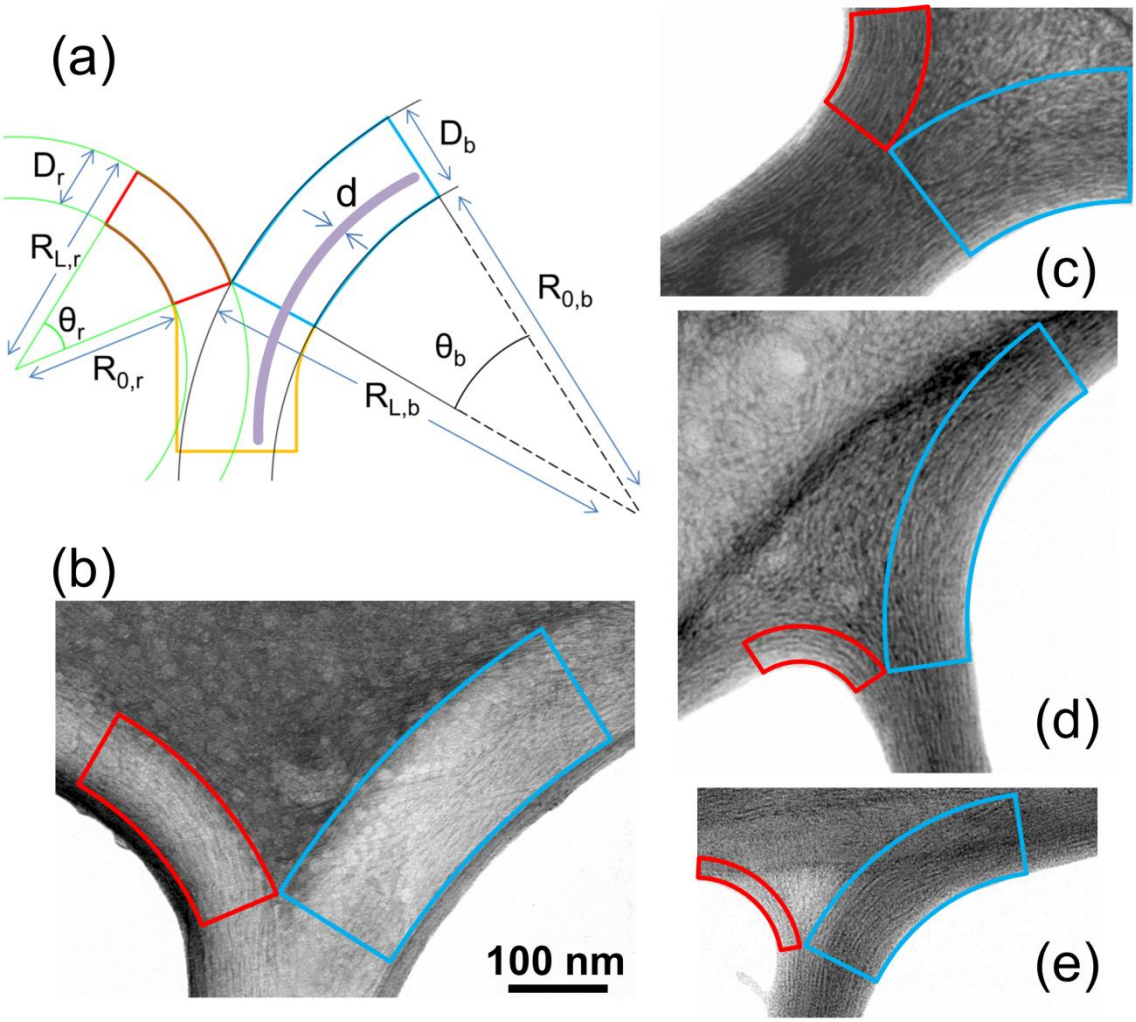

Figure 5.2. (a) Schematic representation of a Y intersection showing a straight leg (yellow section) and two branching sections denoted by red and blue annulus sectors. The red and blue lines mark the boundaries of the two annulus sectors for which the bending energy of the aligned phages of thickness *d* can be calculated analytically according to Eq. (7). (b) - (e) Confined and immobilized M13 phages on four complex intersectional geometries with different intersection widths and topology. Close to the curved surface edges the phages are oriented with their main axis parallel to the periphery of the substrate surfaces. Defects in the nematic ordering are visible where the alignment imposed by the arc-like substrate edges meets the nematic configuration at the top of the Y junctions. The position of the defect can be controlled through the surface geometry such that from panel (b) to (e) the defect is pushed to the annulus sector marked in red in order to reduce the free energy

($\boldsymbol{D_r}$ = 87, 76, 33 and 18 nm, respectively). Partial darkening effects of the molecules arise from heavy metals in the UA solution. Scale bars are identical in (a) – (e). Reproduced from Ref. 12 with permission from The Royal Society of Chemistry.

In the case of a Y junction, the frustration of the director field due to the anchoring at the surface edges leads to a defect of the director field. The phages shown in Figure 5.2b-e, start to form two bundle sections (red and blue sections consisting of N_r and N_b particles, respectively) when coming to the intersection from a narrow single strand (consisting of $N_r + N_b$ particles). At the intersection the director splits into two different orientations determined by the orientations of the surface edges of the substrate. In the case of long macromolecules, their interaction with the surface edges, intermolecular interactions and macromolecular stiffness determine the shape of the director field.[162,163,164]

To interpret the experimental results with the help of Eq. (5.7), Figure 5.2b-e show the BF-TEM images together with red and blue annulus sectors of subtended angles θ_r and θ_b in which N_r and N_b phages, respectively, form bundles with the same orientation parallel to their nearest substrate edge. In particular, the edges of the substrate and its collar at the boundary determine the orientation of nearby phages as mentioned above. This orientational order is further induced to the neighboring molecules via intermolecular forces leading to formation of oriented bundles of phages. Hence, close to the curved edges of the surface the phages tend to align parallel to the edges due to effective entropic forces and attractive van der Waals forces acting between them and the collars along the edges of the carbon surface. It should be noted that the drying process of the phages on the substrate can only modify the strength of the total effective forces acting on the orientational order of phages due to the increase of phage concentration. In other words, phages close to the surface edges orient and align such that their main axis directions become parallel to the periphery of the surface boundary. The defect, beyond which the molecules are geometrically frustrated, is located at the point at which the two annulus sectors meet.

The parameters $R_{0,r}, R_{L,r}, \quad R_{0,b}, R_{L,b}, \theta_r, \theta_b, D_r = R_{L,r} - R_{0,r}$ and $D_b = R_{L,b} - R_{0,b}$ characterizing the red and blue annulus sectors in Figure 5.2b–e were determined according to the illustration in Figure 5.2a. Here the parameters $R_{0,r}$, $R_{0,b}, \theta_r$ and θ_b follow from the shape of the surface edges. As might be expected, the edges of the Y junctions shown in Figure 5.2b-e do not form exactly circular arcs, but these simple geometric lines serve as initial approximations. Lastly, the parameters $R_{L,r}$ and $R_{L,b}$ follow from the phage self-assembly process and they determine the numbers N_r and N_b of the aligned phages in the red and blue annulus sectors, respectively. It is worthwhile to emphasize that in our experimental conditions, the colloidal concentration is considerably lower than the one at the isotropic to nematic phase transition of the unconfined bulk fluid. The orientational ordering at such low concentrations is induced by the spatial confinement, which is consistent with an experimental study on confined actin filaments[164] and earlier theoretical predictions.[161]

To further confirm the orientation of the molecules inside the red and blue annulus sectors, I analyzed the images (c)-(e) in Figure 5.2 in detail (see Figure 5.3). Due to the complexity of extracting the contour of an individual viral particle inside a phage bundle, I segmented the images into sub-images which can represent the form of an individual phage particle and its bending behavior and an angular orientation was assigned to each identified segment.

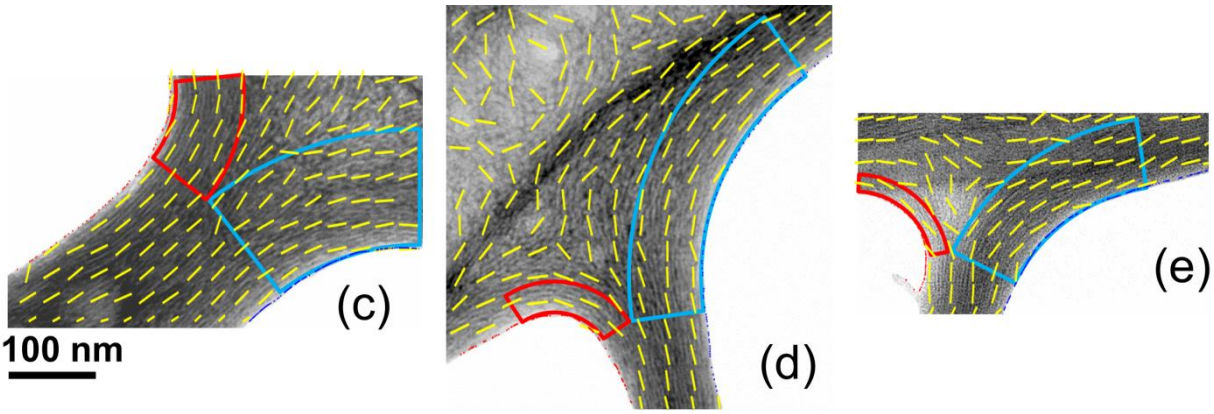

Figure 5.3. Mean orientations of the particles (marked with yellow lines) extracted from the analysis of the images (c) - (e) in Figure 5.2. The mean orientation diagrams are superimposed on the raw TEM images showing that within the assumed annulus sectors the molecules tend to align parallel to their closest surface edge. The orientations are calculated by averaging over the orientation of the particles within circular domains of radius 20 nm. Scale bars are identical. Reproduced from Ref. 12 with permission from The Royal Society of Chemistry.

Figure 5.2 and 5.3 illustrate that the position of the defect can be controlled through the surface geometry. In general, with increasing ratio $R_{0,b}/R_{0,r}$ and fixed angles of the annulus sectors the defect is pushed toward the annulus sector marked in red in order to reduce the total bending energy [Eq. (5.7)] of the phages located in the red annulus sector. Therefore, the resulting director fields given by the orientation of the phages are non-symmetric while rather symmetric director fields have been found for worm-like fd particles confined by symmetric wedges [143] and for carbon nanotubes close to flat substrates.[165,166,167] The radii $R_{0,r}$, $R_{0,b}$, $R_{L,r}$, $R_{L,b}$ for the red and blue sectors of all BF-TEM images in Figure 5.2 and the ratios $\delta = (R_{L,r} - R_{0,r})/(R_{L,b} - R_{0,b})$ for red and blue sections are presented in Table 5.1. From the table, it is apparent that the ratio of the width of the red sector to the width of the blue sector decreases from Figure 5.2b to e.

Table 5.1. Radii $\boldsymbol{R_{0,r}}$, $\boldsymbol{R_{0,b}}$, $\boldsymbol{R_{L,r}}$, $\boldsymbol{R_{L,b}}$ characterizing the red and blue annulus sectors in Figs. 5.2b–e, and the ratios $\boldsymbol{\delta = (R_{L,r} - R_{0,r})/(R_{L,b} - R_{0,b})}$. Reproduced from Ref. 12 with permission from The Royal Society of Chemistry.

Radius $\frac{a}{b}$ (nm)	**(b)**	**(c)**	**(d)**	**(e)**
$\boldsymbol{R_{0,r}}$	290_{-15}	123	72	90
$\boldsymbol{R_{0,b}}$	697_{-18}	264	289	200
$\boldsymbol{R_{L,r}}$	377_{-3}	199^{+12}	105_{-7}	108^{+5}
$\boldsymbol{R_{L,b}}$	836^{+3}	395_{-12}	373^{+7}	281_{-5}
$\boldsymbol{\delta}$ $\frac{a}{b}$	$0.63_{-0.03}$	$0.58^{+0.16}$	$0.39_{-0.10}$	$0.22^{+0.08}$

[a,b] Upper and lower deviation limits, respectively, in the radii and δ values.

Equations (5.1) – (5.7) presented above are applicable to macromolecules that can be modeled as homogeneous worm-like objects. At the protein level, M13 phages are not homogeneous, but the

surface-induced phage bending deformations occur on a larger length scales, because $R_{0,r}$, $R_{0,b}$, $R_{L,r}$, $R_{L,b} \in [72 - 836]$ nm for the samples shown in Figure 5.2. Therefore, the equations presented here can be applied to the M13 phages keeping in mind that approximating the edges of the amorphous carbon surface as circular arcs represents an oversimplification.

This, however, allows one to derive analytic expressions for the bending energy. In order to understand the values of the larger radii $R_{L,b} = R_{0,b} + (N_b - 1)d$ and $R_{L,r} = R_{0,r} + (N_r - 1)d$ of the blue and red annulus sectors displayed in Figure 5.2, it is helpful to consider the free energy

$$F = {U_b}^{(ann)} + {U_r}^{(ann)} - TS\ . \tag{5.8}$$

Here ${U_r}^{(ann)}$ and ${U_b}^{(ann)}$ are the bending energies of the red and blue annulus sector of a Y junction calculated according to Eq. 5.7 and S is the entropy. To compute the entropy $S = k_B\, ln\, \Omega$ due to orienting N_r phages to the left and N_b phages to the right at a Y junction, one has to deduce the number of states according to $\Omega = (N_r + N_b)!/(N_r!\, N_b!)$. Hence the last term in Eq. (5.8) exhibits a minimum at $N_r = N_b$ corresponding to an equal number of phages oriented to the left and to the right at a Y junction. However, the sum of the first two terms in Eq. 5.8 exhibits a minimum at $N_r \neq N_b$ for two arc-like edges of different shape, *i.e.*, $R_{0,r} \neq R_{0,b}$ and $\theta_r \neq \theta_b$, where θ_r and θ_b are the angles of the red and blue annulus sectors, respectively. Therefore, minimization of F leads in general to different values of N_r and N_b in line with the experimental results shown in Figure 5.2. Nevertheless, the simple theoretical approach provides an explanation for the different values of N_r and N_b. Properties of the system are characterized by the free energy which includes both energetic and entropic contributions. The competition of these contributions determines the resulting structures.

Understanding the orientational behavior of phages on complex geometries of carbon web films can offer the active use of topological defects in controlling of liquid crystal flow, because the presence of topological defects strongly affects the flow of liquid crystals which elastically interact with surfaces.[168] Besides, our results could be used in the application of liquid crystals (*e.g.* memory effects) in topological manifolds which have interconnected porous media,[169,170] similar to our carbon web films.

5.6. Conclusions

In this chapter, I studied semi-flexible M13 phages in contact with irregular stranded webs of thin a-C films using TEM and theoretical considerations. In this work, I showed that on the structureless and wide surface areas far from the a-C surface edges, the phages exhibited random orientations. However, the orientation of M13 phages in two-dimensional nematic films was controlled by the orientation and curvature of the substrate edges. When constrained to surface strands, the M13 phages adopted a configuration that matches the confining boundary conditions in order to minimize the total free energy. An annulus sector was superimposed on these oriented phage bundles that allowed us to derive analytic expressions for the bending energy of such oriented bundles. Our theoretical approach provides an explanation for the different number of phages orienting close to the surface edges with different local curvatures. By comparing the self-assembly on differently shaped a-C substrates, it was demonstrated that the alignment of the phages can be controlled by choosing appropriate substrate

shapes. This offers a convenient means to fabricate designed structures of orientationally ordered M13 phages. The understanding of such systems opens up new possibilities for defect engineering of liquid crystals which can be beneficial for the applications of liquid crystals in the presence of surface microscopic pores and irregularities.

Contributions to this chapter:

Pouya Moghimian and Ludger Harnau (MPI-IS) designed the study. Pouya Moghimian performed the research. Sandra J. Facey and Bernhard Hauer (University of Stuttgart) prepared the phage solutions. Francisco de la Pena (University of Cambridge) carried out image analysis. Nima Farahmand Bafi and Pouya Moghimian analyzed the data. Ludger Harnau, Vesna Srot (MPI-FKF) and Peter A. van Aken (MPI-FKF) jointly supervised this work. The published article (Ref. 12) was written by Pouya Moghimian and Ludger Harnau.

6. Chapter 6. Biomineralization and Biotemplated Synthesis of Organic–Inorganic Hybrid Multilayers

6.1. Abstract

Bio-inspired fabrication of organic–inorganic nano-hybrid structures, where inorganic nanomaterials are templated by the organic component, *i.e.* biological entities, is of high interest due to the broad range of applications of these structures.[43,47,53,103,171] Protein-based bottom-up synthesis of functional nanomaterials and devices is one of the most promising areas in bio-nanotechnology. Here, I demonstrate that organic assemblies can serve as biologically controllable scaffolds for the deposition of inorganic nanoparticles. In this work, I used our findings presented in the chapter 4 and I employed a C-sputtered substrate to assemble densely-packed wild-type M13 phages for the controlled mineralization of ZnO particles. Our aim was to construct layered structures consisting of organic and inorganic materials which contain alternating layers on a smooth substrate. The microstructure, elemental composition, and also the integrity of the organic and the biologically-templated inorganic layers were studied. A uniform nano-hybrid structure without significant thickness fluctuations was fabricated by using a high concentration of M13 phages and a carbon-coated substrate. The current study gives insight into the combination of organic–inorganic materials into a multilayered structure, which could be used as a constituent in electronic devices such as transistors.

Table of contents: Assembly of M13-ZnO bilayered structures.

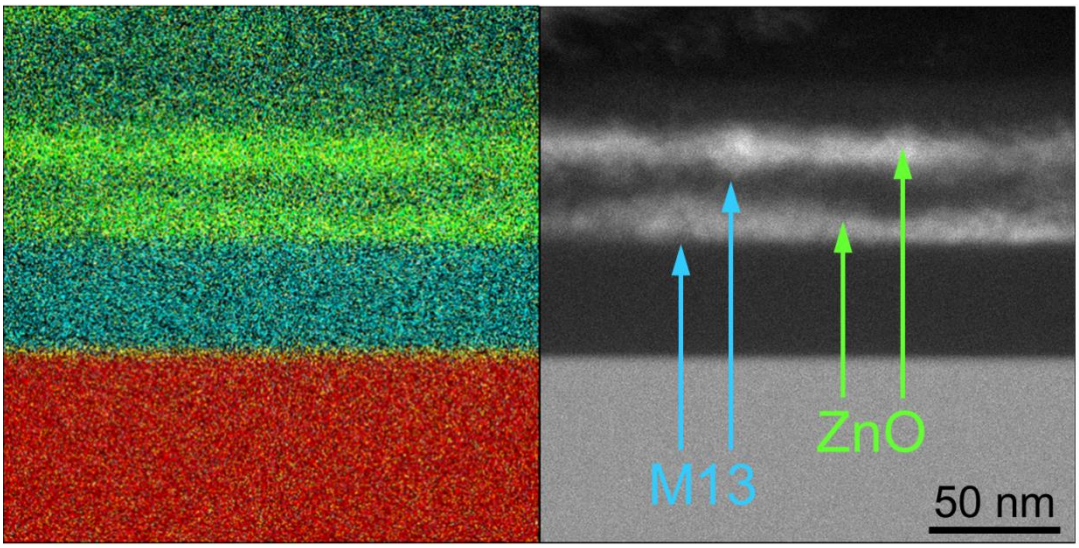

Part of this chapter has been published in Ref. [58]

6.2. Introduction

Different mechanisms can be adopted from nature to trigger the nucleation and growth of desired inorganic nanostructures and consequently to obtain organic–inorganic hierarchical nanostructures, in which the organic nanocomponents are considered as the scaffolds.[172] The WT M13 phage has been the focus of extensive studies owing to its well-defined structure for protein-based scaffolds and also its ability to mineralize nano-inorganic materials at ambient temperature.[173] The coat proteins of the viral particles can be genetically engineered for a specific inorganic target to allow for selective nucleation and growth of the desired inorganic materials. Also, the high aspect ratio of M13 phages makes them attractive templates for the fabrication of inorganic nanowires. M13 phages have recently been engineered to specifically synthesize gold nanoparticles,[174] cadmium selenide,[53] copper sulfide[18] and barium titanate[55] nanocrystals. However, non-modified and non-engineered viruses are still able to template the deposition of inorganic materials and thus they can be used to fabricate a variety of complex hybrid nanostructures.[47] For instance, the tobacco mosaic viruses (TMV) have been reported to mineralize zinc oxide (ZnO) from a deposition solution.[57] This allows us to fabricate intelligent, *i.e.* responsive, organic–inorganic systems with desired properties that have high potential for use in field-effect transistors.[57] Such layered structures containing alternating organic and inorganic layers also showed enhancements in photoconductivity and mechanical properties compared to only inorganic monolayers.[175,176] The study of the integrity and elemental composition of the layers and the interfaces could lead to a more precise control over the properties of such structures.

6.3. Materials and Methods

Two viral solutions with concentrations of 1.4×10^{13} and 3.5×10^{14} pfu/ml were prepared in TBS buffer. The convective assembly technique, was used to deposit the filamentous M13 phages onto the smooth Si and C-coated Si surfaces. To form viral layers on the surfaces, the viral particles were deposited by pulling a meniscus containing the virus solution with a specific concentration across the substrate at a constant rate (1.2 mm/min) using a motion control system. The glass cover slips and the silicon wafers (1.5 × 1.5 cm) that were used in the deposition process were cleaned by consecutive sonication in Milli-Q water and a mixture of 1:1 acetone:ethanol and they were finally dried under N_2 flow prior to use.[177] The coating of homogeneous 40 nm carbon on the silicon wafers was carried out under high vacuum using a magnetron sputtering system (FMK) at room temperature.

The ZnO deposition solution was prepared according to the previously reported procedure.[57,178] Briefly, equimolar methanol solutions of zinc acetate dihydrate ($Zn(OOCCH_3)_2 \cdot 2H_2O$) (puriss. p.a., Fluka), polyvinylpyrrolidone (PVP) (PVP10, M = 10 000, Sigma-Aldrich), and tetraethylammonium hydroxide (TEAOH) (purum, Fluka, ~25 % in methanol) were used to prepare the ZnO deposition solution. The viral films immobilized on C-coated Si wafers were immersed in the ZnO deposition solution and incubated in an oil bath for 1.5 h at 60 °C to complete one deposition cycle. After the deposition cycle, methanol (VLSI Selectipur, BASF) was used to vigorously wash the wafer surface and to remove all the unbound ZnO particles. Thereafter, the wafer was dipped in fresh deposition solution for the next deposition cycle.

SE images were acquired by the Zeiss DSM 982 Gemini SEM operating at 3 kV. Samples that had not undergone the mineralization process were coated with a thin (< 1 nm) layer of PtPd using the sputter coater (Cressington, 208 HR) prior to the SEM investigations. The surface roughness of the

layered structure was measured at ambient temperature by AFM in tapping mode using the Nanoscope III Multimode instrument. The JEOL ARM200F microscope was used to carry out BF-STEM and HAADF-STEM imaging combined with EDX spectroscopy mapping. Cross-sectional specimens were prepared in a wedge-shaped geometry using an automatic tripod polisher and subsequently Ar^+ ion-beam thinned in an ion polishing system (PIPS, Gatan) at 2.7 keV.

6.4. Results and Discussion

First, the convective assembly method was used to immobilize phages on a cleaned silicon surface. Using a cleaned cover slip, 3 µl of a phage solution with a concentration of 1.4×10^{13} pfu/ml was receded at a constant rate on the substrate surface. As shown in Figure 6.1a, mostly branched bundles of phage particles with a width of ~50 nm were formed on the silicon substrate. This bundling lowers the apparent concentration of the particles and consequently lowers the substrate's coverage of M13 particles. The immobilized phage bundles on the silicon wafer were subsequently immersed into the ZnO deposition solution for 2 deposition cycles. It was observed that the phage particles mineralized ZnO nanoparticles on their body surface (see Figure 6.1b). I have monitored the morphology and chemical composition of these organic–inorganic composites using EDX (see Figure 6.1c,d). Figure 6.1c shows that there are ZnO particles, which are not bound to the phage particles, formed on the silicon surface. This phenomenon has also been observed in previous studies.[57] This could occur during the mineralization cycles considering the fact that ZnO particles could form on the surface due to heterogeneous nucleation at preferential sites of the crystalline surface.[179,180] Another reason could be due to the deposition of already-formed ZnO particles in the mineralization solution (*via* homogeneous nucleation). These results suggest that one could construct a phage-controlled nano-hybrid structure using M13 phages and ZnO as alternating organic and inorganic components if the following conditions are fulfilled: using a larger amount of phage particles, enough to cover the substrate, and also using a substrate that can template a packed and uniform organic film.

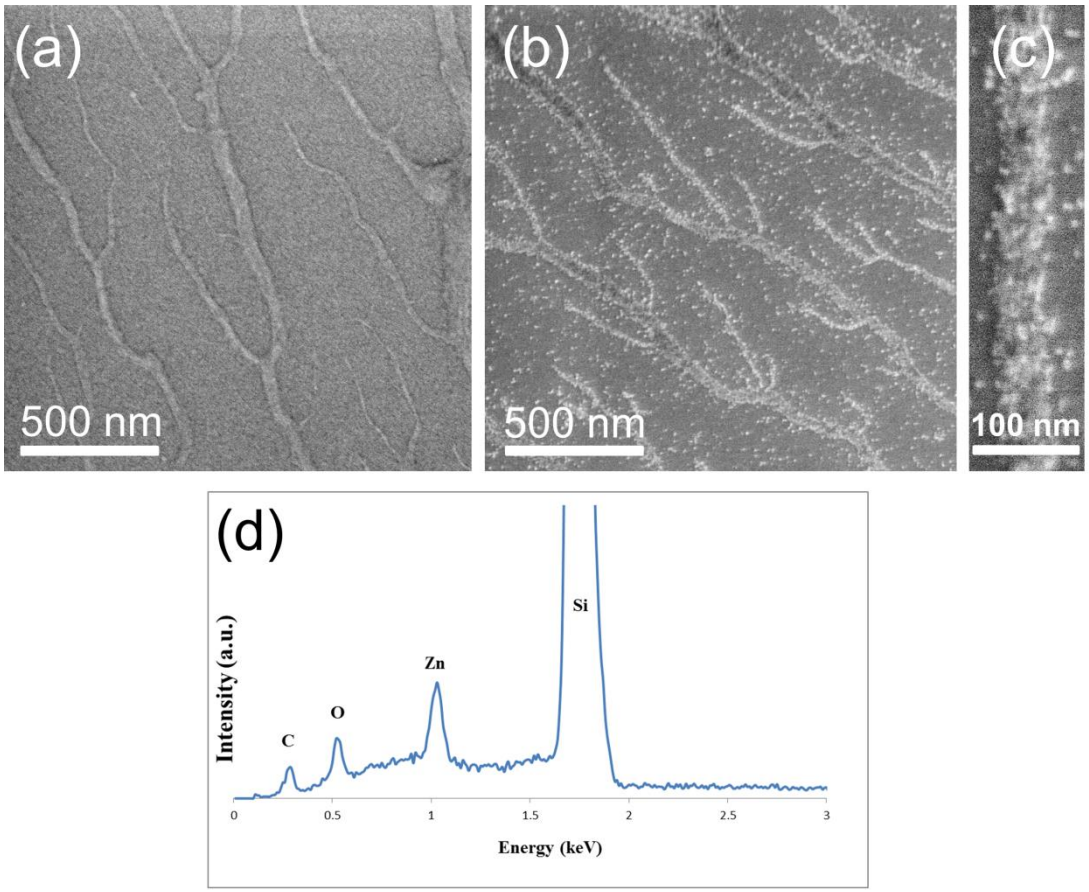

Figure 6.1. Plan-view SEM images of (a) adsorbed M13 phage bundles from a 3 µl phage solution with a concentration of 1.4×10^{13} pfu/ml on a cleaned Si surface. (b) Mineralized ZnO nanoparticles on the phage particles. (c) A single magnified phage bundle that mineralized ZnO nanoparticles with a diameter of ~10 nm. (d) EDX spectrum obtained from a phage bundle with the mineralized ZnO nanoparticles. The background is due to the Bremsstrahlung X-rays. Adapted from the Ref. [58] from the International Journal of Materials Research, IJMR 2016, © Carl Hanser Verlag, München.

To successfully develop a layered structure, 5.5 µl of a phage solution with a concentration of 3.5×10^{14} pfu/ml was withdrawn over a 40 nm C-coated Si surface and this was subsequently subjected to two cycles of ZnO deposition to grow a ZnO film[178,181] on the phage coat proteins. The whole process was repeated two times to fabricate a layer-by-layer structure containing alternating M13–ZnO layers. In chapter 4, I have shown that M13 phages can be well-aligned and organized on a thin carbon surface.[40] Therefore, the cleaned silicon substrate in this experiment was coated with a thin layer of carbon. Figure 6.2 shows a BF-STEM image (a) and a HAADF-STEM image (b) of the resulting layered structure along with an illustration of the system, which was protected during the TEM sample preparation using a glue film. The structure contains two M13–ZnO alternating layers, which show homogeneous sheets of M13 phages and mineralized ZnO particles. The ZnO layers in Figure 6.2b exhibit bright contrast as they correspond to a larger average Z compared to the M13 phages. The ZnO and M13 layers were uniformly assembled on the C-sputtered Si wafer and were continuous over large scales across the sample. This was obtained, as shown in chapter 4, due to the fact that using a-C surface favors the formation of densely-packed and assembled layers of M13 phages, which in turn allows for the deposition of a smooth sheet of ZnO. Moreover, there was no notable thickness fluctuation of the layers over the cross-section of the sample. There is always uncertainty in the exact state of dryness (shrinkage) of the viral particles on a substrate,[31,182] but from the relative thicknesses of the different layers it could be inferred that the organic layers were only a

few phages thick. However, at some areas across the sample, a slight interpenetration of organic and inorganic layers was evident that most likely originates from the multilayer preparation process, in which the immobilized phages are dipped in a zinc solution. Unfortunately, it is difficult to predict the stability of the interface between the two materials.[183] However, it is believed that phages could be detached from the surface during the preparation process and consequently ZnO particles could deposit through the organic layer. Tracing of the interface between the carbon substrate and the first deposited phage layer was rather difficult due to the similar composition of these two materials and the thinness of the first phage layer. This thinness might be due to very low roughness of the C-sputtered surface compared to the roughness of the following inorganic layer which could lead to lower amounts of adsorbed molecules on the carbon surface.[112] The presence of glue on the top of the bilayer indicates that all the layers were protected and no damage to the layers occurred during the TEM sample preparation and therefore the original structure of the bilayer was preserved. The 3D surface morphology and *RMS* roughness of the surface of the layered structure were studied by AFM and are presented in Figure 6.2c. The results indicate a surface roughness of the structure with *RMS* = 14.6 nm, which is about twice the phage thickness. A low thickness of ZnO layers could be a reason for the above-mentioned low surface roughness value, because it could be speculated that by having a thicker ZnO layer, its roughness increases and this could disturb the alignment and homogeneity of the hosted phage layers.

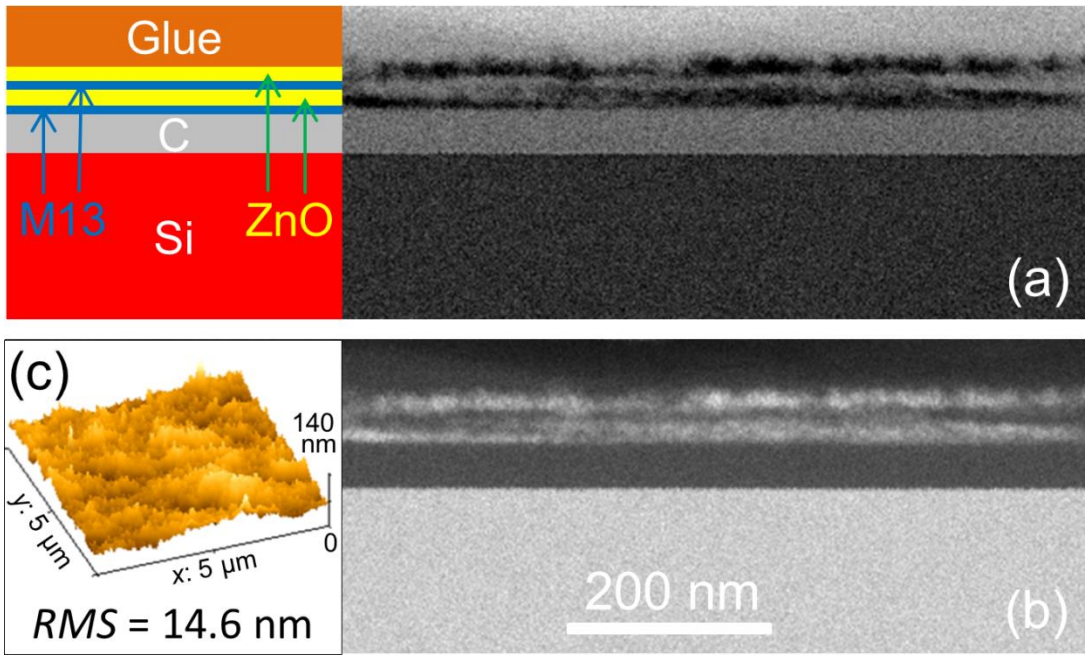

Figure 6.2. (a) BF-STEM image of the cross-section of the layered sample, indicating two homogeneous and thin layers of M13 phages and ZnO (blue and yellow stripes respectively) which were assembled on a C-sputtered Si substrate. An illustration is included showing the layered system. The glue on the top of the specimen was deposited as a protective layer during the TEM sample preparation. (b) HAADF-STEM image of the cross-section of the sample showing the presence of alternating layers of ZnO and M13 phages on the C-coated silicon substrate. A slight interpenetration of the layers is observable in certain areas. The scales in (a) and (b) are identical. (c) AFM 3D image of the surface morphology and *RMS* value of surface roughness of the layered structure within a scanned box size of 5 × 5 µm^2. Reprinted from the Ref. [58] from the International Journal of Materials Research, IJMR 2016, © Carl Hanser Verlag, München.

At each step of the multilayer fabrication, the surface of the layers was imaged by means of SEM. As shown in Figure 6.3, the first viral film along with mineralized ZnO nanoparticles forms an aligned structure on the substrate. The next viral film was deposited in the same orientation and it forms an aligned organic film. Thereafter, the last inorganic layer (ZnO) was highly homogenous and the ZnO nanoparticles were deposited on the directionally aligned phages. It could be stated that the first well-aligned viral film (on the carbon surface) acts like a rubbed surface that promotes the orientation of the following organic layers.[184] This is an interesting finding that starting with an aligned and oriented organic layer on a carbon surface I can construct a multilayered structure with a homogenous and a directional structure.

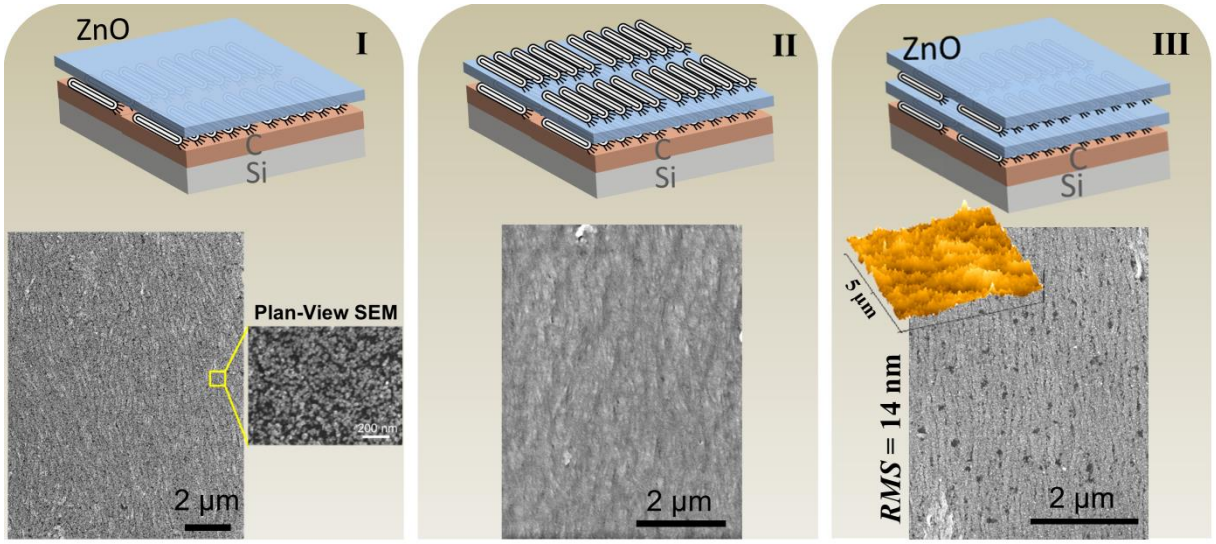

Figure 6.3. SEM images of the layers of the hybrid structure. (I) First ZnO layer mineralized on the top of the viral film. (II) Aligned viral film forming on the mineralized ZnO. (III) The second and last ZnO layer forming on the very top.

Although the layered structure of the sample was apparent in Figure 6.2, the STEM-EDX mapping further confirmed that the two layers of M13 phages and ZnO were formed in an alternating fashion (see Figure 6.4). The ZnO layer was mainly composed of Zn, and O. The weak C signal in these regions can be attributed to the M13 viral particles that have penetrated through the ZnO layer. The M13 phage layer was mainly composed of C.

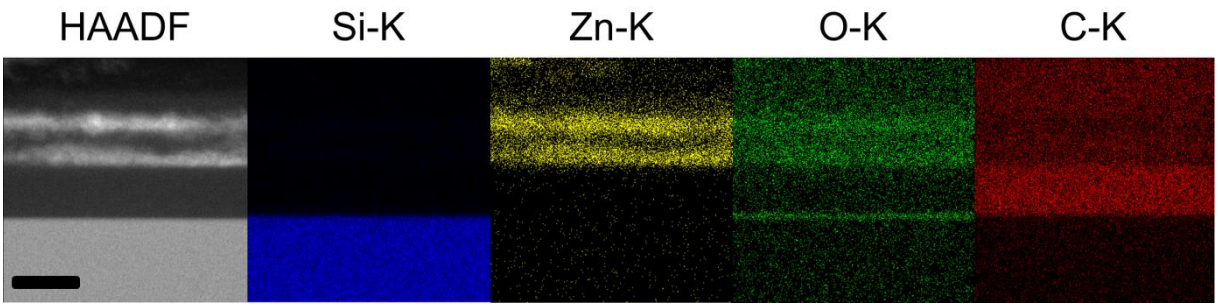

Figure 6.4. STEM-EDX elemental mapping (Si K edge, Zn K edge, O K edge and C K edge) and the corresponding HAADF image of a cross-section of the layered sample showing the presence of alternating layers

of ZnO and M13 phages on the C-coated silicon substrate. The scale bar represents 50 nm. Reprinted from the Ref. [58] from the International Journal of Materials Research, IJMR 2016, © Carl Hanser Verlag, München.

The Zn signal in the phage layer could be attributed to (i) the slight interpenetration of ZnO into the M13 phage layer and (ii) to the vertical projection of the layers considering the cylindrical shape of the phages with the mineralized ZnO nanoparticles. The cylindricality of phages results in a sinusoidal shape of the phage layer surface and this can in turn lead to the presence of Zn signal in the organic layers. Additionally, the carbon signal on the top of the structure shows the presence of the glue that capped the specimen during the TEM sample preparation as a protective layer. The O signal at the top of the silicon substrate and below the carbon coat layer can be attributed to the oxidation of the silicon when it was exposed to air before carbon coating.[185]

6.5. Conclusions

As a part of the current thesis, I successfully assembled a phage-controlled nano-hybrid structure on a carbon-coated silicon wafer using wild-type M13 phages and ZnO as the organic and the inorganic layers, respectively. Double alternating layers were uniformly grown on a highly smooth C-sputtered silicon wafer using the biomineralization process. In this project, the a-C surface was chosen because M13 phages have shown in chapter 4 to have high affinity to form assembled and densely-packed layers on a-C surfaces. In this chapter, it was confirmed that a-C surfaces are promising films to host directionally oriented phages over long length scales. The structure, elemental composition, and also the integrity of the alternating biologically-templated inorganic multilayers were characterized by means of SEM and STEM imaging in conjunction with analytical techniques. A homogeneous organic–inorganic hybrid structure without significant thickness fluctuations and with limited interpenetration of the interfaces was achieved. The conditions of the multilayer assembly process could result in a slight interpenetration of the adjacent organic and inorganic layers. Just as important, the homogeneity of the templating layers profoundly affected the evenness of the following layers and the roughness of the multilayered structure. This effect was reduced in our system by using a thin carbon film as the substrate in order to obtain a smooth and homogeneous layer-by-layer structure. This work provides information for the templating of organic–inorganic multilayers at the nanoscale, which might have potential in the construction of novel multicomponent electronic devices.

Contributions to this chapter:

Pouya Moghimian, Stefan Kilper (MPI-IS) and Dirk Rothenstein (University of Stuttgart) designed the study. Pouya Moghimian and Vesna Srot (MPI-FKF) performed the research. Sandra J. Facey (University of Stuttgart) prepared the phage solutions. Reinhart Völker (MPI-IS) carried out the carbon film deposition. Mahdieh Aghamohammadi (MPI-FKF) did the AFM work. Bernhard Hauer (University of Stuttgart), Joachim Bill (University of Stuttgart) and Peter A. van Aken (MPI-FKF) jointly supervised this work. The published article (Ref. 58) was written by Pouya Moghimian.

7. Chapter 7. Conclusions and Future Directions

7.1. Concluding Remarks

This thesis focuses on (i) the structure and the stability of M13 phages as liquid crystal model systems in different organic solvents, (ii) the fundamental understanding of the behavior and self-assembly of liquid crystals on structured and unstructured surfaces, (iii) the biomineralization process of inorganic materials by M13 phages in solution, and (iv) the bottom-up synthesis of novel hybrid organic–inorganic multilayered structures based on our understanding of the liquid crystal phases, the materials interaction (substrate-molecule specific interactions and molecules-inorganic interactions), and the biomineralization process.

In chapter 1, the objectives and the main challenges of this research thesis are introduced. M13 phages were introduced as our liquid crystal model system in this thesis. The liquid crystal (LC) fundamentals and different LC phases as well as the self-assembly behavior in solutions were discussed in detail. Furthermore, possible defects that can occur in the liquid crystalline structures were classified. Biomineralization was discussed as a tool for the construction of organic–inorganic hybrid structures.

In chapter 2, all characterization and experimental techniques that were used in this research thesis, are explained. SEM, TEM and AFM principles were described and they were shown to be prominent tools for the characterization (imaging and analytics) of our organic and inorganic systems. Contact goniometry method was described as a tool for the investigation of the hydrophobicity of solid surfaces. Our in-house-built apparatus (*i.e.* convective assembly) was introduced as a promising tool to assemble layers of rod-like phages from a pulling solution in a directional fashion. The design and the setup of this apparatus were done as a part of this thesis project.

In chapter 3, I have presented the results on the structural integrity and stability of filamentous M13 phages when exposed to different organic media, as the first step, to understand the structural behavior of these macromolecules. Yielding conditions to maintain the structural integrity of viruses leads to an increased understanding of the factors that disrupt their structure. It has been shown that phages would denature in polar organic solvents as compared to nonpolar solvents. The exposure of M13 phages to apolar solvents had no effect on the structure of the phages for up to 8 h. In contrast, phages showed ~8-fold contraction into rod-like I-forms and to flattened spheroids with ~12 nm diameter upon exposure to polar organic solvents. It was concluded that the fragmentation and as a consequence denaturation of phages can be understood by considering three role-playing factors: Solvent hydrogen-binding capacity, hydrophobicity and water miscibility. Hexane, that is a non-polar hydrophobic organic solvent, was shown to be incapable to compete for the hydrogen bonds between the phage coat proteins and therefore it was not able to deform the native structure of the phages. In contrast, polar solvents employed in our study (chloroform, THF and toluene) were able to break the hydrogen bonding and the hydrophobic interactions between the phage coat proteins. Higher polarities of the solvents used in our experiments, had an influence on breaking the inter-coat protein forces and even weakening the van der Waals interactions between the ssDNA and the coat proteins. The latter can lead to a collapse of the viral structure. I used this knowledge to find appropriate conditions in which phage assemblies can keep their primary structure upon exposure to solvents for long periods of

time (up to 8 hours). This can be used in the developing topic of research that is the control of macromolecular assemblies with hierarchical frameworks.

In chapter 4, I have reported the adsorption and self-assembly of macromolecules (M13 phages) on flat (*i.e.* unstructured) surfaces. The role of different substrates (SiO_2 and a-C) was also investigated and reported in terms of surface chemistry and competitive electrostatic interactions. This was a necessity in the growing field of self-assembly because I have shown that, not only the conditions of the bulk sample control the liquid crystalline phase, but also the chemistry and surface properties of the adsorbent have an influence on the average orientation of the molecules. Obtaining directionally organized layers of M13 phages was a challenge due to their extremely low thickness, flexibility, and high affinity for bundle formation. In order to investigate the role of the surface on the adsorption of phages, the self-assembly was studied in two liquid crystalline regions: in the extreme isotropic region and above the nematic threshold. Our results revealed that the low concentration of M13 phage solution (1.4×10^{13} pfu/mL) leads to the disordered phase of viral particles on the SiO_2 surface. Phage bundles were formed on the SiO_2 surface, which resulted in a decrease of the apparent concentration of filamentous phages. Therefore, the trend of the system was toward the formation of an isotropic phage distribution. However, when the same solution was deposited on a-C film, the molecules showed a degree of alignment. By increasing the concentration of the primary phage solution above the nematic threshold (3.5×10^{14} pfu/mL), phages showed a high degree of alignment on the a-C film. On the SiO_2 film, besides having a high degree of orientation, molecules showed branched arrays on the surface. This can be attributed to the fact that SiO_2 has a smooth and hydrophilic surface, whereas, a-C has a hydrophobic surface and therefore causes weak interactions between the phages and the solid surface. This is believed to allow for the higher mobility of phages on a-C surface and further directional stacking of the 2D viral film. Our work demonstrated that under specific experimental conditions, the a-C film is a promising host for highly oriented layers of M13 phages compared with SiO_2. The M13 phage particles were found to have a high affinity for incorporation into a densely assembled pattern on a-C films. These results suggest a versatile approach that can be used to influence the mineralization of a variety of smooth and homogeneous inorganic nanostructure layers and therefore open up exciting opportunities for the fabrication of organic–inorganic systems with nanoscale precision. I used these results later on (in chapter 6) and constructed multilayers of organic–inorganic materials, which contain alternating virus-templated layers.

These results opened up a new route for us to enhance the functional properties of inorganic materials, by using a self-assembled layer of densely-packed organic molecules to spatially arrange inorganic nanoparticles. For instance, I am using our knowledge on the self-assembly process to spatially arrange magnetic iron oxide nanoparticles on M13 phage templates in order to enhance the magnetic collective properties. To this end, phages are now being assembled on C-sputtered Si wafers at centimeter scales.

In chapter 5, although I have investigated the self-assembly of M13 macromolecules on flat surfaces in chapter 4, it is well known that an ordered medium of liquid crystals often possesses a variety of defects and deformations, at which the director *n(r)* of the liquid crystal undergoes an abrupt change compared to the vicinity of the defect. Experimental research on these effects had been remained challenging and been barely performed on confined rod-like colloidal particles at complex surfaces. Therefore, I studied the local deformation of rod-like M13 phage particles resulting from confinement in an irregular stranded web of thin a-C film in order to investigate the so-called 2D wall-anchoring. In this thesis chapter, I shifted the focus from evaporative self-organization on rationally designed surfaces to that on a complex surface. Here I deposited phages onto carbon web films with asymmetric shapes to study the effect of irregular spatial confinement on long semi-flexible M13 phages and their bending behavior. I showed that on unstructured and wide surface areas far from the

a-C surface edges, the phages exhibited random orientations when dispersed with a low concentration (1.0×10^{13} pfu/mL) in the isotropic phase. However, the orientation of M13 phages in two-dimensional nematic films was controlled by the orientation and curvature of the substrate edges. It was shown that on a single and narrow carbon strand (the straight leg of a Y junction) the mean molecular alignment can be described by a unit vector field, referred to as the director, which is oriented parallel to the axis of the strand. Whereas, a significant orientational evolution occurred in the intersections where the carbon strands meet. Here the M13 phages adopted a configuration that matched the confining boundary conditions in order to minimize the total free energy. In particular, the edges of the substrate determine the orientation of nearby phages. This orientational order is further induced to the neighboring molecules via intermolecular forces leading to the formation of oriented bundles of phages. Hence, close to the curved edges of the surface the phages tend to align parallel to the edges due to effective entropic forces and attractive van der Waals forces acting between them and the collars along the edges of the carbon surface. It should be noted that the drying process of the phages on the substrate can only modify the strength of the total effective forces acting on the orientational order of phages due to the increase of phage concentration at the contact lines with the solid surface. In other words, phages close to the surface edges orient and align such that their main axis directions become parallel to the periphery of the surface boundary. An annulus sector was superimposed on these oriented phage bundles that allowed us to derive analytic expressions for the bending energy of such oriented bundles. The defect, beyond which the molecules are geometrically frustrated, is located at the point at which the two annulus sectors meet. Our theoretical approach provides an explanation for the different number of phages orienting close to the surface edges with different local curvatures. By comparing the self-assembly on differently shaped carbon substrates, it was demonstrated that the alignment of the phages can be controlled by choosing appropriate substrate shapes. Properties of the system are characterized by the free energy which includes both energetic and entropic contributions. The competition of these contributions determines the resulting structures. Understanding the orientational behavior of phages on complex geometries of carbon web films can offer the active use of topological defects in controlling of liquid crystal flow, because the presence of topological defects strongly affects the flow of liquid crystals which elastically interact with surfaces.

Besides, our results could find application in the liquid crystal technology (*e.g.* memory effects) in topological manifolds which have interconnected porous media, similar to our carbon web films. This offers a convenient means to fabricate designed structures of orientationally ordered M13 phages. The understanding of such systems opens up new possibilities for defect engineering of liquid crystals which can be beneficial for the applications of liquid crystals in the presence of surface microscopic pores and irregularities.

In chapter 6, after detailed investigations on the adsorption and self-assembly behavior of M13 molecules on different surface structures in chapters 4 and 5, I employed phages as a soft scaffold for the layer-by-layer fabrication of hybrid organic–inorganic structures. The use of M13 phages for such multilayer design has not been done before. Bio-inspired fabrication of organic–inorganic nano-hybrid structures, where inorganic nanomaterials are templated by the organic component, are of high interest due to the broad range of applications of these structures. In this chapter, I used our designed in-house-built convective assembly apparatus to assemble densely-packed and highly-oriented phage layers (from a 3.5×10^{14} pfu/mL viral solution) on C-coated Si wafers. Because, a-C surface showed to be a promising host for aligned phages (as discussed in chapter 4). In our laboratory, I successfully assembled a phage-controlled nano-hybrid structure on a C-coated Si wafer using wild-type M13 phages and ZnO as the organic and the inorganic layers, respectively. Double alternating ZnO layers of about 20 nm were grown on directionally assembled phage templates via biomineralization process from a mineralization solution. The microstructure, elemental composition, and also the integrity of

the alternating biologically-templated inorganic multilayers were characterized using SEM, TEM and AFM. A homogeneous organic–inorganic hybrid structure without significant thickness fluctuations and with limited interpenetration of the interfaces was achieved. It was shown that the well-aligned viral films might act like a rubbed surface that promotes the alignment on the following layers. The RMS roughness of the resulting bilayered structure was measured to be ~14 nm which is only double of a single phage thickness. Our work provides information for the templating of organic–inorganic multilayers at the nanoscale, which might have potential in the construction of novel multicomponents with controlled organic to inorganic ratios.

Currently, I am working on the construction of a micrometer-scale multilayered structure which consists of 10 alternating organic (M13 phage) and inorganic (ZnO) layers with an adjusted thickness in order to enhance the mechanical properties of such multilayers.

All in all, our results give a comprehensive insight into 2D molecular self-assembly which can be used in the generation of alternating multilayered systems with nanostructured bio-templated inorganic materials that can be used as a constituent of electronic devices, such as transistors.

DECLARATION

Hereby I declare that this thesis titled, “Liquid Crystal Self-Assembly and Organic–Inorganic Hybrid Material Design” has been independently carried out by me at the Stuttgart Center for Electron Microscopy (StEM), Max Planck Institute for Solid State Research in partial fulfillment of the requirements for the degree of Doctor of Philosophy (Dr. rer. nat.) in Materials Science from Technical University of Darmstadt (TUD). I certify that the work presented in this thesis is, to the best of my knowledge and belief, original and contains no material previously published or written by another person, except where due reference and permission is made.

Stuttgart
23.01.2017

Pouya Moghimian

REFERENCES

1. Laskin, A. I.; Gadd, G. M.; Sarialani, S. *Advances in Applied Microbiology*; Elsevier Science Serials2012.
2. Chung, W. J.; Sena, M.; Merzlyak, A.; Lee, S. W. Phages as Tools for Functional Nanomaterials Development. In *Comprehensive Biomaterials*, Editor-in-Chief: Paul, D., Ed.; Elsevier: Oxford, 2011, pp 95-111.
3. Monk, A. B.; Rees, C. D.; Barrow, P.; Hagens, S.; Harper, D. R. Bacteriophage applications: where are we now? *Letters in Applied Microbiology* **2010,** *51* (4), 363-369.
4. Loset, G. A.; Sandlie, I. Next generation phage display by use of pVII and pIX as display scaffolds. *Methods* **2012,** *58* (1), 40-46.
5. Fauquet, C. M.; Mayo, M. A.; Maniloff, J.; Desselberger, U.; Ball, L. A. *Virus Taxonomy: VIIIth Report of the International Committee on Taxonomy of Viruses*; Elsevier Science2005.
6. Hyman, P.; Abedon, S. T. Bacteriophage (overview). In *Encyclopedia of Microbiology (Third Edition)*, Editor-in-Chief: Moselio, S., Ed.; Academic Press: Oxford, 2009, pp 322-338.
7. Tey, B. T.; Ooi, S. T.; Yong, K. C.; Ng, M. Y. T.; Ling, T. C.; Tan, W. S. Production of fusion m13 phage bearing the di-sulphide constrained peptide sequence (C-WSFFSNI-C) that interacts with hepatitis B core antigen. *Afr. J. Biotechnol.* **2009,** *8* (2), 268-273.
8. Rakonjac, J. Filamentous Bacteriophages: Biology and Applications. In *eLS*; John Wiley & Sons, Ltd, 2001.
9. Mohan, K.; Weiss, G. A. Chemically Modifying Viruses for Diverse Applications. *ACS Chemical Biology* **2016**.
10. Purdy, K. R.; Fraden, S. Isotropic-cholesteric phase transition of filamentous virus suspensions as a function of rod length and charge. *Physical Review E* **2004,** *70* (6), 061703.
11. Khalil, A. S.; Ferrer, J. M.; Brau, R. R.; Kottmann, S. T.; Noren, C. J.; Lang, M. J.; Belcher, A. M. Single M13 bacteriophage tethering and stretching. *Proceedings of the National Academy of Sciences* **2007,** *104* (12), 4892-4897.
12. Moghimian, P.; Harnau, L.; Srot, V.; de la Pena, F.; Farahmand Bafi, N.; Facey, S. J.; van Aken, P. A. Controlled self-assembly of biomolecular rods on structured substrates. *Soft Matter* **2016,** *12* (13), 3177-83.
13. Mao, C.; Wang, F.; Cao, B. Controlling Nanostructures of Mesoporous Silica Fibers by Supramolecular Assembly of Genetically Modifiable Bacteriophages. *Angewandte Chemie* **2012,** *124* (26), 6517-6521.
14. Chung, W. J.; Oh, J. W.; Kwak, K.; Lee, B. Y.; Meyer, J.; Wang, E.; Hexemer, A.; Lee, S. W. Biomimetic self-templating supramolecular structures. *Nature* **2011,** *478* (7369), 364-368.
15. Stopar, D.; Spruijt, R. B.; Wolfs, C.; Hemminga, M. A. Mimicking initial interactions of bacteriophage M13 coat protein disassembly in model membrane systems. *Biochemistry* **1998,** *37* (28), 10181-10187.
16. Jończyk, E.; Kłak, M.; Międzybrodzki, R.; Górski, A. The influence of external factors on bacteriophages—review. *Folia Microbiologica* **2011,** *56* (3), 191-200.
17. Yoo, P. J.; Nam, K. T.; Qi, J. F.; Lee, S. K.; Park, J.; Belcher, A. M.; Hammond, P. T. Spontaneous assembly of viruses on multilayered polymer surfaces. *Nat. Mater.* **2006,** *5* (3), 234-240.
18. Zaman, M. S.; Moon, C. H.; Bozhilov, K. N.; Haberer, E. D. Phage-directed synthesis of copper sulfide: Structural and optical characterization. *Nanotechnology* **2013,** *24* (32).
19. Sidhu, S. S. Engineering M13 for phage display. *Biomolecular Engineering* **2001,** *18* (2), 57-63.
20. Hess, G. T.; Guimaraes, C. P.; Spooner, E.; Ploegh, H. L.; Belcher, A. M. Orthogonal Labeling of M13 Minor Capsid Proteins with DNA to Self-Assemble End-to-End Multiphage Structures. *ACS Synthetic Biology* **2013**.
21. Kierny, M. R.; Cunningham, T. D.; Kay, B. K. Detection of biomarkers using recombinant antibodies coupled to nanostructured platforms. *Nano Reviews* **2012,** *3*, 10.3402/nano.v3i0.17240.
22. Johnson, I. D.; Hudson, B. S. Environmental modulation of M13 coat protein tryptophan fluorescence dynamics. *Biochemistry* **1989,** *28* (15), 6392-6400.
23. Salivar, W. O.; Tzagoloff, H.; Pratt, D. Some Physical-chemical and biological properties of rod-shaped coliphage M13. *Virology* **1964,** *24* (3), 359-371.
24. Nasir, S. F.; Jaworski, J. Assessing the stability of assembled filamentous phage coat protein P8. *Supramolecular Chemistry* **2014,** *26* (5/6), 329-337.

25. Collings, P. J.; Hird, M. *Introduction to Liquid Crystals: Chemistry and Physics*; CRC Press1997.
26. Collings, P. J. *Liquid Crystals: Nature's Delicate Phase of Matter*; Princeton University Press2002.
27. Khoo, I. C. *Liquid Crystals*; Wiley2007.
28. Dierking, I. *Textures of Liquid Crystals*; Wiley2006.
29. Singh, S.; Dunmur, D. A. *Liquid Crystals: Fundamentals*; World Scientific2002.
30. Peelle, B. R.; Krauland, E. M.; Wittrup, K. D.; Belcher, A. M. Design criteria for engineering inorganic material-specific peptides. *Langmuir* **2005,** *21* (15), 6929-6933.
31. Sawada, T.; Serizawa, T. Immobilization of highly oriented filamentous viruses onto polymer substrates. *J. Mat. Chem. B* **2013,** *1* (2), 149-152.
32. Dogic, Z.; Fraden, S. Cholesteric Phase in Virus Suspensions. *Langmuir* **2000,** *16* (20), 7820-7824.
33. Jeon, D.-Y.; Hwang, K. H.; Park, S.-J.; Kim, Y.-J.; Joo, M.-K.; Ahn, S.-E.; Kim, G.-T.; Nam, C.-H. Controlled surface adsorption of fd filamentous phage by tuning of the pH and the functionalization of the surface. *Journal of Applied Physics* **2011,** *109* (6), 064701-6.
34. Lee, S.-W.; Wood, B. M.; Belcher, A. M. Chiral Smectic C Structures of Virus-Based Films†. *Langmuir* **2002,** *19* (5), 1592-1598.
35. Yang, S. H.; Chung, W. J.; McFarland, S.; Lee, S. W. Assembly of Bacteriophage into Functional Materials. *Chem. Rec.* **2013,** *13* (1), 43-59.
36. Klem, M. T.; Willits, D.; Solis, D. J.; Belcher, A. M.; Young, M.; Douglas, T. Bio-inspired synthesis of protein-encapsulated CoPt nanoparticles. *Adv. Funct. Mater.* **2005,** *15* (9), 1489-1494.
37. Henry, M.; Debarbieux, L. Tools from viruses: Bacteriophage successes and beyond. *Virology* **2012,** *434* (2), 151-161.
38. Xu, H.; Cao, B. R.; George, A.; Mao, C. B. Self-Assembly and Mineralization of Genetically Modifiable Biological Nanofibers Driven by beta-Structure Formation. *Biomacromolecules* **2011,** *12* (6), 2193-2199.
39. Sawada, T.; Otsuka, H.; Yui, H.; Serizawa, T. Preparation and characterization of hybrid hydrogels composed of physically cross-linked gelatin and liquid-crystalline filamentous viruses. *Polymer Bulletin* **2015,** *72* (6), 1487-1496.
40. Moghimian, P.; Srot, V.; Rothenstein, D.; Facey, S. J.; Harnau, L.; Hauer, B.; Bill, J.; van Aken, P. A. Adsorption and Self-Assembly of M13 Phage into Directionally Organized Structures on C and SiO_2 Films. *Langmuir* **2014,** *30* (38), 11428-11432.
41. Lee, S. W.; Mao, C. B.; Flynn, C. E.; Belcher, A. M. Ordering of quantum dots using genetically engineered viruses. *Science* **2002,** *296* (5569), 892-895.
42. Sotiropoulou, S.; Sierra-Sastre, Y.; Mark, S. S.; Batt, C. A. Biotemplated Nanostructured Materials†. *Chemistry of Materials* **2008,** *20* (3), 821-834.
43. He, T.; Abbineni, G.; Cao, B.; Mao, C. Nanofibrous Bio-inorganic Hybrid Structures Formed Through Self-Assembly and Oriented Mineralization of Genetically Engineered Phage Nanofibers. *Small* **2010,** *6* (20), 2230-2235.
44. Pichon, B. P.; Demortière, A.; Pauly, M.; Mougin, K.; Derory, A.; Bégin-Colin, S. 2D Assembling of Magnetic Iron Oxide Nanoparticles Promoted by SAMs Used as Well-Addressed Surfaces. *The Journal of Physical Chemistry C* **2010,** *114* (19), 9041-9048.
45. Kleman, M.; Lavrentovich, O. D. Topological point defects in nematic liquid crystals. *Philosophical Magazine* **2006,** *86* (25-26), 4117-4137.
46. Whaley, S. R.; English, D. S.; Hu, E. L.; Barbara, P. F.; Belcher, A. M. Selection of peptides with semiconductor binding specificity for directed nanocrystal assembly. *Nature* **2000,** *405* (6787), 665-668.
47. Shen, L.; Bao, N.; Zhou, Z.; Prevelige, P. E.; Gupta, A. Materials design using genetically engineered proteins. *Journal of Materials Chemistry* **2011,** *21* (47), 18868-18876.
48. Lee, S.-Y.; Lim, J.-S.; Harris, M. T. Synthesis and application of virus-based hybrid nanomaterials. *Biotechnology and Bioengineering* **2012,** *109* (1), 16-30.
49. Kim, J.; Rheem, Y.; Yoo, B.; Chong, Y.; Bozhilov, K. N.; Kim, D.; Sadowsky, M. J.; Hur, H.-G.; Myung, N. V. Peptide-mediated shape- and size-tunable synthesis of gold nanostructures. *Acta Biomaterialia* **2010,** *6* (7), 2681-2689.

50. Soto, C. M.; Ratna, B. R. Virus hybrids as nanomaterials for biotechnology. *Curr. Opin. Biotechnol.* **2010,** *21* (4), 426-438.
51. Nam, K. T.; Kim, D. W.; Yoo, P. J.; Chiang, C. Y.; Meethong, N.; Hammond, P. T.; Chiang, Y. M.; Belcher, A. M. Virus-enabled synthesis and assembly of nanowires for lithium ion battery electrodes. *Science* **2006,** *312* (5775), 885-888.
52. Lee, Y. J.; Yi, H.; Kim, W.-J.; Kang, K.; Yun, D. S.; Strano, M. S.; Ceder, G.; Belcher, A. M. Fabricating Genetically Engineered High-Power Lithium-Ion Batteries Using Multiple Virus Genes. *Science* **2009,** *324* (5930), 1051-1055.
53. Huang, Y.; Chiang, C.-Y.; Lee, S. K.; Gao, Y.; Hu, E. L.; Yoreo, J. D.; Belcher, A. M. Programmable Assembly of Nanoarchitectures Using Genetically Engineered Viruses. *Nano Lett.* **2005,** *5* (7), 1429-1434.
54. Courchesne, N.-M. D.; Klug, M. T.; Chen, P.-Y.; Kooi, S. E.; Yun, D. S.; Hong, N.; Fang, N. X.; Belcher, A. M.; Hammond, P. T. Assembly of a Bacteriophage-Based Template for the Organization of Materials into Nanoporous Networks. *Adv. Mater.* **2014**, n/a-n/a.
55. Jeong, C. K.; Kim, I.; Park, K.-I.; Oh, M. H.; Paik, H.; Hwang, G.-T.; No, K.; Nam, Y. S.; Lee, K. J. Virus-Directed Design of a Flexible $BaTiO_3$ Nanogenerator. *ACS Nano* **2013,** *7* (12), 11016-11025.
56. Chen, P.-Y.; Dang, X.; Klug, M. T.; Courchesne, N.-M. D.; Qi, J.; Hyder, M. N.; Belcher, A. M.; Hammond, P. T. M13 Virus-Enabled Synthesis of Titanium Dioxide Nanowires for Tunable Mesoporous Semiconducting Networks. *Chemistry of Materials* **2015,** *27* (5), 1531-1540.
57. Atanasova, P.; Rothenstein, D.; Schneider, J. J.; Hoffmann, R. C.; Dilfer, S.; Eiben, S.; Wege, C.; Jeske, H.; Bill, J. Virus-Templated Synthesis of ZnO Nanostructures and Formation of Field-Effect Transistors. *Adv. Mater.* **2011,** *23* (42), 4918-4922.
58. Moghimian, P.; Kilper, S.; Srot, V.; Rothenstein, D.; Facey, S. J.; Hauer, B.; Bill, J.; van Aken, P. A. Phage-assisted assembly of organic–inorganic hybrid bilayers. *International Journal of Materials Research* **2016,** *107* (4), 295-299.
59. Janairo Jose Isagani, B.; Co, F.; Carandang Jose, S.; Amalin Divina, M. Sequence-dependent cluster analysis of biomineralization peptides. In *Zeitschrift für Naturforschung C*, 2015; Vol. 70, p 191.
60. Masica, D. L.; Schrier, S. B.; Specht, E. A.; Gray, J. J. De Novo Design of Peptide−Calcite Biomineralization Systems. *Journal of the American Chemical Society* **2010,** *132* (35), 12252-12262.
61. Patwardhan, S. V.; Patwardhan, G.; Perry, C. C. Interactions of biomolecules with inorganic materials: principles, applications and future prospects. *Journal of Materials Chemistry* **2007,** *17* (28), 2875-2884.
62. Berti, L.; Burley, G. A. Nucleic acid and nucleotide-mediated synthesis of inorganic nanoparticles. *Nat Nano* **2008,** *3* (2), 81-87.
63. Balci, S.; Bittner, A. M.; Schirra, M.; Thonke, K.; Sauer, R.; Hahn, K.; Kadri, A.; Wege, C.; Jeske, H.; Kern, K. Catalytic coating of virus particles with zinc oxide. *Electrochimica Acta* **2009,** *54* (22), 5149-5154.
64. Gerstel, P.; Hoffmann, R. C.; Lipowsky, P.; Jeurgens, L. P. H.; Bill, J.; Aldinger, F. Mineralization from Aqueous Solutions of Zinc Salts Directed by Amino Acids and Peptides. *Chemistry of Materials* **2006,** *18* (1), 179-186.
65. Tomczak, M. M.; Gupta, M. K.; Drummy, L. F.; Rozenzhak, S. M.; Naik, R. R. Morphological control and assembly of zinc oxide using a biotemplate. *Acta Biomaterialia* **2009,** *5* (3), 876-882.
66. Egerton, R. F. *Physical Principles of Electron Microscopy: An Introduction to TEM, SEM, and AEM*; Springer2005.
67. Flegler, S. L.; Heckman, J. W.; Klomparens, K. L. *Scanning and Transmission Electron Microscopy: An Introduction*; Oxford University Press1993.
68. Williams, D. B.; Carter, C. B. *Transmission Electron Microscopy: A Textbook for Materials Science*; Springer London, Limited2009.
69. Reimer, L. *Scanning Electron Microscopy: Physics of Image Formation and Microanalysis*; Springer1998.
70. Lobocka, M.; Szybalski, W. T. *Bacteriophages*; Elsevier Science2012.
71. Richards, R.; Owen, G. R.; Ap Gwynn, I. Low voltage backscattered electron imaging (< 5 kV) using field emission scanning electron microscopy. *Scanning Microsc* **1999,** *13* (1), 55-60.

72. Egerton, R. F.; Li, P.; Malac, M. Radiation damage in the TEM and SEM. *Micron* **2004,** *35* (6), 399-409.
73. Goodhew, P. J.; Humphreys, J.; Beanland, R. *Electron Microscopy and Analysis, Third Edition*; Taylor & Francis2000.
74. Mullejans, H.; Bruley, J. Electron energy-loss spectroscopy (EELS); comparison with x-ray analysis. *Journal De Physique* **1993,** *3* (7 pt 3), 2083-2092.
75. Wang, Y.; Baiutti, F.; Gregori, G.; Cristiani, G.; Salzberger, U.; Logvenov, G.; Maier, J.; van Aken, P. A. Atomic-Scale Quantitative Analysis of Lattice Distortions at Interfaces of Two-Dimensionally Sr-Doped La(2)CuO(4) Superlattices. *ACS Applied Materials & Interfaces* **2016,** *8* (10), 6763-6769.
76. Hayat, M. *Basic Techniques For Transmission Electron Microscopy*; Elsevier Science1985.
77. Slocik, J. M.; Stone, M. O.; Naik, R. R. Synthesis of gold nanoparticles using multifunctional peptides. *Small* **2005,** *1* (11), 1048-1052.
78. Dang, X.; Yi, H.; Ham, M.-H.; Qi, J.; Yun, D. S.; Ladewski, R.; Strano, M. S.; Hammond, P. T.; Belcher, A. M. Virus-templated self-assembled single-walled carbon nanotubes for highly efficient electron collection in photovoltaic devices. *Nat Nano* **2011,** *6* (6), 377-384.
79. Nam, Y. S.; Magyar, A. P.; Lee, D.; Kim, J. W.; Yun, D. S.; Park, H.; Pollom, T. S.; Weitz, D. A.; Belcher, A. M. Biologically templated photocatalytic nanostructures for sustained light-driven water oxidation. *Nat. Nanotechnol.* **2010,** *5* (5), 340-344.
80. Cao, B. R.; Xu, H.; Mao, C. B. Transmission Electron Microscopy as a Tool to Image Bioinorganic Nanohybrids: The Case of Phage-Gold Nanocomposites. *Microsc. Res. Tech.* **2011,** *74* (7), 627-635.
81. Özdöl, V. B.; Srot, V.; van Aken, P. A. Sample Preparation Techniques for Transmission Electron Microscopy. In *Handbook of Nanoscopy*; Wiley-VCH Verlag GmbH & Co. KGaA, 2012, pp 473-498.
82. Srot, V.; Bussmann, B.; Salzberger, U.; Koch, C. T.; van Aken, P. A. Linking Microstructure and Nanochemistry in Human Dental Tissues. *Microscopy and Microanalysis* **2012,** *18* (03), 509-523.
83. Voigtlaender, B. *Scanning Probe Microscopy: Atomic Force Microscopy and Scanning Tunneling Microscopy*; Springer Berlin Heidelberg2015.
84. Förch, R.; Schönherr, H.; Jenkins, A. T. A. *Surface Design: Applications in Bioscience and Nanotechnology*; Wiley2009.
85. Pazokian, H.; Jelvani, S.; Mollabashi, M.; Barzin, J.; Azizabadi Farahani, G. ArF laser surface modification of polyethersulfone film: Effect of laser fluence in improving surface biocompatibility. *Applied Surface Science* **2011,** *257* (14), 6186-6190.
86. (http://www.biosci.missouri.edu/smithgp/PhageDisplayWebsite/PhageDisplayWebsiteIndex) (AbsorptionSpectrum.doc 12/29/1999).
87. Lin, Z. *Evaporative self-assembly of ordered complex structures*; World Scientific Publishing Company, Incorporated2012.
88. Hernando-Perez, M.; Pascual, E.; Aznar, M.; Ionel, A.; Caston, J. R.; Luque, A.; Carrascosa, J. L.; Reguera, D.; de Pablo, P. J. The interplay between mechanics and stability of viral cages. *Nanoscale* **2014,** *6* (5), 2702-2709.
89. Moghimian, P.; Srot, V.; Pichon, B. P.; Facey, S. J.; van Aken, P. A. Stability of M13 Phage in Organic Solvents. *Journal of Biomaterials and Nanobiotechnology* **2016,** *7* (2), 72-77.
90. Mattos, C.; Ringe, D. Proteins in organic solvents. *Current Opinion in Structural Biology* **2001,** *11* (6), 761-764.
91. Lau, F. W.; Bowie, J. U. A Method for Assessing the Stability of a Membrane Protein. *Biochemistry* **1997,** *36* (19), 5884-5892.
92. Amako, K.; Yasunaka, K. Ether induced morphological alteration of Pf-1 filamentous phage. *Nature* **1977,** *267* (5614), 862-863.
93. Olofsson, L.; Ankarloo, J.; Andersson, P. O.; Nicholls, I. A. Filamentous bacteriophage stability in non-aqueous media. *Chemistry & Biology* **2001,** *8* (7), 661-671.
94. Mao, C.; Liu, A.; Cao, B. Virus-Based Chemical and Biological Sensing. *Angewandte Chemie International Edition* **2009,** *48* (37), 6790-6810.
95. Lee, Y. M.; Kim, Y. H.; Lee, J. H.; Park, J. H.; Park, N.-G.; Choe, W.-S.; Ko, M. J.; Yoo, P. J. Highly Interconnected Porous Electrodes for Dye-Sensitized Solar Cells Using Viruses as a Sacrificial Template. *Adv. Funct. Mater.* **2011,** *21* (6), 1160-1167.

96. Tsen, K. T.; Tsen, S.-W. D.; Fu, Q.; Lindsay, S. M.; Kibler, K.; Jacobs, B.; Wu, T. C.; Li, Z.; Yan, H.; Cope, S.; Vaiana, S.; Kiang, J. G. In *Photonic approach to the selective inactivation of viruses with a near-infrared ultrashort pulsed laser*, 2010, pp 75610W-75610W-10.
97. Zhong, C.; Duan, C.; Huang, F.; Wu, H.; Cao, Y. Materials and Devices toward Fully Solution Processable Organic Light-Emitting Diodes. *Chemistry of Materials* **2011,** *23* (3), 326-340.
98. Roberts, L. M.; Dunker, A. K. Structural changes accompanying chloroform-induced contraction of the filamentous phage fd. *Biochemistry* **1993,** *32* (39), 10479-10488.
99. Wigle, J. C.; Holwitt, E. A.; Noojin, G. D.; Estlack, L. E.; Sheldon, K. E.; Rockwell, B. A. In *No effect of femtosecond laser pulses on DNA, protein, M13, or E. coli*, 2011, pp 789716-789716-9.
100. Martinek, K.; Mozhaev, V. V.; Smirnov, M. D.; Berezin, L. V. Reactivation of "irreversibly" denaturated enzymes. *Biotechnology and Bioengineering* **1980,** *22* (1), 247-251.
101. Lee, B. Y.; Zhang, J.; Zueger, C.; Chung, W.-J.; Yoo, S. Y.; Wang, E.; Meyer, J.; Ramesh, R.; Lee, S.-W. Virus-based piezoelectric energy generation. *Nat Nano* **2012,** *7* (6), 351-356.
102. Toulemon, D.; Pichon, B. P.; Cattoen, X.; Man, M. W. C.; Begin-Colin, S. 2D assembly of non-interacting magnetic iron oxide nanoparticles via "click" chemistry. *Chemical Communications* **2011,** *47* (43), 11954-11956.
103. Neltner, B.; Peddie, B.; Xu, A.; Doenlen, W.; Durand, K.; Yun, D. S.; Speakman, S.; Peterson, A.; Belcher, A. Production of Hydrogen Using Nanocrystalline Protein-Templated Catalysts on M13 Phage. *ACS Nano* **2010,** *4* (6), 3227-3235.
104. Cao, B.; Zhu, Y.; Wang, L.; Mao, C. Controlled Alignment of Filamentous Supramolecular Assemblies of Biomolecules into Centimeter-Scale Highly Ordered Patterns by Using Nature-Inspired Magnetic Guidance. *Angewandte Chemie International Edition* **2013,** *52* (45), 11750-11754.
105. Whyburn, G. P.; Li, Y.; Huang, Y. Protein and protein assembly based material structures. *Journal of Materials Chemistry* **2008,** *18* (32), 3755-3762.
106. Wang, J.; Wang, L.; Li, X.; Mao, C. Virus activated artificial ECM induces the osteoblastic differentiation of mesenchymal stem cells without osteogenic supplements. *Sci. Rep.* **2013,** *3*.
107. Zhu, H.; Cao, B.; Zhen, Z.; Laxmi, A. A.; Li, D.; Liu, S.; Mao, C. Controlled growth and differentiation of MSCs on grooved films assembled from monodisperse biological nanofibers with genetically tunable surface chemistries. *Biomaterials* **2011,** *32* (21), 4744-4752.
108. Kuncicky, D. M.; Naik, R. R.; Velev, O. D. Rapid deposition and long-range alignment of nanocoatings and arrays of electrically conductive wires from tobacco mosaic virus. *Small* **2006,** *2* (12), 1462-1466.
109. Vinnichenko, M.; Gago, R.; Huang, N.; Leng, Y. X.; Sun, H.; Kreissig, U.; Kulish, M. P.; Maitz, M. F. Spectroscopic ellipsometry investigation of amorphous carbon films with different sp3 content: relation with protein adsorption. *Thin Solid Films* **2004,** *455–456* (0), 530-534.
110. Lee, Y. M.; Jung, B.; Kim, Y. H.; Park, A. R.; Han, S.; Choe, W.-S.; Yoo, P. J. Nanomesh-Structured Ultrathin Membranes Harnessing the Unidirectional Alignment of Viruses on a Graphene-Oxide Film. *Adv. Mater.* **2014,** *26* (23), 3899-3904.
111. Ling, T. C.; Loong, C. M.; Tan, W. S.; Tey, B. T.; Abdullah, W. M. W.; Ariff, A. Purification of filamentous bacteriophage M13 by expanded bed anion exchange chromatography. *Journal of Microbiology* **2004,** *42* (3), 228-232.
112. Merzlyak, A.; Lee, S. W. Phage as templates for hybrid materials and mediators for nanomaterial synthesis. *Curr. Opin. Chem. Biol.* **2006,** *10* (3), 246-252.
113. Zakharova, M. Y.; Kozyr, A. V.; Ignatova, A. N.; Vinnikov, I. A.; Sherriyakin, I. G.; Kolesnikov, A. V. Purification of filamentous bacteriophage for phage display using size-exclusion chromatography. *Biotechniques* **2005,** *38* (2), 194-+.
114. Berlind, T.; Tengvall, P.; Hultman, L.; Arwin, H. Protein adsorption on thin films of carbon and carbon nitride monitored with in situ ellipsometry. *Acta Biomaterialia* **2011,** *7* (3), 1369-1378.
115. Masteika, V.; Kowal, J.; Braithwaite, N. S. J.; Rogers, T. A Review of Hydrophilic Silicon Wafer Bonding. *ECS Journal of Solid State Science and Technology* **2014,** *3* (4), Q42-Q54.
116. Gerba, C. P. Applied and Theoretical Aspects of Virus Adsorption to Surfaces. In *Advances in Applied Microbiology*, Allen, I. L., Ed.; Academic Press, 1984; Vol. Volume 30, pp 133-168.
117. Takeda, S.; Fukawa, M.; Hayashi, Y.; Matsumoto, K. Surface OH group governing adsorption properties of metal oxide films. *Thin Solid Films* **1999,** *339* (1–2), 220-224.
118. Takeda, S.; Fukawa, M. Role of surface OH groups in surface chemical properties of metal oxide films. *Materials Science and Engineering: B* **2005,** *119* (3), 265-267.

119. Kayser, R. F.; Raveché, H. J. Bifurcation in Onsager's model of the isotropic-nematic transition. *Physical Review A* **1978,** *17* (6), 2067-2072.
120. Bolisetty, S.; Harnau, L.; Jung, J.-m.; Mezzenga, R. Gelation, Phase Behavior, and Dynamics of β-Lactoglobulin Amyloid Fibrils at Varying Concentrations and Ionic Strengths. *Biomacromolecules* **2012,** *13* (10), 3241-3252.
121. Suib, S. L. *New and Future Developments in Catalysis: Batteries, Hydrogen Storage and Fuel Cells*; Elsevier Science2013.
122. McCafferty, E.; Wightman, J. P. Determination of the concentration of surface hydroxyl groups on metal oxide films by a quantitative XPS method. *Surface and Interface Analysis* **1998,** *26* (8), 549-564.
123. Puddu, V.; Perry, C. C. Peptide Adsorption on Silica Nanoparticles: Evidence of Hydrophobic Interactions. *ACS Nano* **2012,** *6* (7), 6356-6363.
124. Scott, E. A.; Engineering, W. U. i. S. L. B. *Improving Biocompatibility by Controlling Protein Adsorption: Modification and Design of Biomaterials Using Poly(ethylene Glycol) Microgels and Microspheres*; Washington University in St. Louis2009.
125. Dinsmore, A.; Yodh, A.; Pine, D. Entropic control of particle motion using passive surface microstructures. *Nature* **1996,** *383* (6597), 239-242.
126. Ye, Y.-H.; Badilescu, S.; Truong, V.-V.; Rochon, P.; Natansohn, A. Self-assembly of colloidal spheres on patterned substrates. *Applied Physics Letters* **2001,** *79* (6), 872-874.
127. Lin, K.-h.; Crocker, J. C.; Prasad, V.; Schofield, A.; Weitz, D. A.; Lubensky, T. C.; Yodh, A. G. Entropically Driven Colloidal Crystallization on Patterned Surfaces. *Physical Review Letters* **2000,** *85* (8), 1770-1773.
128. Yin, Y.; Xia, Y. Growth of large colloidal crystals with their (100) planes orientated parallel to the surfaces of supporting substrates. *Adv. Mater.* **2002,** *14* (8), 605.
129. Bryk, P.; Roth, R.; Schoen, M.; Dietrich, S. Depletion potentials near geometrically structured substrates. *EPL (Europhysics Letters)* **2003,** *63* (2), 233.
130. Urrutia, I. Fluids confined in wedges and by edges: Virial series for the line-thermodynamic properties of hard spheres. *The Journal of Chemical Physics* **2014,** *141* (24), 244906.
131. Boda, D.; Chan, K.-Y.; Henderson, D.; Wasan, D. T.; Nikolov, A. D. Structure and Pressure of a Hard Sphere Fluid in a Wedge-Shaped Cell or Meniscus. *Langmuir* **1999,** *15* (13), 4311-4313.
132. Yu, Y.-X.; Wu, J. A modified fundamental measure theory for spherical particles in microchannels. *The Journal of Chemical Physics* **2003,** *119* (4), 2288-2295.
133. Merzlyak, A.; Indrakanti, S.; Lee, S.-W. Genetically Engineered Nanofiber-Like Viruses For Tissue Regenerating Materials. *Nano Lett.* **2009,** *9* (2), 846-852.
134. Viry, L.; Mercader, C.; Miaudet, P.; Zakri, C.; Derr, A.; Kuhn, A.; Maugey, M.; Poulin, P. Nanotube fibers for electromechanical and shape memory actuators. *Journal of Materials Chemistry* **2010,** *20* (17), 3487-3495.
135. Jiang, K.; Wang, J.; Li, Q.; Liu, L.; Liu, C.; Fan, S. Superaligned Carbon Nanotube Arrays, Films, and Yarns: A Road to Applications. *Adv. Mater.* **2011,** *23* (9), 1154-1161.
136. Kim, D.-H.; Lee, H.; Lee, Y. K.; Nam, J.-M.; Levchenko, A. Biomimetic Nanopatterns as Enabling Tools for Analysis and Control of Live Cells. *Adv. Mater.* **2010,** *22* (41), 4551-4566.
137. Yang, Z.; Chen, T.; He, R.; Guan, G.; Li, H.; Qiu, L.; Peng, H. Aligned Carbon Nanotube Sheets for the Electrodes of Organic Solar Cells. *Adv. Mater.* **2011,** *23* (45), 5436-5439.
138. Reddy, A. L. M.; Gowda, S. R.; Shaijumon, M. M.; Ajayan, P. M. Hybrid Nanostructures for Energy Storage Applications. *Adv. Mater.* **2012,** *24* (37), 5045-5064.
139. Han, J.; Craighead, H. G. Separation of Long DNA Molecules in a Microfabricated Entropic Trap Array. *Science* **2000,** *288* (5468), 1026-1029.
140. Masanori, U.; Tetsuya, H.; Yuzuru, T.; Yasuhiro, H.; Tomonari, D.; Yoshinobu, B. Curvature Entropy Trapping of Long DNA under Hydrodynamic Flows in Microfluidic Devices. *Japanese Journal of Applied Physics* **2004,** *43* (4R), 1649.
141. Reccius, C. H.; Mannion, J. T.; Cross, J. D.; Craighead, H. G. Compression and Free Expansion of Single DNA Molecules in Nanochannels. *Physical Review Letters* **2005,** *95* (26), 268101.
142. Kheireddin, B. A.; Narayanunni, V.; Akbulut, M. Influence of Shearing Surface Topography on Frictional Properties of ZnS Nanowire-Based Lubrication System across Ductile Surfaces. *Journal of Tribology* **2012,** *134* (2), 022001-022001.

143. Dammone, O. J.; Zacharoudiou, I.; Dullens, R. P. A.; Yeomans, J. M.; Lettinga, M. P.; Aarts, D. G. A. L. Confinement Induced Splay-to-Bend Transition of Colloidal Rods. *Physical Review Letters* **2012,** *109* (10), 108303.
144. Tombolato, F.; Ferrarini, A.; Grelet, E. Chiral Nematic Phase of Suspensions of Rodlike Viruses: Left-Handed Phase Helicity from a Right-Handed Molecular Helix. *Physical Review Letters* **2006,** *96* (25), 258302.
145. Dugyala, V. R.; Daware, S. V.; Basavaraj, M. G. Shape anisotropic colloids: synthesis, packing behavior, evaporation driven assembly, and their application in emulsion stabilization. *Soft Matter* **2013,** *9* (29), 6711-6725.
146. Byun, M.; Bowden, N. B.; Lin, Z. Hierarchically Organized Structures Engineered from Controlled Evaporative Self-Assembly. *Nano Lett.* **2010,** *10* (8), 3111-3117.
147. Lin, Y.; Su, Z.; Xiao, G.; Balizan, E.; Kaur, G.; Niu, Z.; Wang, Q. Self-Assembly of Virus Particles on Flat Surfaces via Controlled Evaporation†. *Langmuir* **2010,** *27* (4), 1398-1402.
148. Van Der Walt, S.; Schönberger, J. L.; Nunez-Iglesias, J.; Boulogne, F.; Warner, J. D.; Yager, N.; Gouillart, E.; Yu, T. scikit-image: image processing in Python. *PeerJ* **2014,** *2*, e453.
149. De Gennes, P.; Prost, J. The physics of liquid crystals, 2nd edn Oxford University Press. *New York* **1993**.
150. Landau, L.; Lifshitz, E. Theory of Elasticity. Pergamon Press, Oxford, UK, 1986.
151. Landau, L.; Lifshitz, E. Statistical Physics, Part 1 (3rd edit.) Pergamon Press. Oxford, NY, 1980.
152. Rivetti, C.; Walker, C.; Bustamante, C. Polymer chain statistics and conformational analysis of DNA molecules with bends or sections of different flexibility. *Journal of Molecular Biology* **1998,** *280* (1), 41-59.
153. Rivetti, C.; Guthold, M.; Bustamante, C. Scanning Force Microscopy of DNA Deposited onto Mica: EquilibrationversusKinetic Trapping Studied by Statistical Polymer Chain Analysis. *Journal of Molecular Biology* **1996,** *264* (5), 919-932.
154. Adamcik, J.; Mezzenga, R. Proteins Fibrils from a Polymer Physics Perspective. *Macromolecules* **2011,** *45* (3), 1137-1150.
155. Adamcik, J.; Jung, J.-M.; Flakowski, J.; De Los Rios, P.; Dietler, G.; Mezzenga, R. Understanding amyloid aggregation by statistical analysis of atomic force microscopy images. *Nat Nano* **2010,** *5* (6), 423-428.
156. Rinke, G.; Rauschenbach, S.; Harnau, L.; Albarghash, A.; Pauly, M.; Kern, K. Active Conformation Control of Unfolded Proteins by Hyperthermal Collision with a Metal Surface. *Nano Lett.* **2014,** *14* (10), 5609-5615.
157. Deng, Z.; Thontasen, N.; Malinowski, N.; Rinke, G.; Harnau, L.; Rauschenbach, S.; Kern, K. A Close Look at Proteins: Submolecular Resolution of Two- and Three-Dimensionally Folded Cytochrome c at Surfaces. *Nano Lett.* **2012,** *12* (5), 2452-2458.
158. Abramowitz, M.; Stegun, I. A. *Handbook of mathematical functions: with formulas, graphs, and mathematical tables*; Courier Dover Publications1972.
159. Malis, T.; Cheng, S. C.; Egerton, R. F. EELS log-ratio technique for specimen-thickness measurement in the TEM. *Journal of Electron Microscopy Technique* **1988,** *8* (2), 193-200.
160. Mitchell, D. R. G. Determination of mean free path for energy loss and surface oxide film thickness using convergent beam electron diffraction and thickness mapping: a case study using Si and P91 steel. *Journal of Microscopy* **2006,** *224* (2), 187-196.
161. Harnau, L.; Penna, F.; Dietrich, S. Colloidal hard-rod fluids near geometrically structured substrates. *Physical Review E* **2004,** *70* (2), 021505.
162. Grelet, E. Hexagonal Order in Crystalline and Columnar Phases of Hard Rods. *Physical Review Letters* **2008,** *100* (16), 168301.
163. Jerome, B. Surface effects and anchoring in liquid crystals. *Reports on Progress in Physics* **1991,** *54* (3), 391.
164. Soares e Silva, M.; Alvarado, J.; Nguyen, J.; Georgoulia, N.; Mulder, B. M.; Koenderink, G. H. Self-organized patterns of actin filaments in cell-sized confinement. *Soft Matter* **2011,** *7* (22), 10631-10641.
165. Zhang, S.; Kinloch, I. A.; Windle, A. H. Mesogenicity Drives Fractionation in Lyotropic Aqueous Suspensions of Multiwall Carbon Nanotubes. *Nano Lett.* **2006,** *6* (3), 568-572.

166. Chang, C.; Lu, L.; Liu, J.; Chen, W. Bending Deformation Mechanism and Defective Properties of Liquid Crystalline Carbon Nanotubes in Evaporating Droplets. *RSC Advances* **2011,** *1* (3), 468-473.
167. Zhang, S.; Li, Q.; Kinloch, I. A.; Windle, A. H. Ordering in a Droplet of an Aqueous Suspension of Single-Wall Carbon Nanotubes on a Solid Substrate. *Langmuir* **2010,** *26* (3), 2107-2112.
168. Araki, T.; Serra, F.; Tanaka, H. Defect science and engineering of liquid crystals under geometrical frustration. *Soft Matter* **2013,** *9* (34), 8107-8120.
169. Belyaev, B. A.; Drokin, N. A.; Kumakhov, M. A.; Shabanov, V. F. Dielectric properties of liquid crystals in polycapillary matrices. *Physics of the Solid State* **2010,** *52* (6), 1315-1322.
170. Serra, F.; Eaton, S. M.; Cerbino, R.; Buscaglia, M.; Cerullo, G.; Osellame, R.; Bellini, T. Nematic Liquid Crystals Embedded in Cubic Microlattices: Memory Effects and Bistable Pixels. *Adv. Funct. Mater.* **2013,** *23* (32), 3990-3994.
171. Park, S.; Yun, W. M.; Kim, L. H.; Park, S.; Kim, S. H.; Park, C. E. Inorganic/organic multilayer passivation incorporating alternating stacks of organic/inorganic multilayers for long-term air-stable organic light-emitting diodes. *Organic Electronics* **2013,** *14* (12), 3385-3391.
172. Habib, M.; Watanabe, K.; Nagata, F. Bioinspiration and emerging actuator technologies. *Artif Life Robotics* **2012,** *17* (2), 191-196.
173. Cao, B.; Xu, H.; Mao, C. Phage as a Template to Grow Bone Mineral Nanocrystals. *Methods in molecular biology (Clifton, N.J.)* **2014,** *1108*, 123-135.
174. Rothenstein, D.; Facey, S. J.; Ploss, M.; Hans, P.; Melcher, M.; Srot, V.; Van Aken, P. A.; Hauer, B.; Bill, J. Mineralization of gold nanoparticles using tailored M13 phages. *Bioinspired, Biomimetic and Nanobiomaterials* **2013,** *2* (4, Themed Issue-Biomaterials Topic, MSE Conference, Darmstadt, 25-27 September 2012-Part 2), 173-185.
175. Burghard, Z.; Zini, L.; Srot, V.; Bellina, P.; van Aken, P. A.; Bill, J. Toughening through Nature-Adapted Nanoscale Design. *Nano Lett.* **2009,** *9* (12), 4103-4108.
176. Takada, J.; Awaji, H.; Koshioka, M.; Nakajima, A.; Nevin, W. A. Organic–inorganic multilayers: A new concept of optoelectronic material. *Applied Physics Letters* **1992,** *61* (18), 2184-2186.
177. Atanasova, P.; Weitz, R. T.; Gerstel, P.; Srot, V.; Kopold, P.; van Aken, P. A.; Burghard, M.; Bill, J. DNA-templated synthesis of ZnO thin layers and nanowires. *Nanotechnology* **2009,** *20* (36).
178. Lipowsky, P.; Hoffmann, R. C.; Welzel, U.; Bill, J.; Aldinger, F. Site-Selective Deposition of Nanostructured ZnO Thin Films from Solutions Containing Polyvinylpyrrolidone. *Adv. Funct. Mater.* **2007,** *17* (13), 2151-2159.
179. Mansoori, G. A.; George, T. F.; Assoufid, L.; Zhang, G. *Molecular Building Blocks for Nanotechnology: From Diamondoids to Nanoscale Materials and Applications*; Springer New York2007.
180. Cortes-Jimenez, S. Y. Site Specific Nanowire Growth. MATERIALS NNIN REU, 2006.
181. Peter, L.; Žaklina, B.; Lars, P. H. J.; Joachim, B.; Fritz, A. Laminates of zinc oxide and poly(amino acid) layers with enhanced mechanical performance. *Nanotechnology* **2007,** *18* (34), 345707.
182. Newman, J.; Swinney, H. L.; Day, L. A. Hydrodynamic properties and structure of fd virus. *Journal of Molecular Biology* **1977,** *116* (3), 593-603.
183. Niklasson, A. M. N.; Abrikosov, I. A.; Johansson, B. Interface mixing energy: A measure of interface stability. *Physical Review B* **1998,** *58* (7), 3613-3616.
184. Wang, X.; Miller, D. S.; Bukusoglu, E.; de Pablo, J. J.; Abbott, N. L. Topological defects in liquid crystals as templates for molecular self-assembly. *Nat Mater* **2015,** *advance online publication*.
185. Harsha, P. K. *Principles of Vapor Deposition of Thin Films*; Elsevier Science2005.